What Can We Learn in Electrocatalysis, from Nanoparticulated Precious and/or Non-Precious Catalytic Centers Interacting with Their Support?

Juan Mora-Hernández, Yun Luo, Nicolas Alonso-Vante

catalysts

MDPI

Review

What Can We Learn in Electrocatalysis, from Nanoparticulated Precious and/or Non-Precious Catalytic Centers Interacting with Their Support?

Juan Manuel Mora-Hernández, Yun Luo and Nicolas Alonso-Vante *

IC2MP, UMR-CNRS 7285, University of Poitiers, 4 rue Michel Brunet, 86022 Poitiers, France; jmmora@live.com.mx (J.M.M.-H.); yun.luo@univ-poitiers.fr (Y.L.)

* Correspondence: nicolas.alonso.vante@univ-poitiers.fr; Tel.: +33-054-945-3625

Academic Editors: Vicenzo Baglio and David Sebastián

Received: 12 July 2016; Accepted: 9 September 2016; Published: 21 September 2016

Abstract: This review is devoted to discussing the state of the art in the relevant aspects of the synthesis of novel precious and non-precious electrocatalysts. It covers the production of Pt- and Pd-based electrocatalysts synthesized by the carbonyl chemical route, the synthesis description for the preparation of the most catalytically active transition metal chalcogenides, then the employment of free-surfactants synthesis routes to produce non-precious electrocatalysts. A compilation of the best precious electrocatalysts to perform the hydrogen oxidation reaction (HOR) is described; a section is devoted to the synthesis and electrocatalytic evaluation of non-precious materials which can be used to perform the HOR in alkaline medium. Apropos the oxygen reduction reaction (ORR), the synthesis and modification of the supports is also discussed as well, aiming at describing the state of the art to improve kinetics of low temperature fuel cell reactions via the hybridization process of the catalytic center with a variety of carbon-based, and ceramic-carbon supports. Last, but not least, the review covers the experimental half-cells results in a micro-fuel cell platform obtained in our laboratory, and by other workers, analyzing the history of the first micro-fuel cell systems and their tailoring throughout the time bestowing to the design and operating conditions.

Keywords: low temperature fuel cells; electrocatalysts; catalytic centers; micro laminar flow fuel cells

1. Introduction

Fuel cell technology is a promising strategy to provide power for areas where there is no access to the public or where the cost of wiring and electricity transfer network is important. These devices are usually employed as an energy source for purposes that require non-intermittent power stations such as power generation and energy distribution systems. The use of hydrogen as a fuel makes them clean energy systems with less noise, and pollution generation [1]. Currently, fuel cells are used in both small and large systems such as combined-heat-power (CHP) systems, mobile power, portable computers and communication equipment [2]. Despite all these advantages, there are some limitations for the use of fuel cells. For example, the short lifetime caused by impurities in the gas stream inlets, degradation and poisoning of the catalysts used as electrodes, slow kinetics to perform multi-electron charge transfer reactions, low density output power per unit volume and low accessibility are, to name a few, challenges to overcome. However, in the last years, a great progress in the development of this technology using novel catalysts and fuels aiming at optimizing the operation of fuel cells [2] has been made. Among the main fuel cells operation issues, we can find the high cost and availability of electrocatalysts, the degradation of the proton exchange polymeric membrane, and the oxygen reduction reaction (ORR) kinetics. This reaction takes place on the most active element, Pt, at an overpotential of around 0.3 to 0.4 V [3]. For this reason, fuel cells operate, in practice, at a much

lower potential relative to the theoretically possible and with a very low efficiency [4]. The ORR is, in fact, one of the most important reactions in electrochemistry because of its central action in metal-air batteries, electro-synthesis of hydrogen peroxide and the manufacture of cathodes for fuel cells [4]. The molecular oxygen reduction is ideally performed by a transfer mechanism of four electrons. A process involving a single step in which molecular oxygen is reduced to water [5]. Any new ORR electrocatalyst should be investigated to determine the ORR kinetics, since the H_2O_2 produced often causes the degradation of the polymer electrolyte membrane in the heart of proton exchange cells [5]. Nowadays, an important variety of precious metals are used as ORR electrocatalysts.

Platinum supported on carbon is usually used as an anode to conduct the oxidation reaction of hydrogen (HOR) as well as at the ORR at the cathode. It is well stablished that Pt is costly and very sensitive to the presence of contaminants [6]. Numerous strategies have been explored to reduce the mass loading and improve its activity. One of these strategies is the formation of Pt-alloys with 3d transition metals. These kind of alloys can also inhibit the formation of adsorbed species such as hydroxyl, Pt-OH [7]. The transition metal alloys of Pt with, e.g., Ir, Ru, Rh, Re, Os, increase substantially the electrochemical activity, reduce the mass loading, induce lower overpotentials, and promote the reaction of four-e^- [8]. A study carried out by Min et al. [9] considers that the electrochemical property of Pt and its alloys is a result of electronic factors. They suggested that the ORR kinetics increases with the decreasing vacancies in the 5d band of Pt, since such hybridization is less favorable as there is an increase in particle size, implying a decrease of the adsorption strength of the oxygen species. Mukerjee et al. [7] concluded that, on PtCo/C, PtCr/C, PtMn/C, PtFe/C, and PtNi/C alloys, the catalytic activity is increased by an electronic combination which produces changes in the vacancies of the d band, and alloy network contractions. Thus, better ORR properties were obtained on PtCr/C. Markovic et al. [10] reported the synthesis of two Pt-based materials; PtFe and PtCo nanowires. The PtFe electrocatalysts presented higher activity than PtCo toward the ORR due to a greater Co leaching from the alloy. The mass activity and specific surface of the PtFe nanowires were higher than the commercial platinum electrocatalyst. Besides the effect obtained by alloying with early or late transition metals, the electronic properties of Pt NPs can also be modulated by interaction with the support. Indeed, in recent years, exhaustive research activities have been conducted for searching active Pt structures to reach the Department of Energy (DOE) targets [11], which led to the development of many different types of alloys, often identified as skin-layer-, core-shell-, and thin film-electrocatalysts. Greeley et al. [12] has identified, by a density functional theory (DFT) computational screening, a skin-type Pt_xY catalyst as a promising cathode material for the ORR. In this connection, Pt_3Y alloys were the most stable Pt_3M alloys able to bind oxygen species slightly less than pure Pt, therefore showing a higher ORR activity [13]. The high stability of Pt_3Y alloy was attributed to the almost half-filling of the metal-metal d-band of the two alloyed metals, which corresponds to the bonding states filling, whereas the antibonding states are empty.

Another kind of electrocatalysts are the transition metal chalcogenides. Indeed, the substitution in a cluster compound of Ru by Mo atoms in Mo_6Se_8 led to a ternary chalcogenide, $Ru_2Mo_4Se_8$, with interesting properties toward the ORR in acid media [14]. These type of materials are metal clusters with octahedral centers where the delocalization of electrons provides a high electronic conductivity acting as reservoirs of electrical charges, while it remains kinetically stable [15]. Transition metal chalcogenides have also the ability to provide binding sites for the reactants neighbors and intermediaries, they possess also the property to change the volume and distance during the electronic transfer. As a result of these studies, the Ru has been positioned as one of the main electrocatalytic alternatives for the ORR: it is less noble than Pt and is oxidized at a potential 0.2 V more negative than Pt, and the oxides and also hydrides formed on its surface can act as a chemical oxidant for the CO adsorbed at a potential between 0.3 and 0.4 V more negative than pure Pt, this prevents its poisoning as occurs in the case of Pt [16]. Furthermore, it has been shown that Ru possesses good electrocatalytic activity and that combining it with other elements they show greater stability [17–20]. In the Ru_xSe_y material, the Se modifies the electrical properties of the active sites by synergistic effects facilitating the

electron transfer [21–24]. Other studies demonstrated that the presence of Mo and Ru atoms decreases the percentage of peroxide produced [25], the Sn reduces the ORR overpotential [26] and finally, the W facilitates the oxygen adsorption [27].

Another strategy to tailor the electrochemical ORR activity and reduce the amount of Pt is by replacing it with Pd, resulting in cheaper electrocatalysts with high ORR activity [28]. Pd has a valence electron configuration and a lattice parameter similar to Pt [29]. Furthermore, it is suggested that the oxygen reduction activity on Pt can be enhanced if Pd is used in combination with other elements which can improve the rate of the electro-reduction of oxygen [30] and the desorption kinetics of the ORR products. Pd is an element more abundant and also cheaper than Platinum; in addition, its stability in acid medium can be comparable with Pt. However, its performance to carry out the ORR is several times smaller in comparison to Pt and its alloys [31]. In order to enhance the catalytic activity of Pd catalysts for PEMFC (proton exchange membrane fuel cell), the particle size control [32], the structure [33], alloying metals [34] and supports [31] are crucial parameters to be considered. In general, the reactivity and selectivity of Pd catalyst for a certain catalytic reaction can be tailored by controlling their shape and thus the type of facets. Pd NPs perform the ORR in acid media and proceed preferentially via four-e^- [35], Pd-Ag, Pd-Cu alloys have shown catalytic activity for the ORR in acid medium with 2- and 4-electrons [36]. Recent reports have shown that Pd alloys such as $Pd_3Fe(111)$ have excellent electrochemical properties [37,38]. Similar studies prove that PdCo/C alloys display comparable activity to Pt/C towards the ORR in acid medium [39]. It has been suggested that the increased oxygen reduction activity of PdCo alloys might be attributed to a Pd electronic stabilization due to the addition of this last element [40]. The electrochemical activity of PdCo/C containing 10%–30% of Co presented a half-wave potential value of 0.66 V/RHE (reversible hydrogen electrode) while Pt/C showed an $E_{1/2}$ = 0.68 V/RHE. Both electrodes were evaluated in a 0.1 M $HClO_4$ solution [41]. Several studies have shown that the catalysts formed by the Pt-Pd alloy present a comparable activity comparable with pure Pt [42] due to the facility to modify the length of the lattice parameter depending on the Pt amount in the alloy in order to favor the highest oxygen adsorption over the catalyst surface [43]. Among the electrocatalysts with different Pt-Pd ratios, the $Pt_{30}Pd_{70}$ presented an onset potential 17 mV more positive than Pt indicating a faster kinetics. The $Pt_{30}Pd_{70}$ electrocatalyst is thermodynamically more active for the ORR than pure Pt as revealed recently by the density functional theory (DFT) studies [44]. This scenario, aside from ORR, another interesting reaction exists where Pd-based catalysts play an important role in the oxidation of organic molecules (methanol (CH_3OH) [45], and formic acid (HCOOH)) [46]. Pd-based electrocatalysts have been employed to oxidize methanol; nevertheless, besides their good electro-activity, those catalysts can overcome the effect of carbon monoxide-poisoning [47] with a high performance as anode catalysts in alkaline DMFC's. Pd-based catalysts show a higher tolerance than Pt to CO species however, the disadvantage of Pd-based catalysts is their lack of durability [48].

Under this scenario, many efforts have been made tailoring and improving the electrochemical activity and durability of Precious and Non-precious based catalysts to perform two of the most important electrochemical reactions in fuel cells; the hydrogen oxidation and the oxygen reduction reactions. In this work we emphasize the catalytic response of precious catalytic centers like Pt-, Pd-based electrocatalysts, and chalcogenides, synthesized via the carbonyl chemical route. We also present the catalytic performance of non-precious electrocatalysts produced via a free-surfactant chemical heating route. All these materials were tested towards the ORR and HOR. The selection of such materials was based on the experience that our research group has acquired in the synthesis methods and electrochemical evaluations. In addition, the electrocatalysts modification by the hybridizing process of some catalytic centers with some carbon and ceramic supports is discussed. Taking into account the most active materials synthesized in our laboratory, they were evaluated in a micro-fuel platform and the results were compared with the state of the art of the micro fuel cells domain analyzing the design, operating arrangements and conditions.

2. Materials Design

2.1. Precious Catalysts

Electrocatalytic materials in the nanodivided form can be obtained by the pyrolysis, in an organic solvent, of transition metal complexes [$M_y(CO)_x$] that contain a metallic cluster in their base structure, or using metallic salts and employing the carbonyl chemical route through the reactivity of carbon monoxide to achieve the chemical coordination of CO with a metal center in organic or aqueous solvents [49]. The physicochemical and catalytic properties of electrocatalysts depend directly on the chemical nature of the surface but also on their size and shape [50]. Due to its high feasibility and great potential to tailor electrocatalysts, the carbonyl chemical route has been extensively employed to produce active, and chemically stable electrocatalysts [50]. The carbonyl chemical route [51] involves the reactivity of metal carbonyls in solvents to obtain metallic clusters. It has been employed to synthesize Ru [49,52], Pt [49,53–55] and recently Pd-based [56,57] catalysts for electrocatalytic purposes.

2.1.1. Pt- and Pd- Based Electrocatalysts

The synthesis of carbonyl complexes was initiated by Longoni et al. [58]. These authors developed a process to produce the dianions $[Pt_3(CO)_6]_n^{2-}$ (n = 10, 5, 4, 3) from the reduction of several platinum precursors ($Na_2PtCl_6{\cdot}6H_2O$, $H_2PtCl_6{\cdot}xH_2O$, Na_2PtCl_4, $Pt(CO)_2Cl_2$) using various reducing agents (alkali hydroxides under carbon monoxide, $Fe(CO)_5$, cobaltocene, alkali metals). The n value of the final product depends greatly on the nature of the reagents and the experimental conditions, the reductive carbonylation proceeds as follows [58]:

$$[PtCl_6]^{2-} \rightarrow [Pt_3(CO)Cl_3]^{-} \rightarrow [Pt_3(CO)_6]_{10}^{2-}\ (\text{insoluble}) \rightarrow [Pt_3(CO)_6]_6^{2-}\ (\text{olive}-\text{green}) \quad (1)$$

$$[Pt_3(CO)_6]_5^{2-}\ (\text{yellow}-\text{green}) \rightarrow [Pt_3(CO)_6]_4^{2-}\ (\text{blue}-\text{green}) \quad (2)$$

$$[Pt_3(CO)_6]_3^{2-}\ (\text{violet}-\ \text{green}) \rightarrow [Pt_3(CO)_6]_2^{2-}\ (\text{orange}-\text{red}) \rightarrow [Pt_3(CO)_6]^{2-}\ (\text{pink}-\text{red}) \quad (3)$$

The reactivity of these complexes depends on the value of n and generally, the trend was that increasing n results in an increase in the reactivity towards nucleophilic and reducing agents, while decreasing n results in an increase in reactivity towards electrophiles and oxidizing agents.

For Pt-based electrocatalysts, this method was modified in our group and can be shortly described as follows: the platinum carbonyl $[Pt_3(CO)_6]_5^{2-}$ was prepared by mixing specific quantities of $Na_2PtCl_6{\cdot}6H_2O$ with sodium acetate (mol ratio of NaAc/Pt = 6) in methanol solution under CO atmosphere, for 24 h. Activated carbon Vulcan XC-72 was aggregated to the previous solution and stirred for another 12 h under nitrogen atmosphere. The product, nanostructured Pt/C, was washed, filtered and dried [50]. The above process is shown in the reaction (4) [51].

$$[Pt_3(CO)_6]_{10}^{2-} + M_yX_n \rightarrow [Pt_xM_y(CO)_z] \rightarrow Pt_xM_y \quad (4)$$

where M = Sn, Ni, Cr, Co, and X = Cl^-.

Based on these previous studies, CO tolerant carbon supported anode bimetallic electrocatalyst Platinum-Tin (Pt_3Sn) was developed [59]. Figure 1a,b schematize the process established by Longoni and Chini [58], and by Alonso-Vante's group [59], respectively. It is important to mention that the process followed by Longoni and Chini stops at step 4. The advantage of the reactivity of the cluster complex is that careful handling the platinum complex, can be taken to deposit the Pt nanoparticles over several supports (step 5). In this case, by depositing carbon black (Vulcan XC-72) Pt/C, can be obtained.

As a result of this synthesis modification, it was found that commercial Etek catalysts presented a broader particle size than the homemade Pt-Sn produced also by the carbonyl chemical route, Figure 2.

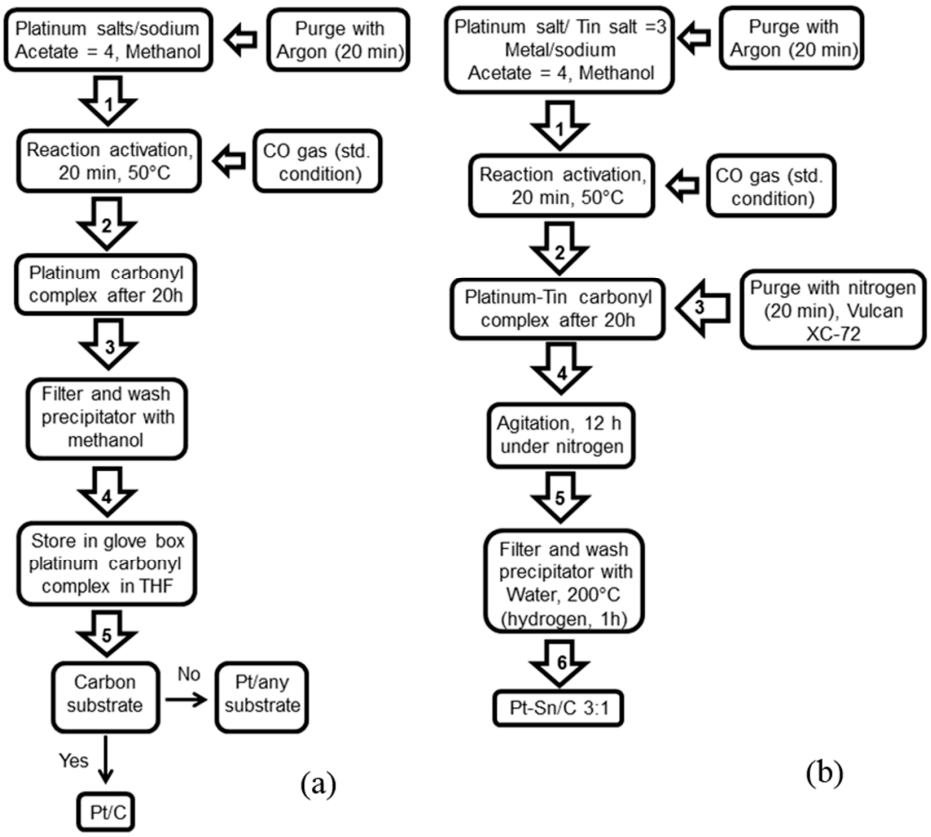

Figure 1. Pathways to obtain Pt (**a**); and Pt-based electrocatalysts (**b**) by carbonyl chemical route.

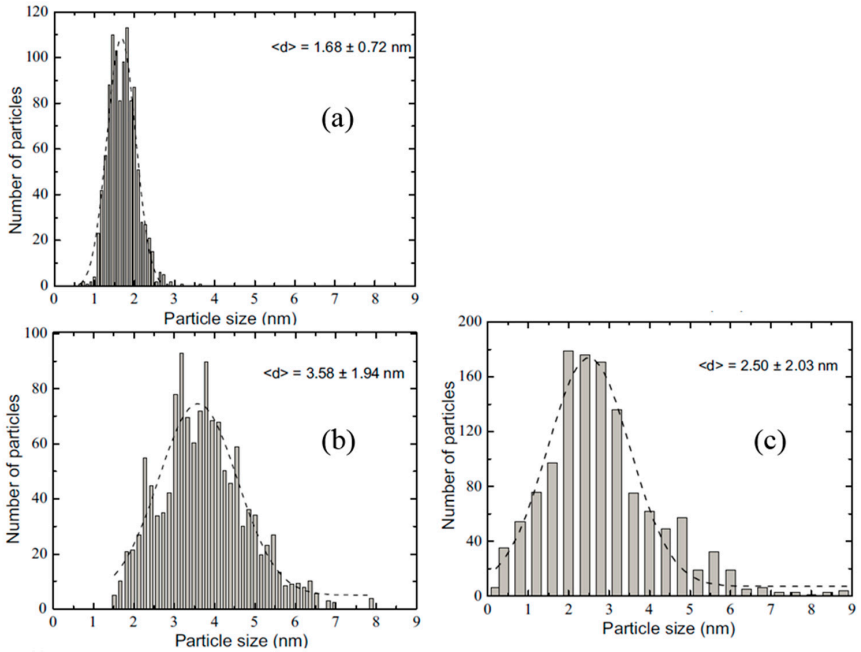

Figure 2. Particle size of the electrocatalysts (**a**) Pt-Sn/C (carbonyl route); (**b**) Pt-Sn/C Etek; and (**c**) Pt/C Etek [59] obtained by TEM (transmission electron microscopy). The <*d*> parameter was determined by a Gaussian distribution. Reprinted with permission from [59]. Copyright John Wiley and Sons, 2002.

In the same line, further bimetallic nanoalloys, e.g., carbon-supported well dispersed Pt-Ni; and Pt-Cr alloys were obtained [54,55]. In this latter, $CrCl_3$ was used with a final heat treatment from 200 °C to 500 °C. The lattice parameter presents an inversely proportional relation with the content of

Cr (Pt/C Etek 0.3923 nm, Pt:Cr (3:1) 0.3895, Pt:Cr (2:1) 0.3863 and Pt:Cr (1:1) 0.3817) [54]. Pt-Cr showed an enhancement factor of 1.5–3 in the mass activity (MA), and in the specific activity (SA), Figure 3; because of the changes in this lattice parameter and the Pt-Cr composition.

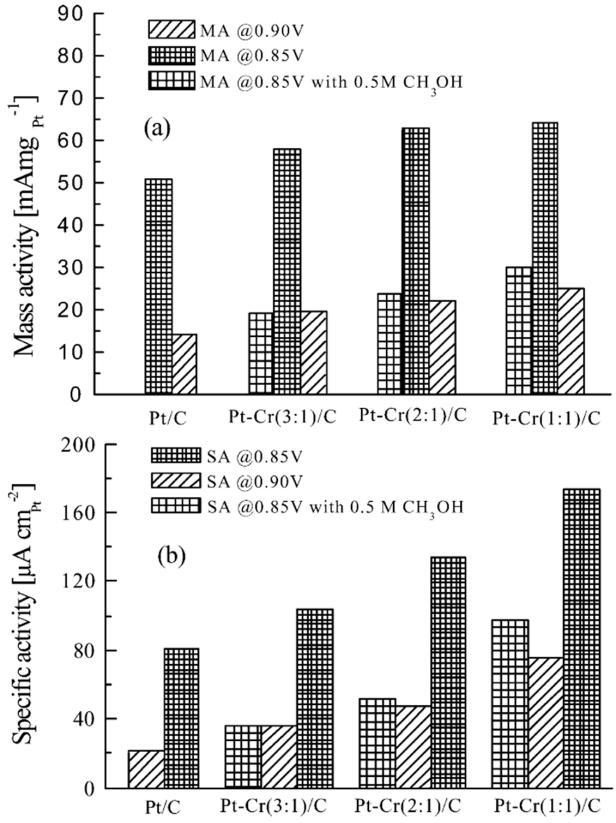

Figure 3. (**a**) Mass activity (MA) and (**b**) specific activity (SA) histograms for the Pt-based materials towards the oxygen reduction reaction (ORR). 0.5 M $HClO_4$ was used as electrolyte [54]. Reprinted with permission from [54]. Copyright American Chemical Society, 2004.

For Pt-Ni, the wide angle X-ray spectroscopy patterns, and the Debye function analysis showed that the as-prepared Pt-Ni electrocatalysts presented face-centered cubic structure and that the lattice parameter is reduced with the increase of Ni [55]. More important, both Pt-Cr and Pt-Ni alloys showed high tolerance to methanol than the Platinum electrocatalyst, Figure 4.

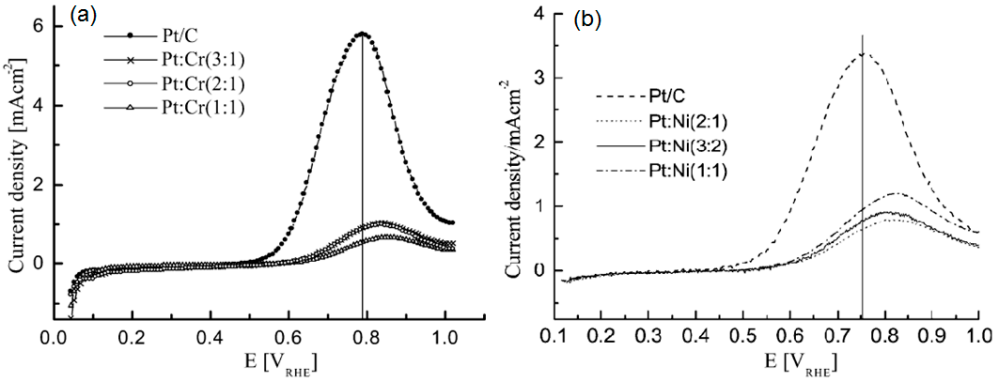

Figure 4. Methanol oxidation comparison for (**a**) Pt-Cr (reprinted with permission from [54]. Copyright American Chemical Society, 2004 and (**b**) Pt-Ni (reprinted with permission from [54]. Copyright Elsevier, 2005 in a 0.5 M $HClO_4$ + 0.5 M CH_3OH outgassed solution. The test conditions were: Scan rate υ = 5 mV/s, and a rotating disk rate of 2000 rpm [54,60].

To explore the effect of the support material onto Pt NPs the synthesis of platinum supported on Vulcan-carbon (Pt/C) and multi-walled carbon nanotubes (Pt/MWCNTs), via the carbonyl chemical route, was done [61]. After 20 V cycles (CVs) from 0.05 to 1.2 V/RHE, an improved stability was obtained with Pt/MWCNT in comparison to Pt/C. This kinetics and stability improvement were attributed to a higher graphitization degree of MWCNT support, leading to an increased strength of the π-sites with the MWCNTs acting as anchoring centers for Platinum nanoparticles [62]. Furthermore, this interaction also limited the agglomeration of Pt nanoparticles.

Through a modification of the classic carbonyl chemical route, the synthesis of carbon supported Pt-Ti nanoparticles was performed [63]. For the chemical composition, a post heat treatment process on the distribution of the particle size, and also on the electronic properties of Ti and Pt atoms on the performance on the oxygen reduction, and the methanol tolerance were done. The catalytic activity and selectivity towards methanol showed a remarkable enhancement for the nanoalloyed structure. The improvement was caused by the annealing at 875 °C as a result of the alteration of the density of electrons present in the platinum *d*-orbitals modifying the strength of the oxygen adsorption. In consequence, the arrangement of a surface alloy with a high order degree is the responsible to mediate the methanol poisoning of platinum sites [63].

The carbonyl chemical route was further explored to synthesize, for the first time ever, carbon supported Pd NPs supported for the ORR [57]. Herein, K_2PdCl_6 and sodium acetate were used as precursors reacting with CO. All of them were dissolved in CH_3OH, a step which was the key in the modified process because this reaction has to be performed for 2 h in an ice-bath, in this way the reaction rate was decreased avoiding the agglomeration of particles during the complex formation. Thereafter, the process continued following the classical route. The synthesis process comparison for platinum- and palladium-based nanomaterials via carbonyl chemical route is contrasted in Figure 5.

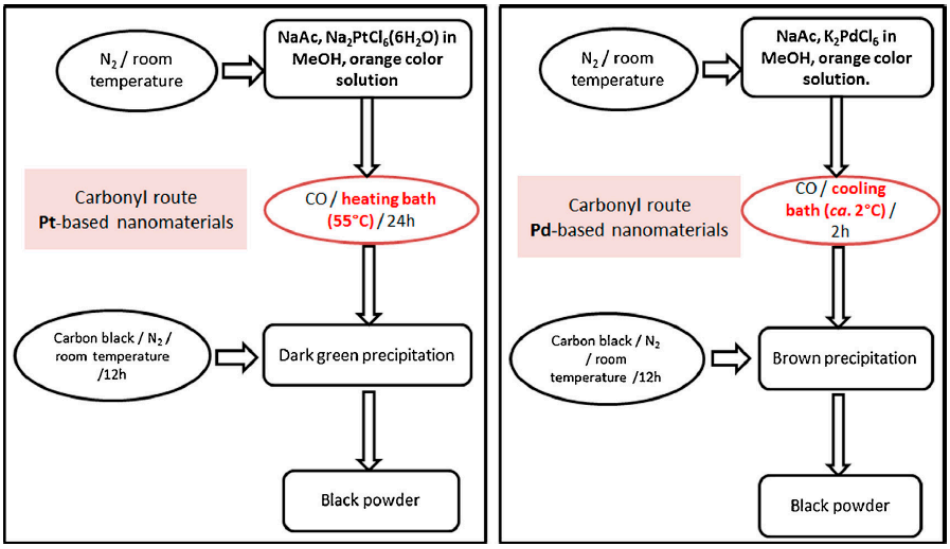

Figure 5. Process diagrams for the synthesis via the carbonyl route of platinum- and palladium-based electrocatalysts [57]. Reprinted with permission from [57]. Copyright Elsevier, 2015.

As a result of this process, Pd samples showed metal mass-loading dependent morphologies. In 10 wt % Pd/C, Pd NPs were highly agglomerated on the carbon support. In Figure 6a, we can find many particles with an average diameter higher than 10 nm. For 20 wt % Pd/C, large amounts of Pd nanowires could be observed, see Figure 6b. In Figure 6c, it is possible to observe Pd nanorods which present an average diameter of 3 nm, these nanorods were well dispersed on the carbon support presenting a total composition of 30 wt % Pd/C. In Pd/C-4, the nanoparticles were almost agglomerated, Figure 6d. In comparison with platinum-based catalysts obtained by the carbonyl

chemical route, the morphology of the palladium electrocatalysts changed depending on the metal mass loading [57].

The importance of this study lies in the description to control the morphology of palladium nanoparticles depending of the metal loading following the carbonyl route.

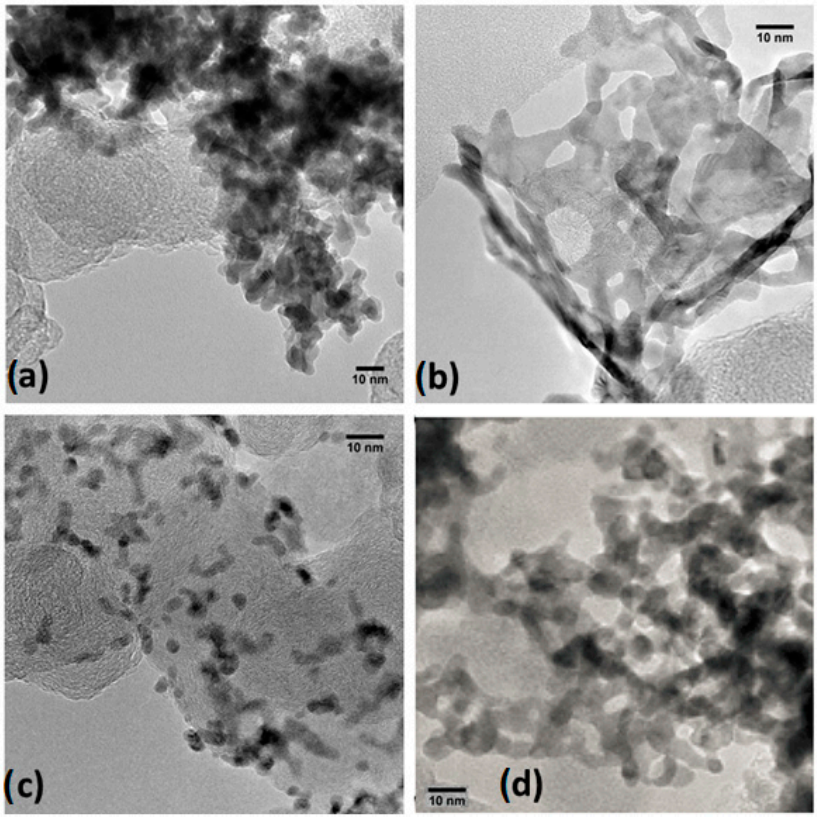

Figure 6. TEM images for (**a**) Pd/C 10%; (**b**) Pd/C 20%; (**c**) Pd/C 30% and (**d**) Pd/C 40% electrocatalysts.

2.1.2. Transition Metal Chalcogenides

Transition metal chalcogenides are promising materials in the field of catalysis and photo-electrocatalysis, since they combine the properties of electrically conducting materials with the catalytic advantage of molecular metal-clusters [64]. In the 70s, various research groups developed the so-called Chevrel phases such as M_6X_8 (M = Mo; Re, X = S, Te and Se), having exceptional superconducting properties [65]. Perrin et al. [66] reported the synthesis and properties of $Mo_xRe_ySe_z$ and $Mo_xRe_yTe_z$ but also $Mo_xRu_ySe_z$, $Mo_xRu_yTe_z$ and $Mo_xRh_yTe_z$ [67]. The authors found that molybdenum sulfide phases and those with mono or divalent elements, a rhombohedric structure with a triclinic deformation predominated. They assumed that Mo and Re d-electron bands were responsible for the electrical superconductivity in these materials. All these samples were prepared by a direct synthesis from the elements in evacuated quartz ampoules, heated up to 1200 °C. The generated samples were ground and annealed at the same temperature for 24 h. To obtain the sulfide compounds, it was necessary to let the reaction take place near 1300 °C, and several subsequent heat treatments were necessary in order to get a pure sample. For selenide and the telluride clusters the synthesis was easier. In order to evaluate and manipulate the samples, the powders were converted into pellets and finally sintered [66,67].

The use of such transition metal chalcogenides ($Mo_{4.2}Ru_{1.8}Se_8$) as electrocatalysts for the oxygen reduction in acid medium was reported in 1986 [68]. The authors reported the first test of such materials to perform the ORR with an appreciable cost advantage with respect to platinum [68]. It was further assessed that the $Mo_{4.2}Ru_{1.8}Se_8$ cluster, in powder form fixed on supports with the help of of Nafion® ionomer thin film, onto glassy carbon, Figure 7a, and on p-type gallium phosphide

(p-GaP) semiconductor, Figure 7b, favored the ORR, and hydrogen evolution reaction (HER) under Visible illumination [69]. $Mo_{4.2}Ru_{1.8}Se_8$ clearly enhanced both processes. On p-GaP surface the photo- induced hydrogen evolution was maintained. The limiting currents were reduced by only 3% at −0.56 V (vs. SHE). This was quite remarkable and suggested (now a phenomenon well established) that hydrogen, besides protons, can penetrate the Nafion layer easily, curve 3, in Figure 7b. The flat-band potential of the unmodified electrode was determined to be 0.94 V vs. SHE and was not shifted as a consequence of attachment of the Nafion film and the cluster particles.

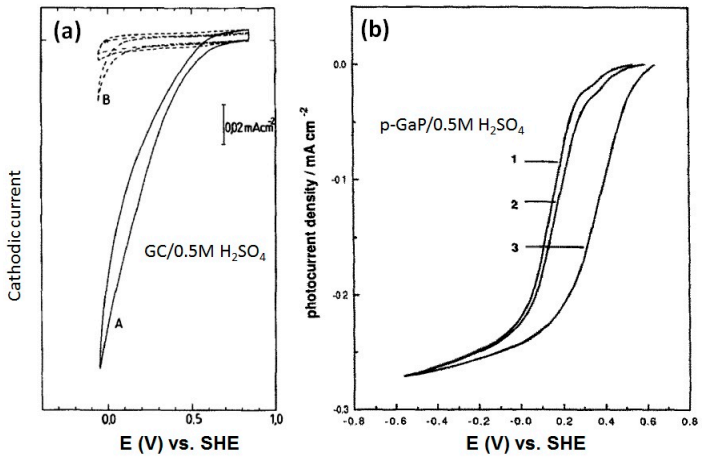

Figure 7. Linear scan voltammograms for the ORR (oxygen reduction reaction) and photo-evolution of hydrogen of the Nafion-attached cluster chalcogenides. (**a**) Glassy Carbon at 50 mV/s; and (b-curve (3)) p-GaP. Curve (B), in (**a**), is the unmodified GC surface. In (**b**), curves (1, 2) represent Nafion unmodified, and modified p-GaP surfaces. Scan rate = 5 $mV \cdot s^{-1}$. Adapted from [69].

Summing up, the $Mo_{4.2}Ru_{1.8}S_8$ cluster employed as a model catalyst for multi-electron reduction processes for the ORR, was not suitable for multi-electron oxidation processes—the oxygen evolution reaction (OER), due to insufficient kinetic stabilization [69]. Based on previous works [70,71], a certain degree of kinetic stabilization can be accomplished with chalcogenides, which can permit a photoreaction of holes via transition-metal d-states which are not significantly mixed with chalcogen states. Regarding the electrochemical activity towards the ORR, $Mo_{4.2}Ru_{1.8}S_8$, Figure 8, a pseudo ternary cluster, outperformed the ternary clusters, e.g., $Ni_{0.85}Mo_6Te_8$, where Ni atoms occupies the free sites in the channels between the Mo-clusters. Two main positive effects on the pseudo ternary compound were claimed, namely, the increase of metal-metal distance in the cluster, thus possibly facilitating the breaking of the –oxygen–oxygen– bond liberating OH^- ions. The expected shift of the electronic levels upwards was caused by the increase of the charge in the cluster.

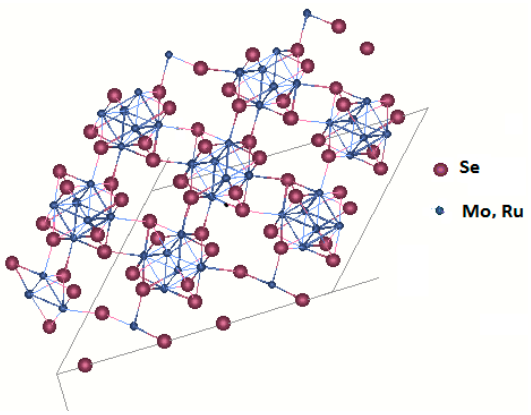

Figure 8. Structure of a pseudo ternary cluster $(Mo_4Ru_2)Se_8$.

Because the catalytic properties and the high density of *d* states at the Fermi level can be related, this relation on $Mo_4Ru_2Se_8$, $Mo_2Re_4Se_8$, Mo_6Se_8, and the Mo metal was undertaken [72]. Indeed, Mo_6Se_8 showed metallic properties, whereas $Mo_4Ru_2Se_8$ and $Mo_2Re_4Se_8$ showed semiconducting properties. The explanation lies on the fact that the substitution of Mo by Re and/or Ru atoms, that contain a high valence electron number, causes an increment of the electrons from 20 to 24 in the cluster M_6X_8, resulting in a filling of the e_g band. This effect shifts upwards the Fermi level, as schematized in Figure 9.

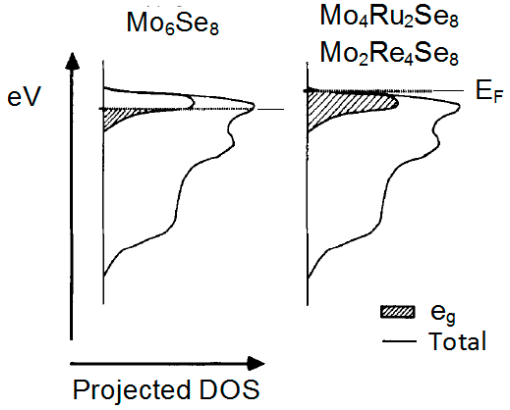

Figure 9. Band structure scheme of chalcogenide clusters. Adapted from [72,73]. Reprinted with permission from [72]. Copyright Elsevier, 1988.

These compounds were evaluated towards HER and ORR. As a result of the narrow energy band caused by the *d*-state density, some improvement was observed on the HER, with a significant influence on ORR. This study revealed that hydrogen species solely interact with individual metal atoms, the molecular oxygen interacts with the atoms M, and M' in the $(MM')_6X_8$ cluster [74], as shown in Figure 10, thus forming a surface transition metal complex. Based on the statistics of the calculated possible combinations and taking again into account the density of *d* states, the complex IV must play a major role in the ORR electrocatalytic materials activity.

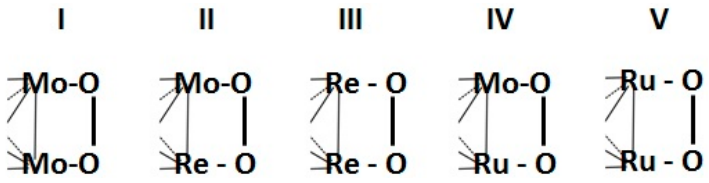

Figure 10. Surface transition metal complexes and their bridge-type, interaction with the chemisorbed oxygen, modified from [72]. Reprinted with permission from [72]. Copyright Elsevier, 1998.

Based on these Chevrel phase model compounds, prepared in quartz ampoule at high temperature [67], Mo-Ru-Se, in powder and/or in thin layer form, was synthesized via a soft chemical method; the carbonyl chemical route by reacting molybdenum hexacarbonyl, tris-ruthenium dodecacarbonyl and selenium powder in xylene [75]. The XPS (X-ray photoelectron spectroscopy) characterization revealed the presence of SeO_2 and MoO_3, Figure 11. After cathodic electrochemical treatment, in presence or absence of oxygen at 0.35 V during 5 min in 0.5 M H_2SO_4, the emission line for SeO_2, disappears and the MoO_3, emission line is strongly reduced, see curves (2) in Figure 11, indicating that the catalysts still contain a small amount of Mo. Exposed to air for more than 100 days, curves (3), the MoO_3 species is further reduced to a minimum in comparison to the shortly treated electrode, curves (2). The absence of SeO_2, species demonstrates a higher stability than Chevrel phase compounds against oxidation under oxygen atmosphere [13].

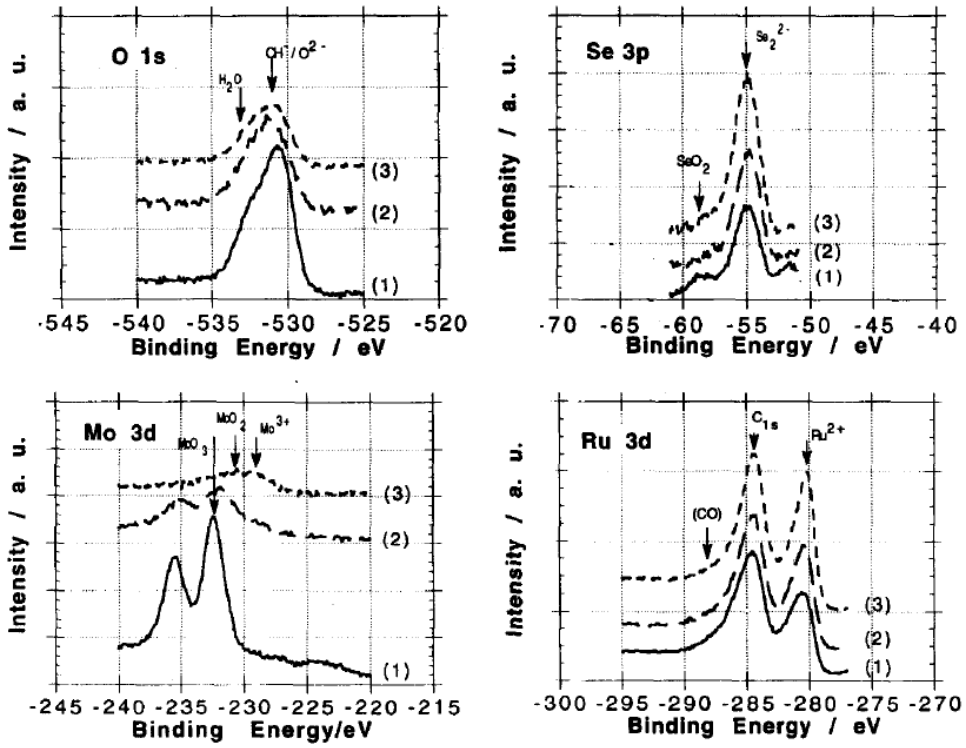

Figure 11. XPS (X-ray photoelectron spectroscopy) spectra of $(Ru_{1-x}Mo_x)_ySeO_z$ at different conditions; (1) as prepared sample in xylene solution; (2) polarized sample at +0.35 V/NHE (5 min) in 0.5 M H_2SO_4; and (3) after ORR and kept in air approximately 100 days. Reprinted with permission from [75]. Copyright Elsevier, 1994.

The Extended X-ray absorption fine structure spectroscopy (EXAFS) disclosed that chemically generated Mo-Ru-Se electrocatalysts were, structurally speaking, different to that of the Chevrel phase compound [64]. It was concluded that the Mo and Ru atoms, in Mo-Ru-Se, were located as independent phases: $MoSe_x$, MoO_x and $RuSe_x$ [76]. They, however, showed high selectivity to perform the ORR, in a solution containing methanol, with a four-electron reaction pathway, with an activity nevertheless, lower than that of the standard Pt catalysts in methanol-free electrolyte [77].

A further characterization by X-ray diffraction at wide angles (WAXS) of Ru_x and Ru_xSe_y was carried out [78]. Indeed, chalcogenide particles produced from the reaction between $Ru_3(CO)_{12}$ and Se were more resistant to oxidation than monometallic Ru_x nanoparticles with similar size. This phenomenon was associated to the coordination of Selenium atoms over the ruthenium atoms surface. As revealed by EXAFS analysis [79,80] the closest Ru-Ru averaged distance was 2.64 Å (corresponding to the *hcp* phase of metallic ruthenium) and that of the metal chalcogenide Ru-Se was 2.43 Å. It is worth noting that the calculated Debye-Waller parameters were a factor of 2 higher for the Ru-Se coordination distance than for Ru-Ru. Considering a particle diameter of 17 Å a pure ruthenium cluster-like model particle was developed containing 153 atoms (Ru_{153}). This is the third species in a series of *hcp* closed shell clusters with "magic" numbers 13, 57, 153, 323, etc. Therefore, within the *hcp* cluster model (17 Å particle size, 153 atoms), the number of ruthenium atoms available for electrocatalytic purposes at the surface of such cluster can be $153 - 57 = 96$. Because $x = 2$ and $y = 1$ in the chalcogenide material, Ru_xSe_y, the cluster model contains 99 Ru atoms and 54 Se atoms, with an increased disorder of selenium atoms, deduced from EXAFS calculations [79], almost all selenium atoms are coordinated to ruthenium atoms on the cluster in a statistical way, as shown in Figure 12. In this way, the Ru-clusters surface coverage by Se atoms induces the necessary free active sites (Ruthenium sites) to perform an efficient coordination with oxygen/water [78].

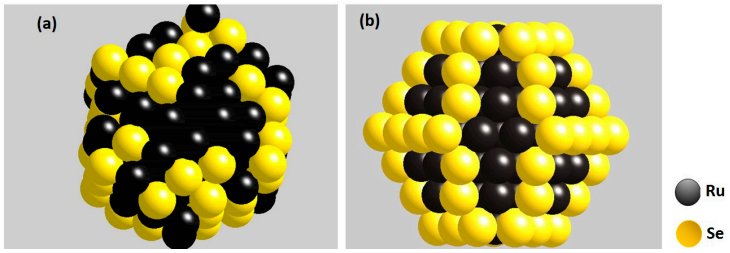

Figure 12. *hcp*-Cluster Model structures for $Ru_{99}Se_{54}$; (**a**) Se statistically bonded onto the Ru clusters; (**b**) Se replacing Ru surface atoms in an ordered positioning with 5-, 6-, and 7- fold coordinated.

The use of selenium atoms to coordinate catalytic center surface atoms, as well as impinging on it electronic modification was demonstrated for ruthenium in Ru_xSe_y [81]. This concept was further applied onto platinum, generated via the carbonyl chemical route [82]. The surface Pt NPs in Pt/C was modified with Se (selenization process). Platinum supported on carbon and SeO_2 were mixed in isopropanol solution with specific quantities and stirred for 12 h at room temperature. This mixture (20 wt % Pt_xSe_y/C) was heat-treated (200 °C) for 1 h under a nitrogen atmosphere. In order to account the optimal amount of Se atoms, to allow the adsorption and subsequent reduction of O_2 molecules, Se was concomitantly stripped from the Pt surface using Chronoamperometry at different stripping times, at an established anodic potential. Employing a stripping time of 20 min at 1.1 V/RHE, the ORR half-wave potential ($E_{1/2}$) shifted to positive values, whereas the OCP (open circuit potential) remained constant. The optimal Se coverage (see arrow in Figure 13a) kept to a maximum the ORR in the presence of methanol [83]. The partial leaching of Se atoms from the Pt surface improved the activity of Pt_xSe_y/C towards the oxygen reduction, with a high tolerance as compared to Pt/C, Figure 13.

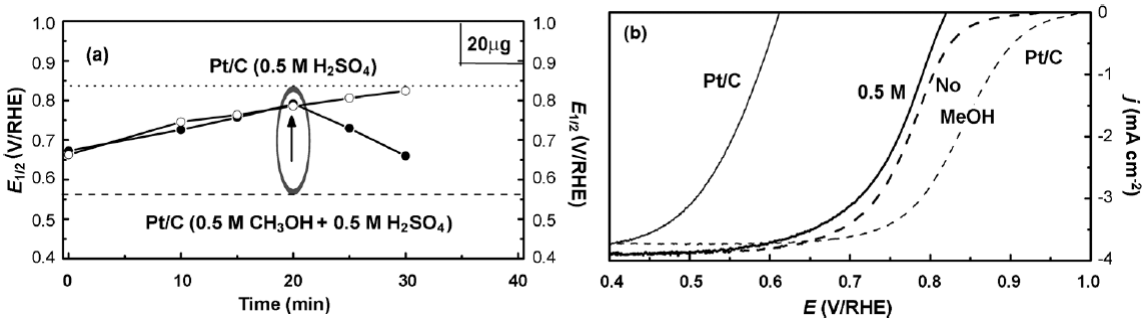

Figure 13. (**a**) Pt_xSe_y/C (20 mg of 20 wt %) ORR half-wave potentials compared to Pt/C (dotted lines). Both electrocatalysts were evaluated at 900 rpm in oxygen-saturated 0.5 M H_2SO_4 + 0.5 M CH_3OH (filled circles, left axes) and 0.5 M H_2SO_4 (empty symbols, right axes). (**b**) Linear scan voltammetries for the same test [83]. Reprinted with permission from [83]. Copyright John Wiley and Sons, 2013.

2.2. Non-Precious Catalysts

Despite the efforts carried out in the production of novel and efficient electrocatalyst, platinum-based materials are still one of the most efficient oxygen reduction catalysts employed in PEMFCs [84]; however, their high cost, low abundance and poor durability are a main obstacle in the development of PEMFCs [85]. To overcome these issues, the search of non-precious metal ORR catalysts has been extensively conducted in recent years [86]. Pt-free catalysts such as transition-metal chalcogenides have shown promising activities towards fuel cell reactions [51]. Co and Fe are also promising cathodic catalyst centers [87]. In recent studies, researchers have focused their efforts on two kinds of non-precious metals as catalytic centers: Co and Fe, and transition-metal chalcogenides with application in the ORR [88].

The development of new non-precious electrocatalyst dates back to the seventies with Co_3S_4 and $Me^{(a)}Me_2^{(b)}X_4$ ($Me^{(a)}$ = Mn, Fe, Co, Ni, Cu or Zn, $Me^{(b)}$ = Ti, V, Cr, Fe, Co or Ni, X = O, S, Se or Te). This material showed the highest catalytic activity for the oxygen reduction in a 1 M H_2SO_4 solution, and presented an open circuit potential of ca. 0.8 V vs. HRE [87]. However, Co_3S_4 was not close to the catalytic activity of Pt. Based on this work other Co-based materials [89–93] came into light. Feng et al. [94] synthesized three Co_3S_4 (-01, -02 and -03) compounds following different methodologies. Co_3S_4-01 was produced from a $Co_2(CO)_8$ decomposition in a mixture solution which contained tri-octylphosphane oxide and oleic acid as surfactants, just after sulfur and cobalt particles were reacted and deposited over the carbon substrate [91]; Co_3S_4/C-02 was prepared following the same synthesis procedure for Co_3S_4-01 but without the use of surfactants. Co_3S_4/C-03 was synthesized by means of a microwave-assisted process [94]. Co_3S_4/C-02 and Co_3S_4/C-03 synthesized without surfactant showed the highest activity toward the ORR, Figure 14. This work suggested that the surfactants, used in the synthesis of Co_3S_4/C-01, block the electrocatalyst active sites. These results demonstrated that routes without the surfactants were effective methods to produce non-precious catalysts supported onto carbon [94].

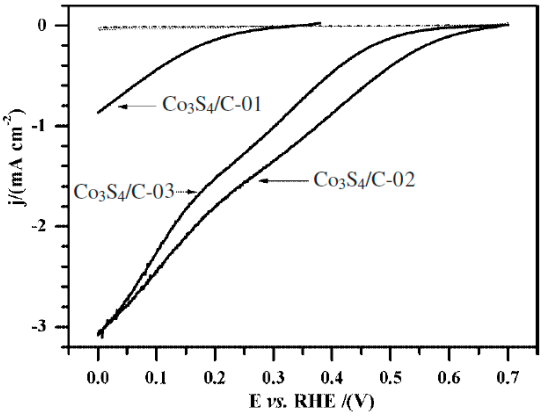

Figure 14. Linear scan voltammograms of 20 wt % Co_3S_4/C-01, -02, and -03. Rotation rate = 1600 rpm in an oxygen saturated 0.5 M H_2SO_4 solution at 25 °C. υ = 5 mV s^{-1} [94]. Reprinted with permission from [94]. Copyright American Chemical Society, 2008.

In modifying and upgrading the Co-Se electrocatalysts synthesis, $CoSe_2$ nanoparticles with different nominal loading from 20 wt % to 50 wt % were produced [95] via conventional heating process [94]. In short, for the synthesis of 20 wt % $CoSe_2$/C, $Co_2(CO)_8$ and Vulcan carbon were well dispersed in *p*-xylene under a nitrogen atmosphere at 25 °C for a half-hour. This suspension was heated and refluxed, and then cooled down. Thereafter, a specific amount of selenium was dispersed in *p*-xylene and stirred half-hour. Both suspensions were mixed, heated, and refluxed for 10 min. The final product was filtered, washed, and dried under vacuum at 25 °C. All $CoSe_2$/C electrocatalysts with different nominal ratio were heat-treated at 300 °C under high purity N_2 for 3 h.

The oxygen reduction cathodic current obtained for 20 wt % $CoSe_2$/C was in agreement to the results reported in previous works for non-precious metallic electrocatalysts (ca. 2.5 mA·cm^{-2} at 0.4 V at 1600 rpm) [96–98]. Some data from the literature were 2.0 mA·cm^{-2} for $Co_{1-x}Se$/C (50 wt % Cobalt on Vulcan carbon) [96], and 2.5 mA·cm^{-2} for (Co, Ni)S_2 thin films [98] at 2000 rpm. The OCP value of 0.81 V in oxygen-saturated 0.5 M H_2SO_4 surpassed the $Co_{1-x}Se$/C [96], and FeS_2 (0.78 V) [97]. The OCP was quite similar to that of NiS_2 (0.80 V), and CoS_2 (0.82 V) [98], but not better than that of (Co, Ni)S_2 (0.89 V) [98].

The electrode loading effect of $CoSe_2$ (from 11 μg·cm^{-2} to 44 μg·cm^{-2}) was investigated via the rotating ring disk electrode (RRDE) technique, Figure 15a. In this experiment, the disk current increased at an electrode potential of 0.5 V from 2.5 to 3.8 mA·cm^{-2} by the increase of the catalyst loading, with a concomitant decrease of H_2O_2% generation (at ca. 0.32 V). The variation of the mass

loading as a function of the peroxide production can be interpreted in terms of an increase of the active sites in the electrocatalyst. In other words, the H_2O_2 has additional time to react to water in a thicker layer. As a result of this effect, an increase in the total number of electrons, and a decrease in the hydrogen peroxide was detected at the ring electrode. Similar results on galena and pyrite materials were observed by Ahlberg et al. [99]. The authors found 25%–30% H_2O_2 production at the disk electrode. On the other hand, in Figure 15b we can observe the influence of 20 wt %, 35 wt %, and 50 wt % $CoSe_2$/C systems on the oxygen reduction activity and the hydrogen peroxide generation. Since the hydrogen peroxide generated on the surface of the ring electrode decreases from 30% to 15% when the loading rate is changed from 20 wt % to 50 wt %, there must exist a limiting catalytic site density. A similar trend was observed in other systems, e.g., 20 wt % Ru_xSe_y/C, which overpasses the current density of 70 wt % Ru_xSe_y/C [100], including Pt/C [101].

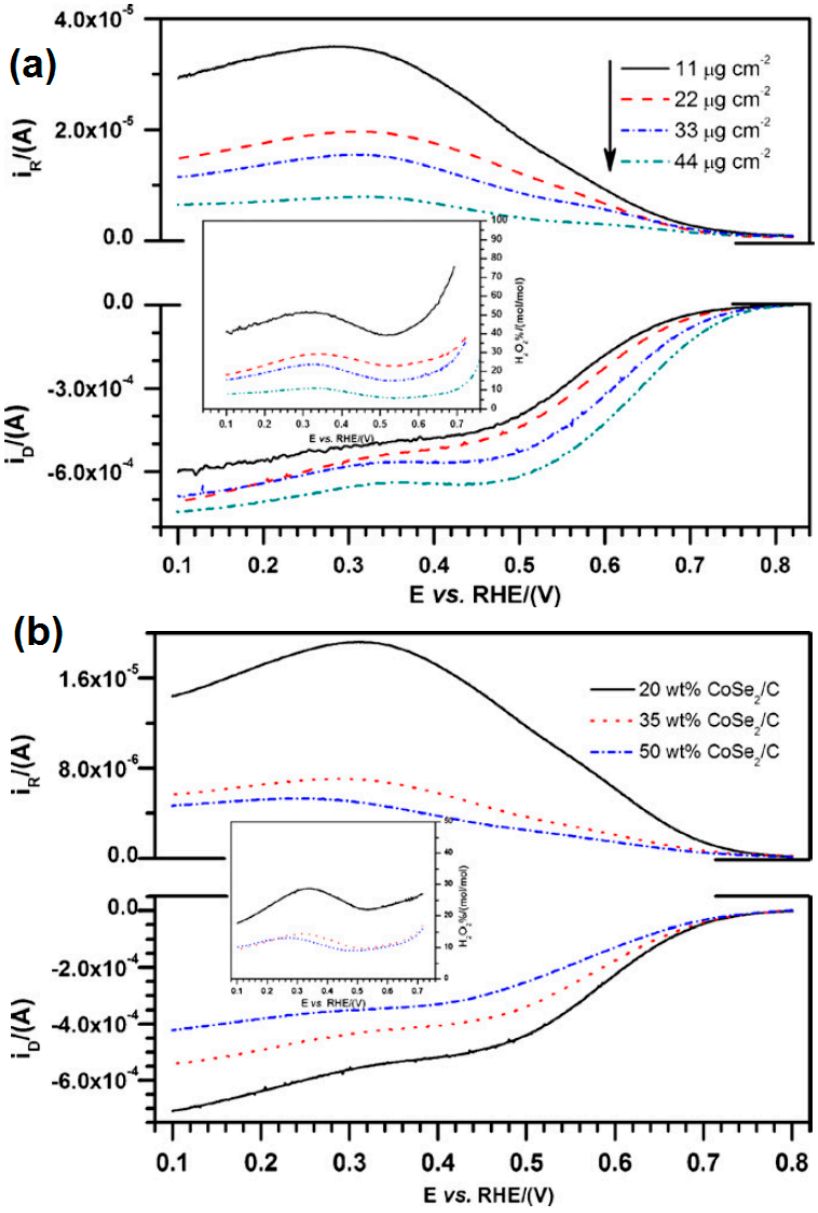

Figure 15. Linear scan voltammograms for the ORR and the formation of peroxide hydrogen (insets); (**a**) Electrode loading effect of $CoSe_2$ (from 11 μg·cm^{-2} to 44 μg·cm^{-2}); (**b**) Influence of 20 wt %, 35 wt %, and 50 wt % $CoSe_2$/C systems on the ORR activity and the H_2O_2 production [95]. Reprinted with permission from [95]. Copyright Elsevier, 2009.

Besides the ORR activity on the Co-Se system, the methanol tolerance was further investigated in alkaline medium [102]. Without surprise, the $CoSe_2$ nanocatalyst performance in alkaline medium is better than that in acid medium revealing further that the carbon-supported cubic phase of $CoSe_2$ is a promising non-precious electrocatalyst for alkaline fuel cells [103]. Furthermore, the oxygen reduction activity of 20 wt % $CoSe_2$/C in 0.1 M KOH was slightly higher than that of Co_3O_4/rmGO (reduced mildly oxidized graphene oxide) and comparable to that of Co_3O_4/NrmGO (nitrogen-doped mildly oxidized graphene oxide) as reported by Liang et al. [104]. Apropos methanol tolerance, Figure 16 contrasts the ORR curves of 20 wt % $CoSe_2$/C with that of 20 wt % platinum supported on carbon in oxygen-saturated 0.1 M KOH containing methanol. For Pt/C, the onset potential shifts negatively from 1.0 to 0.6 V, with an oxidation peak observed at ca. 0.65 V when the methanol concentration increased from 0 to 5 M. For 20 wt % $CoSe_2$/C, the onset potential remains unchanged and no oxidation peak is observed testifying immunity to methanol. At $j = -3$ mA·cm^{-2}, however, the potential shifts from 0.68 V to 0.62 V for 20 wt % $CoSe_2$/C catalyst, suggesting that methanol species in alkaline medium perturb the ORR. Nevertheless, the results herein show that 20 wt % $CoSe_2$/C presented an improved selectivity to perform the oxygen reduction reaction in presence of methanol than Pt/C electrocatalyst in alkaline medium. However, $CoSe_2$ is not hundred percent tolerant to methanol.

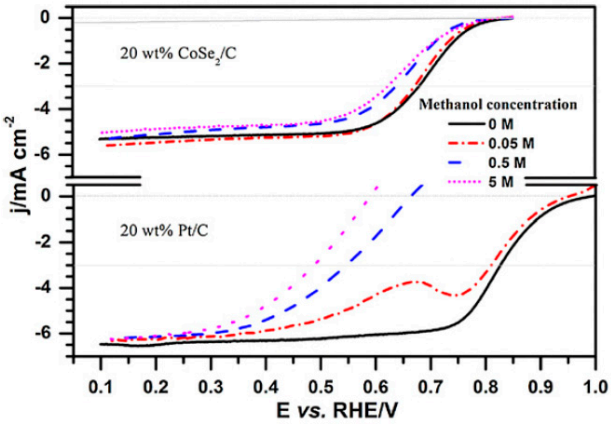

Figure 16. Methanol effect comparison $CoSe_2$/C and commercial Pt/C from E-TEK towards the oxygen reduction at concentrations of 0, 0.05, 0.5 and 5 M CH_3OH and a rotating speed conditions of 2500 rpm in an oxygen saturated 0.1 M KOH solution at 25 °C [102]. Reprinted with permission from [102]. Copyright Elsevier, 2012.

3. Fuel Cell Reactions

3.1. Hydrogen Oxidation Reaction—HOR

The electrocatalysis of hydrogen is a central issue in low temperature membrane fuel cells (PEMFC). H_2 is oxidized at the anode electrode:

$$H_2 \rightleftharpoons 2H^+ + 2e^- \quad (5)$$

The HOR largely depends on the strength of the intermediate interaction and bonding of metal and adsorbed hydrogen atoms [105]. As a consequence, the binding energies of the adsorbed hydrogen to the surface should always be in a range of an adsorption energy. A stronger bond would hamper the catalysis process by reducing surface dangling states and active sites, while a weaker bond could possibly indicate an inert electrode surface character with low number of dangling states and unsuitability of electrode for the catalysis [106]. Equation (5) can be represented by the following microscopic steps:

$$H_2 \rightleftharpoons 2H_{ad} \qquad \text{Tafel} \quad (6)$$

$$H_2 \rightleftharpoons H_{ad} + e^- + H^+ \qquad \text{Heyrovsky} \tag{7}$$

$$H_{ads} \rightleftharpoons H^+ + e^- \qquad \text{Volmer} \tag{8}$$

So, that the overall reaction can be revealed knowing some parameters, such as the exchange current density, activation energy, charge transfer coefficients, and Tafel slope. In PEMFCs the mass loading reduction of the expensive Pt is required to catalyze the HOR. Significant efforts have been made on the potential use of partial or complete replacement of Pt electrocatalyst at the cathode [107–109].

For the replacement of the most common based on platinum group metals (PGMs = Pt, Pd, Ru, Ir, Rh and Os [110]) catalysts employed so far for the HOR in acidic media [43,111–117], anionic exchange membrane fuel cells (AEMFCs) are also very interesting because their applicability of non-Pt metal catalysts in alkaline medium, where most of the transition non-precious metals presents high stability [118,119]. While research on oxygen ORR catalysts in alkaline medium has been ongoing for many years [120], studies on hydrogen HOR catalysts for AEMFCs constitute practically a new field of investigation. In contrast to the fast kinetics of the HOR on PGMs catalysts in acidic media, it was found the HOR activity of several PGMs in alkaline electrolyte is around two orders of magnitude slower than the activity of these materials in acid electrolyte, all this as a result of an intrinsic HOR kinetic barrier [121,122].

Contrary, to the simple Volmer reaction performed in acidic media, Equation (8), in alkaline medium, Equation (10) is required to complete the HOR that comprise two different sub-processes of hydrogen adsorption on the metallic surface and water formation in alkaline medium [123].

$$H_2 + OH^- \rightleftharpoons H_{ad} + H_2O + 1e^- \qquad \text{Heyrovsky} \tag{9}$$

$$OH^- + H_{ad} \rightarrow H_2O + 1e^- \qquad \text{Volmer} \tag{10}$$

Recent attempts to reduce the amount of Pt in the design and production of electrocatalysts for the HOR were carried out by Gu et al. [124]. Using a hydrothermal method, the synthesis of Pt@Ru in the face-centered cubic (*fcc*) phase with a metastable phase for Ru under ambient conditions was performed. The *fcc* Pt@Ru nano crystals were produced by a one-step hydrothermal procedure, in which K_2PtCl_4 and $RuCl_3$ were reduced by formaldehyde (HCHO) at 160 °C in the presence of sodium oxalate ($Na_2C_2O_4$), HCl, and poly(vinyl-pyrrolidone) (PVP). The samples were referred to as $Pt_x@Ru_{100-x}$, in which x was the molar percentage of Pt in the feedstock.

As revealed by density functional theory (DFT) calculations, a preferentially epitaxial growth of Ru atom layers on the non-closest-packed facets of hetero *fcc* metal seeds led to the formation of *fcc* Ru shells to form Pt@Ru tetrahedrons/C, Figure 17; these morphological arrangements showed enhanced electrocatalytic activity with an order of magnitude more efficient toward the hydrogen oxidation reaction (HOR) in acidic electrolyte as compared with hydrothermally synthesized Ru/C [124]. The sample composed by tetrahedrons shows an average size of 8.3 nm, Figure 17b,c, which are in agreement with the models of *fcc* tetrahedrons from each zone axes, explicitly indicating that these particles are *fcc* tetrahedral single crystals enclosed by (111) facets. High angular annular dark field-scanning transmission electron microscopy image and their corresponding contrast line profile are shown in Figure 17d,e.

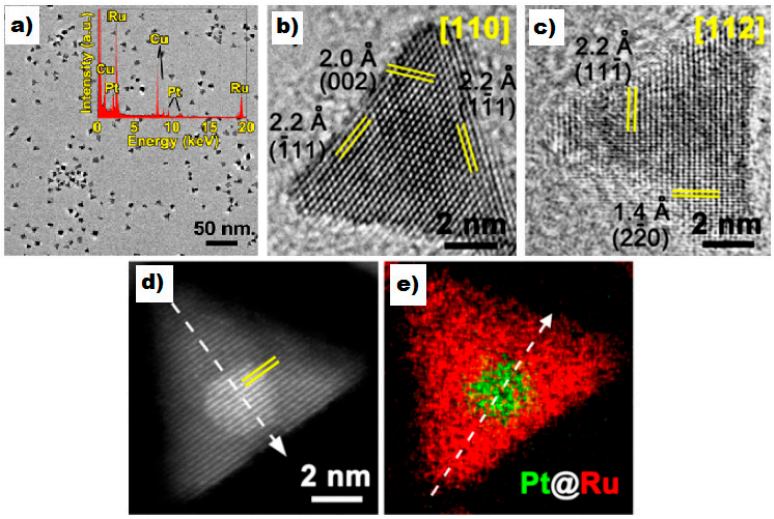

Figure 17. (**a**) $Pt_{10}@Ru_{90}$ nanotetrahedrons TEM image and its EDS (Energy dispersive spectroscopy) spectrum; (**b**,**c**) HRTEM (High resolution transmission electron microscopy) images, corresponding to FFT (Fast Fourier Transform) patterns, and models of *fcc* tetrahedrons from (110) and (112) zone axes, respectively; (**d**) HAADF-STEM (high-angle annular dark-field imaging-scanning transmission electron microscope) image; and (**e**) EDS mapping [124]. Reprinted with permission from [124]. Copyright American Chemical Society, 2015.

The HOR polarization curves obtained on *fcc* Pt@Ru, Ru/C (as-prepared), and commercial Pt/C loaded on glassy carbon RDE with a rotation speed of 2500 rpm in H_2 saturated 0.1 M $HClO_4$ solution are presented in Figure 18. A significant HOR activity was achieved on *fcc* Pt@Ru as compared to Ru/C. $Pt_{10}@Ru_{90}$/C showed the highest activity among the core-shell samples, i.e., 0.19 A·mg^{-1} and 0.30 mA·cm^{-2}. The mass, and area activities are higher, by one order of magnitude, than the as-prepared Ru/C (0.016 A·mg^{-1} and 0.017 mA·cm^{-2}) and comparable with those of commercial platinum (0.23 A·mg^{-1} and 0.27 mA·cm^{-2}).

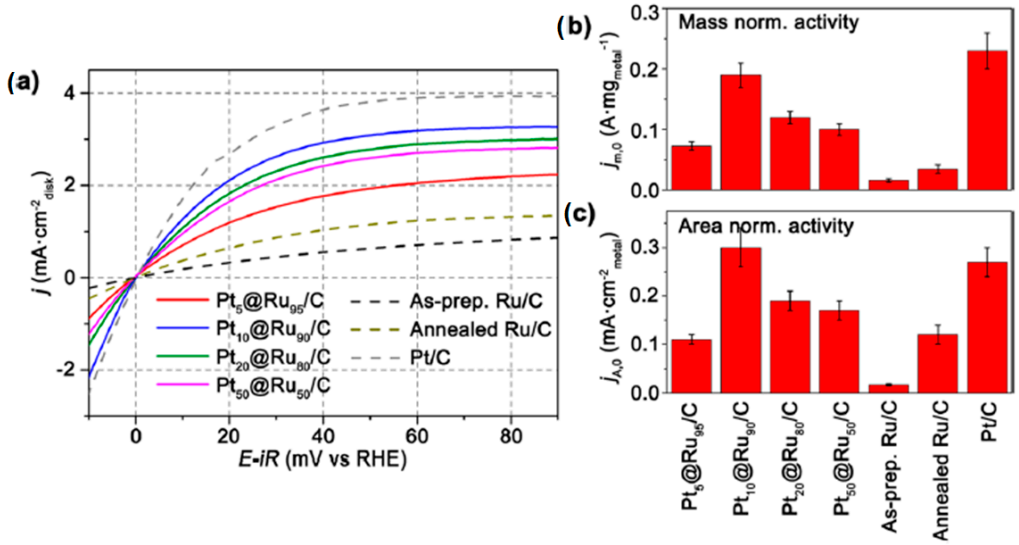

Figure 18. (**a**) Hydrogen oxidation reaction (HOR) Current-potential characteristics for Pt@Ru/C, Ru/C (as-prepared), Ru/C (annealed), and Pt/C (commercial); total metal mass: 3 µg. Test conditions: $\upsilon = 5$ mV·s^{-1}; at a rotation speed of 2500 rpm in a 0.1 M $HClO_4$ solution at 25 °C. (**b**) Mass and (**c**) ECSA (electrochemical surface area) normalized exchange current densities [124]. Reprinted with permission from [124]. Copyright American Chemical Society, 2015.

In search of new materials for HOR, palladium phosphide electrocatalyst with a small particle size was synthesized. Its improved stability, in acid medium, and the increased electrocatalytic activity towards the HOR with respect to commercial Pd/C was obtained [125]. Transition metals alloyed with phosphorus produced metal-phosphide, resistant to corrosion of the underlying transition metal, presenting metallic conductivity, or low electrical resistivity as low-band gap semiconductors [126]. Furthermore, they can be synthesized following a variety of routes and presenting high stability in basic and acidic media in comparison to the unalloyed metals [127–129]. The catalytic activity of transition metal phosphides and metal-phosphide materials namely, Ni [130–133], Co [134], Mo [135] and W [136] towards the HER has been studied. From these experiments it has been determined that the HOR performance of Pd-phosphide is comparable to that of palladium supported on carbon (Figure 19). The materials show a similar curve for the HOR, although there is a reduction in the limiting current value for PdP_2/C. Materials containing phosphide showed a weak wave before the limiting current which it is associated with the hydrogen oxidation on the phosphide lattice. This indicates that H_2 diffusion could be higher in the particles than in the palladium precursor. However, a faster onset for the HOR than the Pd/C precursor was visualized on the phosphorus material by dividing the current density by the corresponding limiting current.

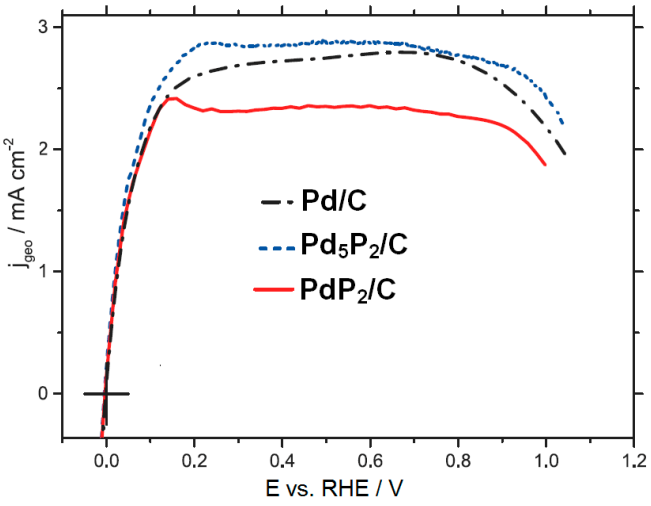

Figure 19. HOR on Pd/C, Pd_5P_2/C and PdP_2/C electrocatalysts in 0.1 M $HClO_4$ at 298 K [125].

Regarding the HOR in alkaline conditions, a pioneering study investigating non-PGM catalysts for HOR in AEMFCs, was carried out by Lu et al. [137]. In this work, Ni nanoparticles were decorated with Cr. This system generated an initial maximum power density of ca. 70 mW·cm^{-2}, operating at 60 °C. Another recent report has described nickel-based anode catalysts in alkaline media to oxidize hydrazine [138].

In a recent contribution Ni was combined with Mo and Co in ternary alloys: NiMoCo, which were tested for HOR in alkaline conditions [119]. This latter showed an improved HOR activity versus Ni alone; however, the recorded high HOR activity could be sustained only for anodic potentials below of 0.1 V, apparently because of the excessive surface oxidation above this potential. The HOR on both CoNiMo and Pt increases with applied overpotential below ~0.1 V, Figure 20. While the HOR increases beyond 0.1 V on Pt, on CoNiMo this reaction decreases certainly due to the passivation of Ni on the catalyst surface as suggested [119,139].

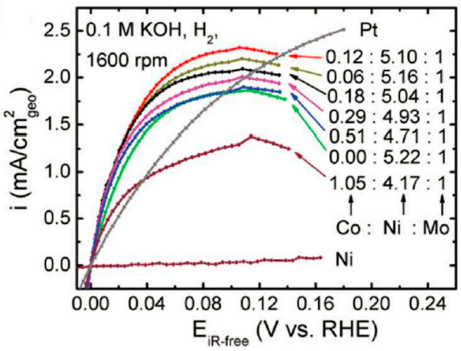

Figure 20. Linear scan voltammograms for the HOR on electroplated Ni, NiMo, CoNiMo. Atomic ratios between Co, Ni and Mo in the plating solution. Reprinted with permission from [119]. Copyright Royal Society of Chemistry, 2014.

Recent papers have proposed the use of various nanoscale electrocatalysts, such as Ni films partially covered by a palladium layer which provide one of the most active materials for the HOR [140]. These Pd/Ni electrodes were synthesized by an electrolytic deposition of palladium over a polycrystalline Ni surface varying the composition of the surface. The catalytic performance of the Pd/Ni electrodes towards the HOR was evaluated in alkaline medium, showing an improvement for this bimetallic catalyst. Limiting currents at 0.55 V in a H_2 saturated KOH solution, as well as the current exchange values are shown in Figure 21. Ni material did not present any catalytic activity in these conditions; this could be the result of a Ni surface covered with oxygenated species which block the surface and avoid the hydrogen adsorption. Nevertheless, a minimal palladium amount (0.5%) deposited onto Ni, activates the compound to perform the HOR. An increase of the coverage up to 17% in palladium shows two interesting phenomena; the kinetic current experiences a pseudo-linear increase from 1.5% to 17% palladium coverage. Contrary to the kinetic current increase, the onset potential presents a decrease as a function of the palladium loading. Both parameters did not present further improvement with a Pd deposition above 17%, Figure 21.

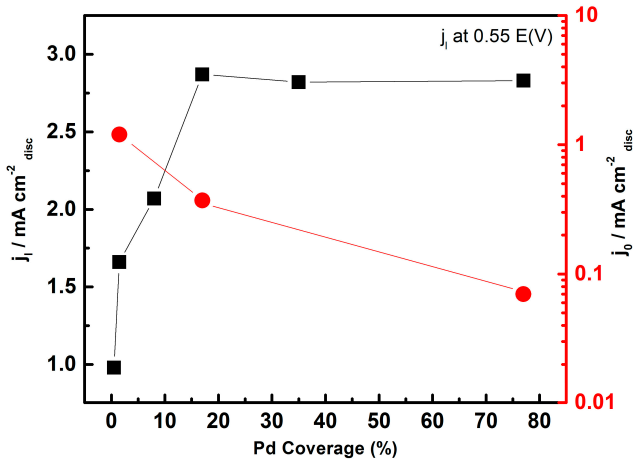

Figure 21. Limiting currents of Pd/Ni at 0.55 V as a function of Pd coverage percentage (Black squares) in H_2 saturated 0.1 M KOH, and comparison with the exchange current density from the Tafel plot (red dots). Data extracted from [140].

From this study the authors determined that the 17% Pd coverage corresponds to 7 atomic layers (approximately a thickness of 1.5 nm). It was also determined that Pd/C catalysts, under the same work conditions conveyed values below 0.1 mA/cm^2_{Pd} at an overvoltage η = 0.05 V with a palladium loading of 5 $\mu g/cm^2$ [141], while Pd/Ni with 0.9 $\mu g/cm^2$ reaches 0.30 mA/cm^2_{disc} and 0.57 mA/cm^2_{Pd}

at an overvoltage η = 0.05 V [120]. For Ni covered by a high amount of Pd, the exchange current density value reached a very similar one to that of Pd/C. This value < 0.1 mA/cm^2_{Pd} is the usual value for palladium in alkaline medium, this was corroborated in a similar study where a gold surface was covered by palladium [142]. Coming back to the Pd/Ni study, the highest exchange current values were obtained with a low Pd coverage, even above 1.5% on Ni (Figure 21 (red dots)) [140].

To replace a portion of the expensive platinum metal without compromising the HOR electroactivity in alkaline medium, the synergistic ligand and strain effects were put into advantage by alloying Pt NWs (nanowires) to metals such as: Fe, Co, Ru, Cu, Au [143,144]. The synthesis of such materials was done by a solution-based technique [145]. Pt NWs were synthesized using a hexachloroplatinic acid hydrate solution combined with cetyltrimethylammonium bromide (CTAB) in chloroform. Subsequently, water was added to this mixture to be stirred for an additional 30 min at 1600 rpm. After 30 min reaction, a sodium borohydride solution was poured in, as the reducing agent, and the reduction process was confirmed by a color change from gray to black. The entire mixture was stirred for an additional 20 min at 1600 rpm, subsequently centrifuged and the supernatant was discarded. The binary NWs were analogously synthesized using commercial precursor. To generate a series of PtRu, PtFe, PtCu, PtCo, and PtAu ultrathin nanowires, ruthenium (III) chloride hydrate, iron(III) nitrate nonahydrate, cupric chloride, cobalt chloride and hydrogen tetrachloroaurate (III) hydrate were used, respectively. A cleaning protocol was used to electrochemically eliminate the CTAB surfactant and activate the electrode surfaces [146]. Figure 22a shows the performance of as-synthesized Pt NWs with that of binary alloy catalysts made of 70 atom % Pt and 30 atom % Fe, Co, and Ru, respectively. Pt_7Ru_3 NW catalyst was able to achieve a diffusion-limited current at lower potentials, indicative of an improved HOR kinetics. Pt alloyed with both Au and Cu (30 at. %) are depicted in Figure 22b. Specifically, the Pt_7Cu_3 NW catalyst attain the diffusion-limited current density at ~0.2 V, whereas the Pt_7Au_3 NW catalyst only attained this value at ~0.25 V. This observation would indicate relatively slower HOR kinetics for this particular Pt_7Au_3 composition, with respect to other binary catalysts. The experimental HOR exchange current densities obtained at 2500 rpm with respect to the calculated hydrogen binding energy (HBE) values are found in Figure 22c [147]. Summing up, the exchange current densities have been used to evaluate catalytic activity, close to the reversible potential, since this is the potential where HOR is kinetically limited [148].

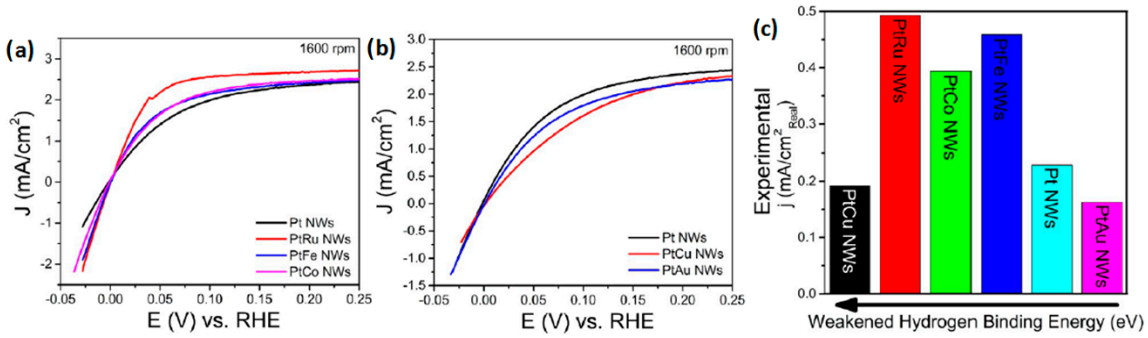

Figure 22. (**a**, **b**) HOR linear sweep voltammograms acquired in a hydrogen-saturated 0.1 M KOH solution at 1600 rpm (current normalized to the geometric surface area of the electrode). (**c**) HOR exchange current densities on the basis of calculated surface hydrogen binding energy (HBE) values [144]. Reprinted with permission from [144]. Copyright American Chemical Society, 2016.

There is no kinetic data in alkaline medium for rhodium electrodes. In this context, a study with nanostructured Rh electrodes with application in the HOR was carried out through the evaluation of the elementary kinetic parameters of the Tafel-Heyrovsky-Volmer (THV) mechanism [149]. By means of the sputtering of Rh on a glassy carbon substrate an electrode was prepared, this process was carried out in an inert atmosphere [150]. The analysis of the limiting current at an overpotential of η = 0.3 V as

a function of the rotation rate, under the kinetic mechanism of THV, is shown in a Koutecky-Levich plot, Figure 23. At this overpotential, one can read a kinetic current density of 3.44 mA/cm^2.

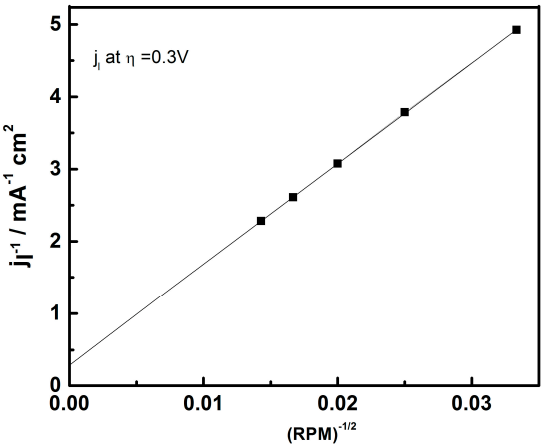

Figure 23. Koutecky-Levich analysis of the limiting current dependence with the rotation rate under the kinetic mechanism of Tafel-Heyrovsky-Volmer (THV) in 0.1 M NaOH, 298 K. Data extracted at η = 0.3 V from [149].

To establish the THV-mechanism, Equations (3), (6) and (7), certain constrains that imply the Koutecky-Levich expression were considered [151]. We can observe how in the potential range of interest, the HOR followed preferentially the Tafel-Volmer route [149]. The equilibrium reaction rate value obtained from the correlated experimental results was $j_0 = 1.18 \times 10^{-4}$ A·cm^{-2}, this value was significantly lower than that obtained for Rh in acid medium (6.77×10^{-4} A·cm^{-2}) [150].

3.2. Oxygen Reduction Reaction—ORR, and Carbon Supports

In addition to the precious metals, required to improve the kinetics of the ORR, the oxygen reduction reaction is also affected by the ionic species contained in the acid or alkaline media, where the electrocatalysts are evaluated [152]. The kinetics, and the electroreduction mechanism for oxygen is carried out through an adsorption of the oxygen molecules on the catalysts surface. This process can be affected by blocking species composed by the anions of the electrolyte or oxygen containing molecules (OH-ads). The presence of these species affects the coordination and the adsorption energy of the molecular oxygen over the catalyst surface, thus influencing negatively the reaction ORR mechanism [153]. Previous studies demonstrated that this deficiency of the electrochemical exchange is due to the effect of the blocking species: OH^- and anions present in electrolyte solutions. Such chemical species induce even a higher blocking effect on Pt-based electrocatalysts [154].

Various studies [155,156] have demostrated that the decrease in the ORR activity in sulfuric acid solutions (H_2SO_4) is caused by a substantial adsorption of sulfate (SO_4^{2-}) or bisulfate (HSO_4^-) onto the Pt surface which cause an adsorption mixed potential between the anions $H_2SO_4^-/SO_4^{2-}$ and the molecular oxygen. Another kind of species which affect the oxygen adsorption onto the catalysts surface are the phosphate anions (PO_4^{3-}) present in the phosphoric acid solution (H_3PO_4). Thus, it was determined that prechloric acid ($HClO_4$) is an ideal electrolytic solution to perform the ORR in acid medium since the perchlorate anions (ClO_4^-) practically do not interfere in the oxygen adsorption process at the catalysts surface [157].

On the other hand, the ORR kinetics is carried out in a more efficient manner in alkaline medium than acid medium [158]. This allows the use of catalysts with a lower price than Pt, such as silver, palladium, copper, nickel, among others [159]. The main technical disadvantages presented by the ordinary alkaline fuel cells (AFC's) are the durability of the electrodes, in highly caustic medium, the adequate water supply, at the electrodes to avoid both the anodic flooding, and the properly

cathode drying, and the progressive electrolyte carbonatation, which is caused by the CO_2 present in the atmosphere or produced from the oxidation of the fuel used [160]. The carbonates formation has a particular importance since these species precipitate over the electrodes, damaging and blocking the microporous structure of the catalysts and therefore the catalytic active sites reducing progressively the fuel cell performance [1]. To avoid the aforementioned issues, it was developed AFC's with flowing electrolytes streams, compared with the AFC's systems with stationary flow, these novel fuel cells present a better performance and lifetime [160–162].

Regarding catalysts supports, for Pt and non-precious metal based catalytic centers, carbon materials and oxides are most commonly used and investigated materials. Low and high graphitic carbon are, e.g., carbon black (CB), single-walled or multi-walled carbon nanotube (CNT), graphene oxide (GO) [55,163–182] and carbon nitride (CN) [183–186] among others. The semi-conducting oxides, such as TiO_2, doped-TiO_2 and doped-SnO_2, have been reported as support for catalytic centers [187–193]. The conductivity of oxides can be improved by synthesizing oxide/carbon composites [194]. The supports of this kind of composite materials are widely used for Pt or other catalytic centers [194–198]. The utilization of supporting materials can affect the nanoparticle (NPs) morphology, dispersion, and create a support-metal interaction (SMSI) [199–202]. These facts can favor the catalytic process, and hence, the support has a great impact on the design of composites based catalysts, aiming at improving the kinetics and stability for the electrocatalytic processes in low temperature fuel cells.

$$TiO_2 + 2H_2 + 3Pt \rightarrow TiPt_3 + 2H_2O \quad (8)$$

The SMSI effect is directly related with the electrochemical activity of novel electrocatalysts. This interaction was firstly found in metal NPs supported by oxide [199,200]. Tauster et al. demonstrated the loss of H_2 and CO absorption capacity on TiO_2 supported group 8 metals (Ru, Rh, Pd, Os, Ir and Pt) [200]. This phenomenon revealed the formation of a chemical bond between the metal and TiO_2, cf. Equation (8) [200].

Later, similar effect was discovered in, such as La_2O_3 [203], and ZrO_2 [204] supported noble metals. In addition to oxides, noble metals supported onto carbon-based materials showed also SMSI, as revealed by the electron transfer at Pt-C interface [201]. For non-precious metals, it is well known that Co–N chemical bonds form from cobalt-oxides supported N-doped carbon materials [205–207]. The SMSI effect was also reported in Ni/Al_2O_3, [208], Ni/HZSM-5 (zeolite) [209] composites. Recently, Alonso-Vante et al. [195,197,198,210] reported SMSI in Pt and rare earth oxide interface, in these experimentations different from classical SMSI, the SMSI was identified as structural surface modification of Pt NPs. Therefore, from this point of view, the SMSI widely exist in metal-support composites, induced by the surface/structure modification of the catalytic surfaces. The catalytic performance can thus be improved via tailoring SMSI, via, the use of oxide, oxide-carbon composites, and highly graphitic carbon supports [163,198,211,212], as revealed through the use of various analytical tools of data collected from XRD (X-ray diffraction), XPS or/and electrochemical CO-stripping [163,198,211,212]. A way to probe the SMSI for Pt surface, and structure modification can be brought into light from XRD data, since the Pt diffraction peak broadening is affected by crystallite size, micro-strain and stacking fault [211], on the other hand, the Pt XPS spectra may reflect the charge transfer at the interface, induced by chemical bonding [163]. The SMSI on Pt NPs surface can be probed further via CO-stripping [213].

3.2.1. Low Graphitic Carbon

With respect to low graphitic carbon materials, commercially available carbon black from Vulcan or Ketjen is usually applied to support nanoparticles (NPs) [164,214–219]. They were reported as supports for Pt, alloyed Pt-M (M = 3d transition metals), Pd and alloyed Pd-M NPs. For instance, commercial Pt NPs supported onto carbon black, have been widely used as a benchmark for electrocatalytic process in half-cells or fuel cells [195,197,198,220,221]. Pt-M nanoalloys supported by carbon black were developed to investigate the dealloying effect of M atoms on Pt surface towards ORR

activity in acid medium [215,219]. Recently, supported by theoretical DFT (density functional theory) calculation, Chorkendorff's group reported experimental facts showing that the Pt-RE (RE = rare earth elements) alloys were the most active and stable Pt-based electrocatalysts for ORR [12,222–224]. Therefore, the synthesis of highly and homogeneously dispersed Pt-RE nanoalloys is an interesting phenomenon in the domain of energy conversion. However, the synthesis is extremely difficult via a soft chemical route, since the reduction potential of metallic REs ca. < −2.0 V/RHE [197,198]. This is the reason why a layer of RE oxides usually cover the surface of the obtained Pt NPs, even after heat-treatment at 300–900 °C [195,197,198,210,225,226]; surprisingly, the ORR activity on RE oxides modified Pt surface was improved with respect to pure Pt surface. Therefore, it is very interesting to study the effect of RE oxides on Pt surface towards ORR, using carbon black as supports. As shown in Figure 24a–d, for Pt-M_2O_3 (M = Y, Gd and Sm) supported onto carbon black, the particle size and morphology were almost the same for both Pt and Pt-M_2O_3 NPs, whereas the ORR, Figure 24e, activity was enhanced on Pt-M_2O_3 NPs. Among oxide modified samples, the oxygen reduction activity on Pt-Y_2O_3/C overcame that on Pt-Gd_2O_3/C and Pt-Sm_2O_3/C samples.

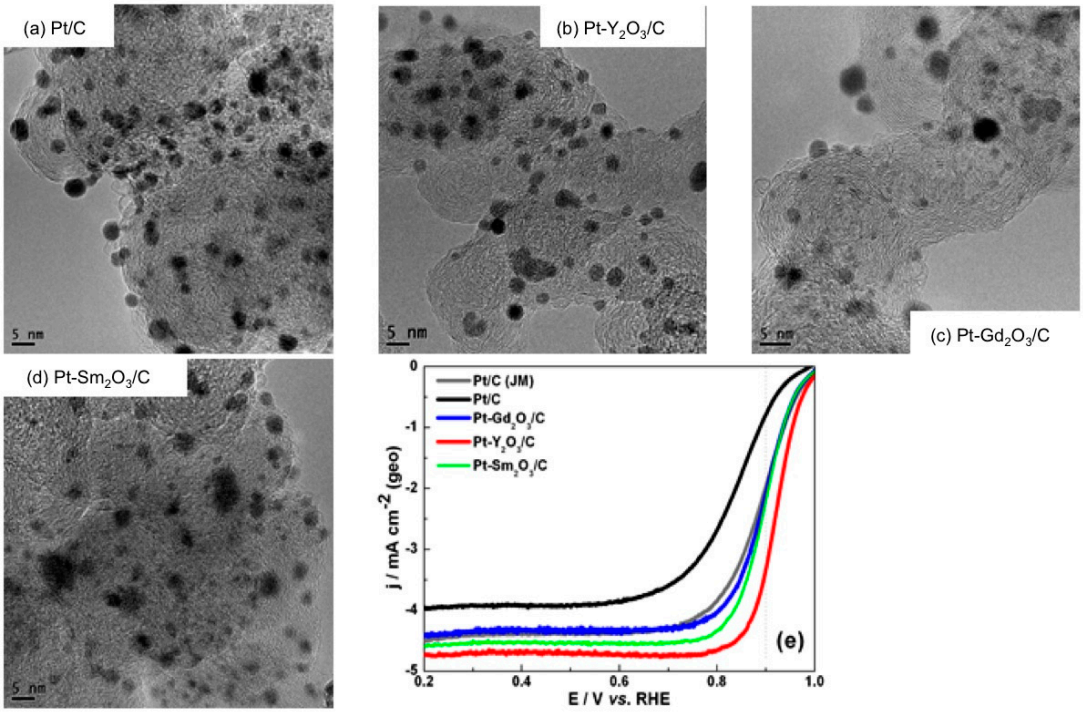

Figure 24. TEM images for (**a**) Pt/C and (**b–d**) Pt-M_2O_3/C (M = Y, Gd and Sm), respectively, and (**e**) the rotating disk electrode polarization curves (ORR) in oxygen saturated 0.1M $HClO_4$ at 900 rpm.

As indicated above, cf. Figure 6, different Pd NPs morphologies could be generated by adding different amounts of carbon support, showing the impact of carbon black support towards the nucleation of Pd NPs [57]. Moreover, the morphological impact of Pd NPs towards ORR and fuels (methanol, and formic acid) oxidation were identified [56,57]. In this regard, Co_3O_4 NPs, with different morphology deposited onto carbon black, showed different catalytic activity towards ORR [227]. The synthesis of Co_3O_4 NPs was done in two steps: (1) dissolving Co^{3+} precursor into a solution of water and DMF (dimethyformamide); and (2) adding ammonia into the solution to form $Co(OH)_3$ followed by a heat-treatment at 330 °C [227]. Adjusting the ratio of water and DFM to 1:0 (Co_3O_4-10), 3:1 (Co_3O_4-31), 1:1 (Co_3O_4-11) and 1:3 (Co_3O_4-13), a different morphology of Co_3O_4 NPs was, indeed, generated, Figure 25a–d [227]. This phenomenon indicates that nucleation of $Co(OH)_3$ onto carbon support was controlled by the ratio of aqueous and organic solvents during the synthesis [227]. The ORR Tafel plot, Figure 25e further shows the morphological impact of Co_3O_4 NPs towards catalytic activity [227].

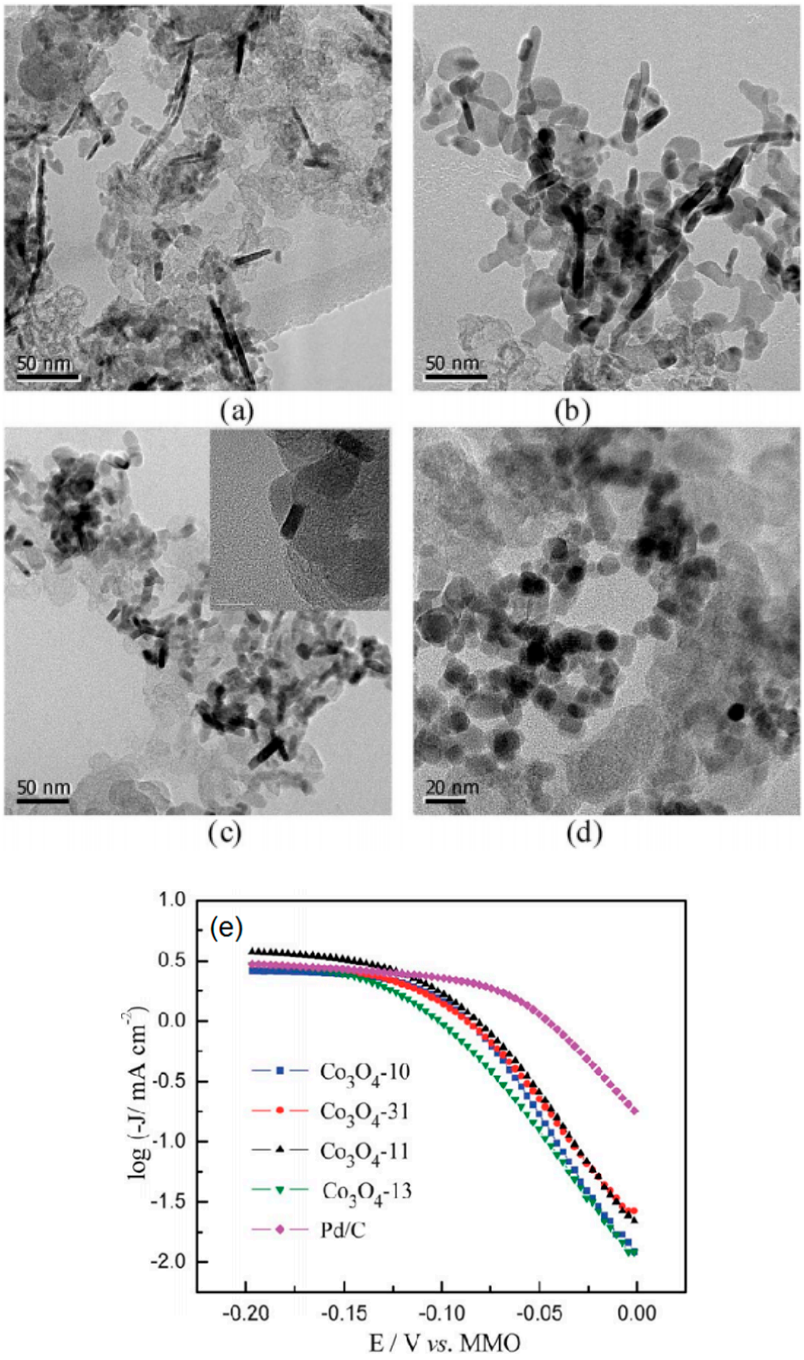

Figure 25. The TEM images for (**a**) Co_3O_4-10; (**b**) Co_3O_4-31; (**c**) Co_3O_4-11 and (**d**) Co_3O_4-13 supported by carbon black; (**e**) Tafel plot for ORR on Co_3O_4-10, Co_3O_4-31, Co_3O_4-11, Co_3O_4-13 and Pd/C (20 wt %). Reprinted with permission from [227]. Copyright the Royal Society of Chemistry, 2012.

Concerning the carbon nitride supports, Di Noto et al. [183] described the synthesis of a series of Pd-based catalysts with a general formula $K_n[Pd_xCo_yC_zN_lH_m]$ and a molar ratio $y/x > 1$ and $y/x < 1$. The most relevant results rely on the ORR activity presented by the Pd-based catalysts with $y/x > 1$ annealed at 700 °C and 900 °C which overpassed the activity presented by a commercial Pt/C electrocatalyst. With respect to HOR and methanol tolerance no-improvement against Pt/C was obtained. To explain this ORR catalytic improvement, the authors suggested that a high concentration of cobalt atoms provokes the Pd-rich domains coalescence improving the mass utilization efficiency of the active sites. Ongoing with the incorporation of active metals in a carbon nitride matrix, this group

synthesized two Pd-based electrocatalysts [184]. The materials PdNi-CN_h 900 and PdCoAu-CN_h 600 were produced by a pyrolysis method. The samples were physical-chemically characterized and evaluated towards the ORR with and without the presence of methanol and HOR. The main physical-chemical results revealed the formation of a disordered graphitic carbon nitride domain in PdNi-CN_h 900. On the other hand, PdCoAu-CN_h 600 presented a poorer nitrogen atoms incorporation due to a less graphitic carbon nitride matrix. No enhancement towards in the ORR and the HOR against the commercial Pt reference was observed. However, both electrocatalysts showed a better methanol tolerance than commercial Pt. Di Noto el al. [186] also worked in the production of Pt-based-carbon nitride (CN) core-shell electrocatalysts, and their application as cathodes in a single fuel cell system. PtNi-CN and PtFe-CN were synthesized via pyrolysis process and decorating a hybrid organic-inorganic material. In general, both PtNi-CN and PtFe-CN improved the fuel cell performance in comparison with the commercial Pt assembly. PtNi-CN presented a higher selectivity and a four-electron pathway to perform the ORR than the PtFe-CN. This enhanced activity was the result of a higher density of neighboring platinum active sites in the PtNi-CN surface [186].

Continuing in the same context, carbon nanohorns (CNH) is another interesting low graphitic carbon material, showing horn shape carbon particles self-assembling to a dahlia-like morphology [228–230]. Our group reported recently N-doped (NCNH) supported $CoSe_2$, Figure 26a, for ORR in alkaline medium [229]. The ORR activity on $CoSe_2$/NCNH was improved with respect to $CoSe_2$/CNH, $CoSe_2$/C and NCNH [229]. The XPS results revealed a charge transfer from N atom to $CoSe_2$ nanocrystals in the $CoSe_2$/NCNH sample [229], thus indicating a support catalyst center interaction in $CoSe_2$/NCNH, responsible for the ORR kinetics enhancement [229].

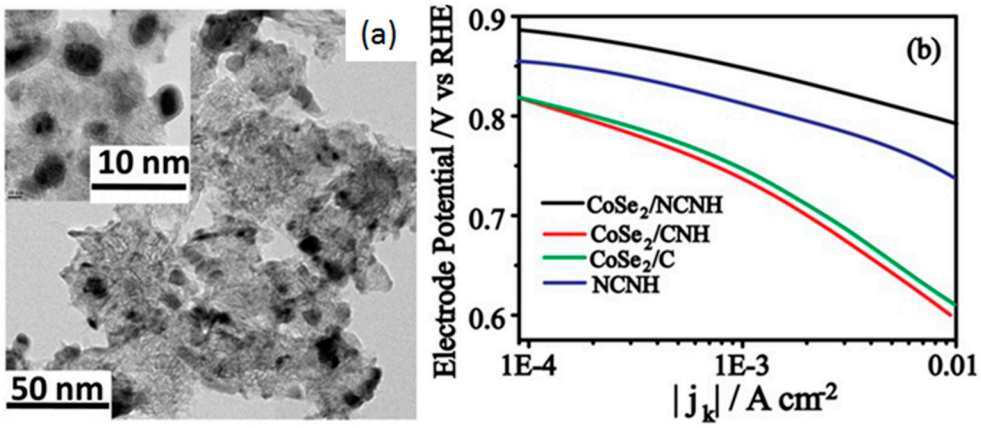

Figure 26. (**a**) TEM image for $CoSe_2$/NCNH sample; (**b**) Tafel plot for ORR on $CoSe_2$/NCNH, $CoSe_2$/CNH, $CoSe_2$/C and NCNH. Reprinted with permission from [229]. Copyright John Wiley & Sons, 2015.

3.2.2. High Graphitic Carbon

High graphitic carbon materials, such as carbon nanotubes (CNT) and graphene oxides (GO) are widely used as supports for both precious and non-precious catalytic centers [104,171,177,231–241] The high graphitic carbons are less corrosive than low graphitic carbon as shown in Figure 27a [164]. Taking CNT as an example, the Raman spectra show that the oxidized multi-walled CNT (ox.MWCNT) has dominant graphitic sp^2 domains, as compared to carbon (Vulcan XC-72) which shows highly disordered sp^3 domains, Figure 27b. The surface ratio $(I_D)/(I_G)$ domain was 2.1 and 1.2 for carbon Vulcan and ox.MWCNT, respectively.

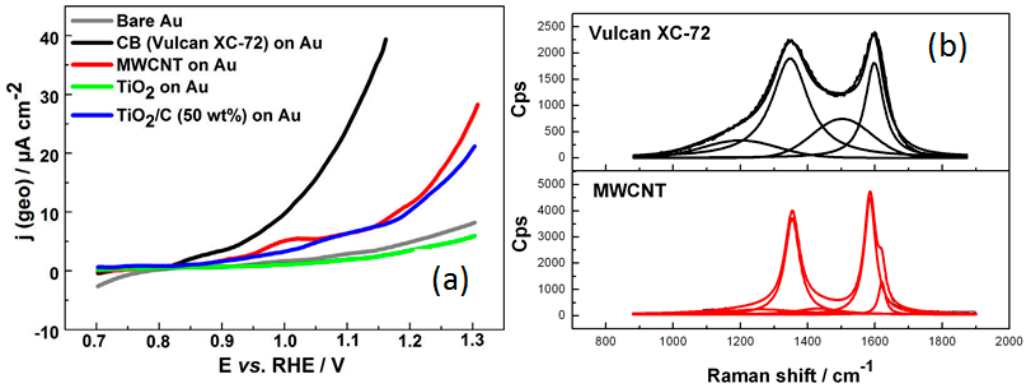

Figure 27. (**a**) The oxidation curves for carbon- and oxide-based supports in 0.1 M $HClO_4$. Reprinted with permission from [164], Copyright Elsevier, 2015. (**b**) The Raman spectra for carbon Vulcan XC-72 and oxidized multi-walled CNT (MWCNT).

When a catalytic center, e.g., Pt, is chemically deposited onto highly graphitic carbon the interaction takes place with both sp^3 and sp^2 domains, Figure 28a,b, shows the close Pt particle size and morphology [201]. However, the surface chemistry is totally different as depicted in Figure 28c. There is a sole CO-oxidation peak on the Pt/Vulcan sample, whereas there are two peaks on the Pt/MWCNT-m sample [201]. Based on Raman, XPS and DFT calculation results one can conclude that the peak I should be related to monoxide carbon oxidation on the platinum surface interacted with the sp^2 domain of the support, and peak II attributed to oxidation on Pt site interacted with the sp^3 domain [201]. The ORR stability, Figure 28d,e, in acid medium was improved on CNTs support with respect to carbon, and attributed to the interaction between Pt NPs and sp^2 domains of CNT.

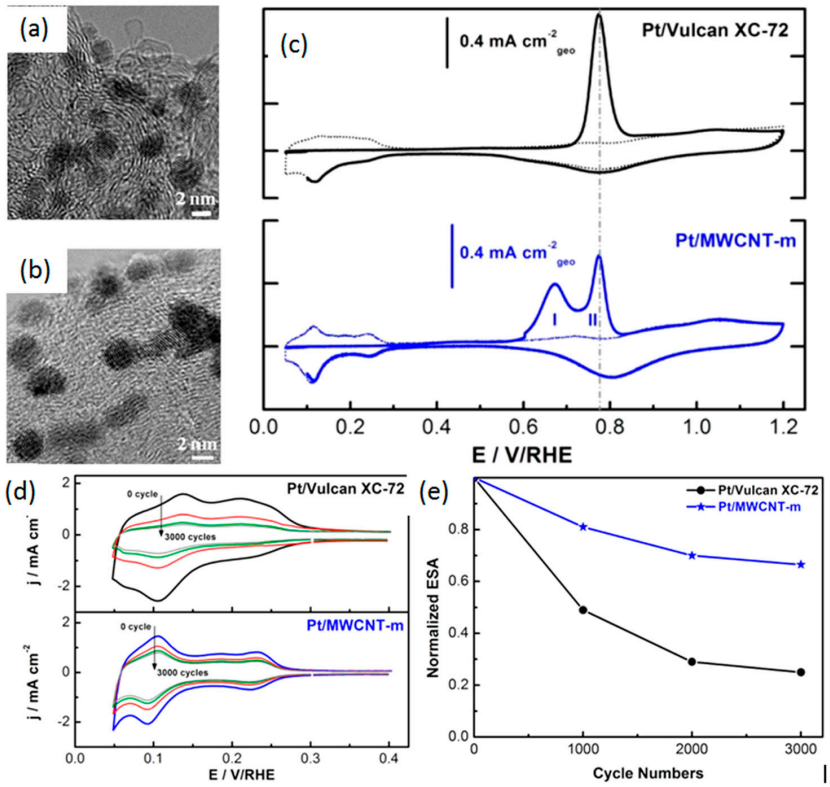

Figure 28. (**a**) Vulcan carbon XC-72 and (**b**) homemade MWCNTs (marked as MWCNT-m); (**c**) CO-stripping curves for Pt/C and Pt/MWCNT-m; (**d**) Cyclic voltammograms on Pt/Vulcan and Pt/MWCNT-m and (**e**) evolution of Pt active surface during cycling. Reprinted with permission from [201]. Copyright American Chemical Society, 2013.

Graphene, a highly graphitic carbon material, has been used for catalytic centers support. An increased ORR activity of Pt NPs deposited onto N-doped reduced graphene oxide (NRGO) was reported [242]. In this work, Pt NPs supported by GO, graphite, carbon black (Vulcan XC-72), reduced graphene oxide (RGO) and NRGO were synthesized and studied for ORR [242]. According to XPS results, Figure 29a,b, the electron transfer from Pt to N moieties was identified, and responsible for modifying the electronic state of Pt atoms, supported by DFT calculation [242], and the increased ORR activity, see Figure 29d. The finger print, onto the various supports, of Pt NPs are contrasted in Figure 29c.

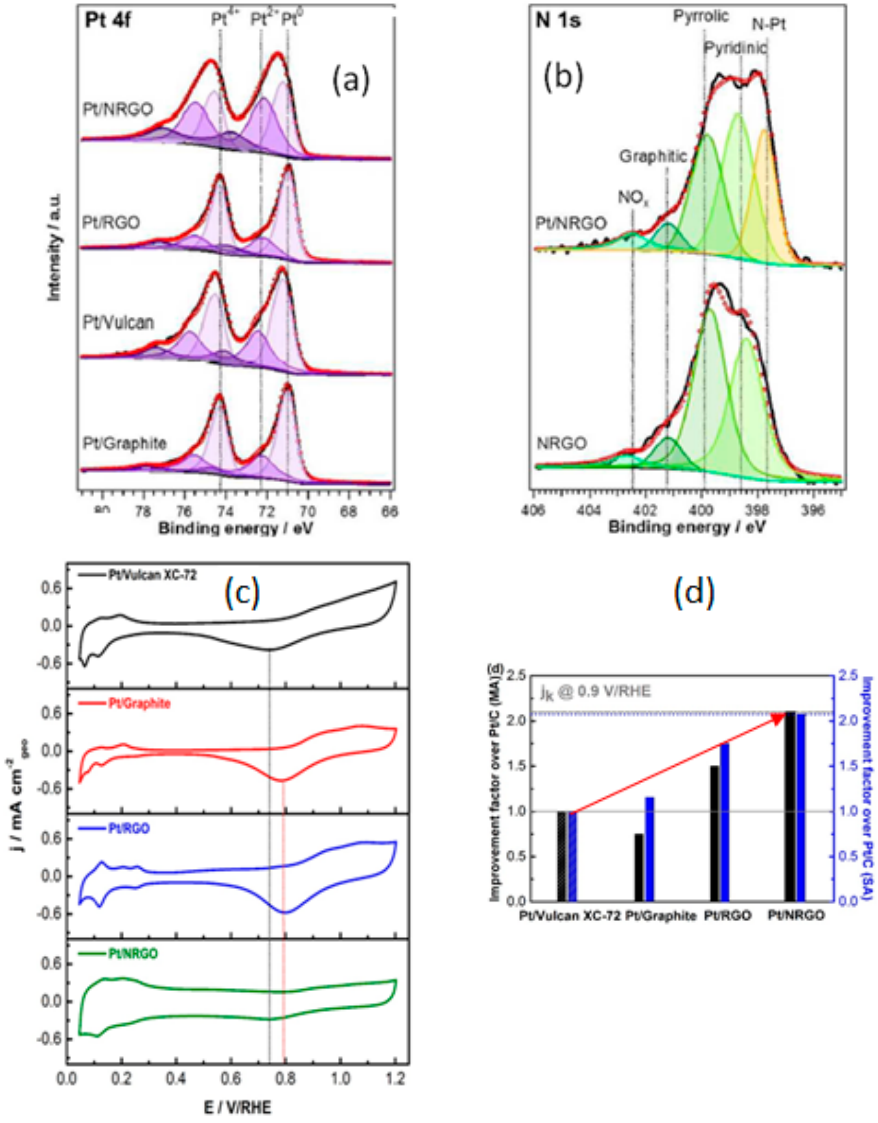

Figure 29. XPS spectra of (**a**) Pt 4f and (**b**) N 1s; (**c**) cyclic voltammograms and (**d**) normalized ORR specific and mass activity for Pt/Vulcan, Pt/graphite, Pt/RGO and Pt/NRGO. Reprinted with permission from [242]. Copyright the Royal Society of Chemistry, 2015.

The support also interacts with non-precious metal centers. This phenomenon is clearly shown for $CoSe_2$ in Figure 30a,b, where the ORR activity in alkaline medium was improved when the chalcogenide was supported on functionalized CNT (f-CNT) as compared to that on carbon black [243]. In acid medium, the f-CNT supported $CoSe_2$ was the most active catalyst for ORR, as compared to carbon black, TiO_2-C composite and NCNH supported $CoSe_2$ [243]. In alkaline medium, however, $CoSe_2$/NCNH showed the highest ORR activity, followed by $CoSe_2$/f-CNT [243]. One should note

that the NCNH support was very active towards ORR in alkaline medium [229]. Therefore, it is not surprising that the oxygen reduction activity was further increased on $CoSe_2$/NCNH.

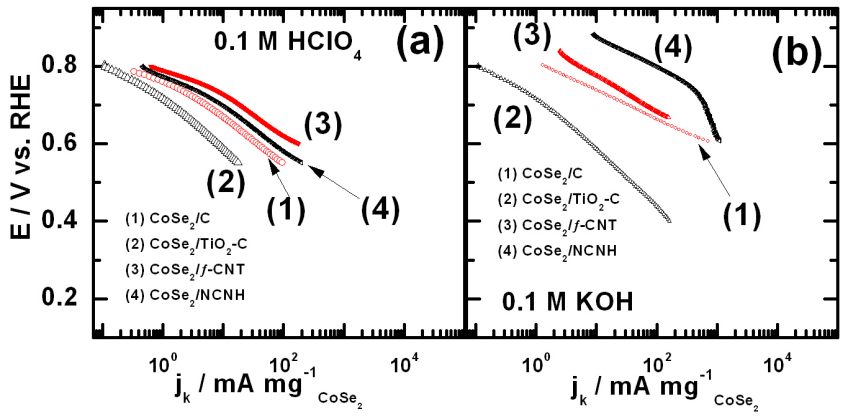

Figure 30. Tafel plot for ORR on $CoSe_2$/C, $CoSe_2$/TiO_2-C, $CoSe_2$/f-CNT and $CoSe_2$/NCNH in (**a**) acid and (**b**) alkaline medium.

An important contribution in the metal-support interaction domain was reported by Lee et al. [244]. They developed three novel Pd-Pt electrocatalysts supported onto three different carbon supports, namely, defective graphene nanosheets (GNSs), herringbone graphite nanofibers (GNFs), and single-walled carbon nanotubes (SWCNTs). The synthesis of the electrocatalyst Pd_3Pt_1 supported onto such different supports was carried out by chemical reduction of Pd and Pt precursor deposited on the various carbon supports. Among other characterization techniques, Raman spectrum was one of the most interesting tools to determine that GNS presented the highest disordered carbon structure with a D/G ratio of 1.23 over the values of 1.12 and 0.61 for Pd_3Pt/GNF and Pd_3Pt/SWCNT, respectively. Pd_3Pt/GNS presented the highest activity toward ORR in acid medium producing the highest percentage of water (70.35%). Because the use of the same active metal supported onto various carbon supports, the authors attribute the enhanced performance of Pd_3Pt/GNs to a metal-support interaction. Two years later this group reported the synthesis of a Pd-based electrocatalyst supported onto reduced graphene nanosheets (RGN) which were produced by an electrostatic method (RGNSECM) but also via a chemical reduction method (RGNCM) [245]. They deposited cubic Pd nanoparticles (10 nm) onto these two RGN substrates by an electrostatic deposition process. XPS analysis reveals one of the main characteristics to understand the metal-support interaction effect; the carbon contents in RGNSECM and RGNCM were 95.9% and 77.2%, respectively. Additionally, the oxygen content for these supports were 4.1% for RGNSECM and 22.8% for RGNCM. This analysis confirms the higher number of physical defects on RGNSECM resulting in more oxygen-containing functional groups which improve the supports vacancies to perform a better oxygen reduction. The electrochemical evaluations carried out in alkaline medium pointed out a higher mass activity for Pd cubes/RGNSECM but also a best catalytic response in the ORR overcoming the electrocatalytic response of RGNCM and a commercial Pd/C electrode. Furthermore, RGNSECM produced the less amount of hydrogen peroxide showing an oxygen reduction tendency of four-electrons but also a higher stability. These excellent properties of RGNSECM were related to the substrate defects, which induce a strong binding trap for Pd, a higher charge transfer, and a downshift in the d-band of the Pd clusters.

3.2.3. Oxide and Oxide-Carbon Composites

Oxides, such as semiconducting TiO_2 have been used as support materials for Pt-based catalytic centers, since much more corrosion-resistant than carbon materials, cf. Figure 27a. To favor the charge transfer between the oxide support and catalytic center, the conductivity of Titania must be improved

via doping. Recently, Mo- and Ru-doped TiO_2 ($Ti_{0.7}M_{0.3}O_2$, M = Mo and Ru) were reported as support for Pt NPs [193,246]. In both cases, the enhanced electron transfer between oxide and Pt was identified, leading to different Pt surface chemistry, catalytic activity and stability [193,246]. As depicted in Figure 31a, the X-ray absorption spectra show that the white-line intensity in X-ray Absorption Near Edge Structure (XANES) zone of $Pt/Ti_{0.7}M_{0.3}O_2$ was lower than Pt/C and PtCo/C [193]. In Figure 31b, the $Pt/Ti_{0.7}M_{0.3}O_2$ sample showed the lowest number of unfilled d-states, followed by PtCo/C, Pt/C and Pt foil, indicating that the electron transfer is carried out from the support to platinum, known as SMSI effect, induces the d-band vacancy of platinum. The effect is more significant on $Ti_{0.7}M_{0.3}O_2$ than on Pt. The ORR kinetics, in acid medium, shown in Figure 31c, is enhanced on oxide supported Pt with respect to Pt/C and PtCo/C. These results show that increased SMSI favors catalytic activity on Pt surface towards ORR.

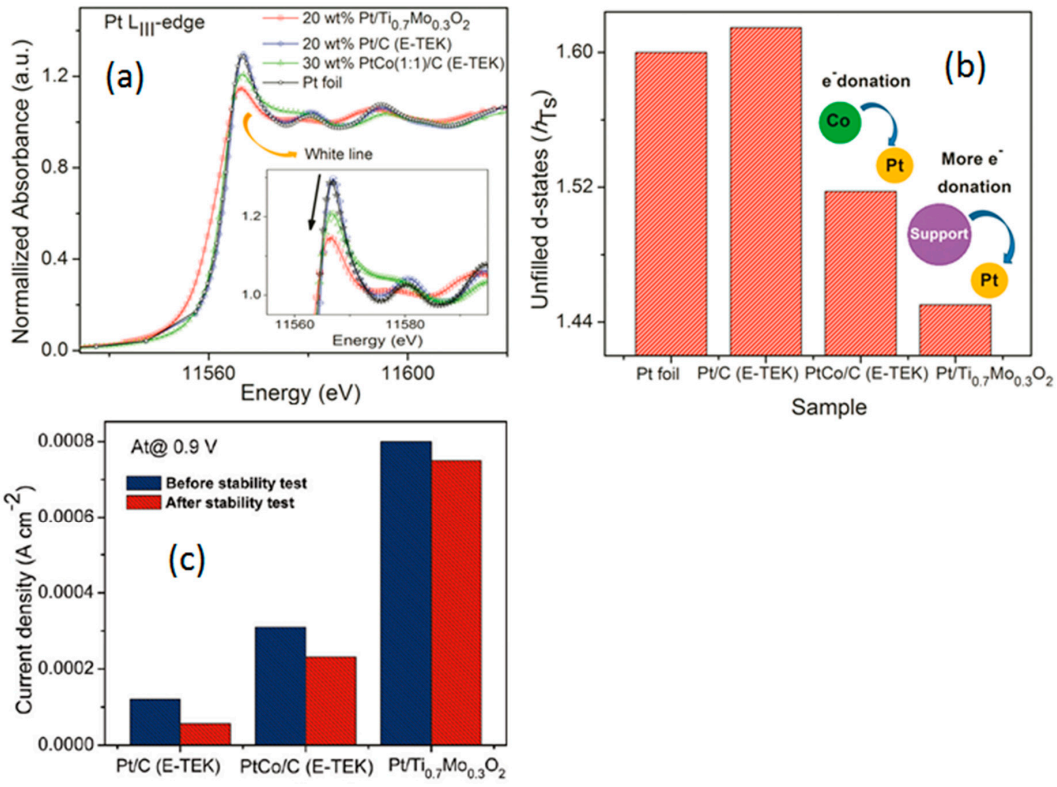

Figure 31. (**a**) X-ray Absorption Near Edge Structure (XANES) spectra of Pt L_{III}-edge; (**b**) values of unfilled d-state and (**c**) ORR kinetic current before/after stability test for Pt/C, PtCo/C and $Pt/Ti_{0.7}M_{0.3}O_2$. Reprinted with permission from [193]. Copyright American Chemical Society, 2011.

In addition, oxide-carbon composites are good candidates as catalytic center supports [194,196–198,210,247]. Our group reported Pt NPs supported by TiO_2-C, and Y doped TiO_2-C [194]. It was found that TiO_2 became more conducting after doping with Yttrium (Y:TiO_2-C). This material was as conducting as the carbon black, ensuring, in this way, the efficiency of electron transfer between the catalyst center and the support. The SMSI effect between Pt NPs and support was improved on photo-deposited Pt NPs onto oxides with respect to Pt/TiO_2-C prepared via a soft chemical route [194]. The SMSI effect can be easily visualized in the CO-stripping process, see Figure 32a, where one can observe that the photo-deposition (PD) favors the interaction between Pt and sp^2 domain of carbon support, whereas the carbonyl chemical route (CCR) favors the Pt-sp^3 interaction. Such an observation demonstrated a random dispersion of Pt NPs via CCR, while PD is more selective to deposit Pt NPs onto sp^2 domains of carbon. On TiO_2-C and Y:TiO_2-C, cf. Figure 32a, the Pt NPs interact with the sp^2 domain of carbon, and oxide. Concerning the ORR activity, in acid medium, there was a slight enhancement on Pt/Y:TiO_2-C, with respect to platinum samples without

Y, Figure 32b. The oxygen reduction stability on Pt/Y:TiO_2-C, studied via an accelerated stability test (AST), from 0.6 to 1.0 V/RHE, is close to that of Y-free samples. However, when cycling from 0.6 to 1.2 V/RHE, the stability of Pt NPs was clearly put in evidence on the oxide, Figure 32c–f. Such an observation indicated that the SMSI of Pt-Y:TiO_2 stabilized the Pt NPs on the support.

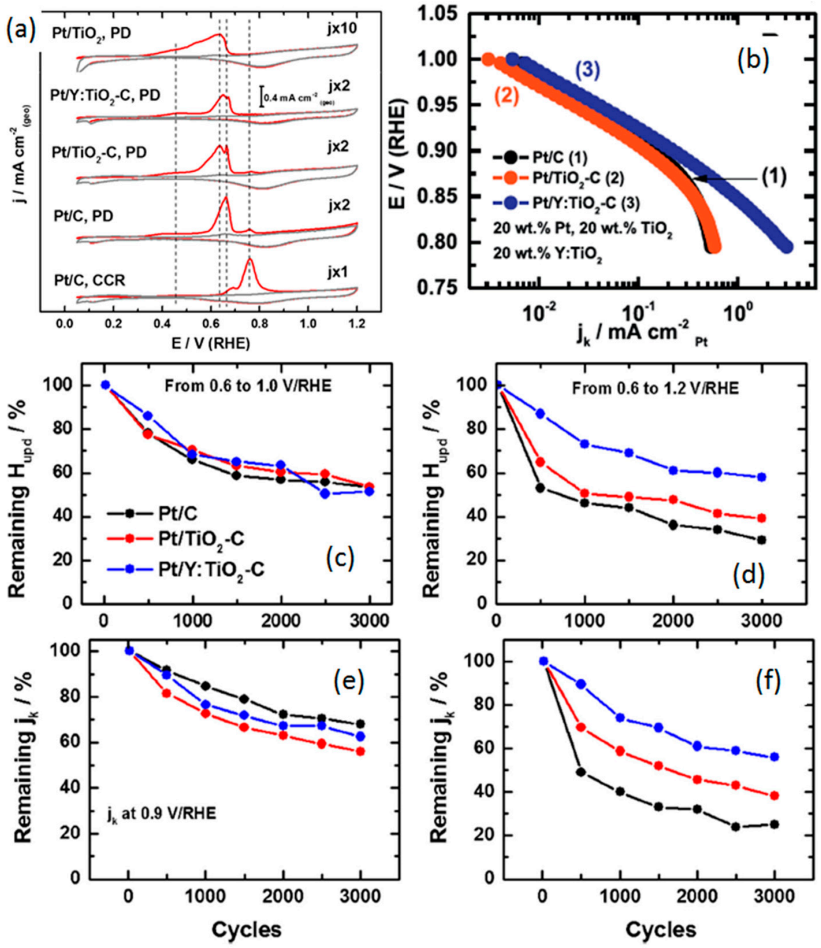

Figure 32. (**a**) CO-stripping for Pt/C (CCR), Pt/C (PD), Pt/TiO_2 (PD), Pt/TiO_2-C (PD) and Pt/Y:TiO_2-C (PD). (**b**) Tafel plot and (**c**–**f**) stability results towards ORR for photo-deposited Pt/C, Pt/TiO_2-C and Pt/Y:TiO_2-C. Reprinted with permission from [194]. Copyright Elsevier, 2015.

4. Micro-Fuel Cell Platform

Micro-Laminar Flow Fuel Cells

In the power generation field, as novel energy sources for residential and industrial applications, fuel cells have become essential devices. The fast advancement in the technology demands multi-functional, smaller and lighter electronic devices. This has stimulated manufacturers to look for alternative solutions [248]. Portable electronics, mobile phones, and computing gadgets are among the largest and fastest growing devices nowadays [249]. The statistics reveal that worldwide the number of mobile phone users increased from about 500 million in the year 2000 to about 5000 million in the year 2011 [250]. Recent data show a quasi-exponential growth of these values. The International Telecommunication Union's (ITU) latest report estimates that more than 7 billion mobile phone subscriptions were globally conducted by the end of 2014, with a population penetration rate of 97% [250]. Portable electronics currently rely on batteries as a power source, but the need for constant replacement and recharging, interrupted operation, disposal issues, and increasing power requirements has prompted the development of new power sources [251]. Thereby, micro fuel cells have become promising devices to satisfy the global power requirements [252] thanks to their easy operation,

competitive efficiency and environmental friendly performance. Even nowadays, the fabrication of such devices confronts many fabrication challenges, namely, design fabrication, the gas diffusion layer (GDL), electrocatalysts improvement and the exchange membrane assembly (MEA) [253]. The development of such devices is documented in the reference [254]. A recent modification of micro fuel cell systems are the silicon-glass-bonding systems by Mex et al. [255]. Silicon-glass-bonding systems retain the Nafion® membranes disadvantage, methanol crossover, therefore, extra barrier layers have to be employed. A new thin MEA consisted of sputtered catalysts deposited onto porous silicon supports, ceramics or foils. One of the main characteristic of those films is the low permeation rate and chemical and thermal stability.

On the other hand, researchers from the Mechanical Technology Incorporated (MTI) MicroFuel Cells institute carried out the development of a simple direct methanol fuel cell design that can be scaled to applications for a wide range of portable devices. This novel device design does not require the use of pumps and water collectors; these modifications reduce the manufacture cost but also allows the use of concentrated fuels [256]. On the same line, people from the Lawrence Livermore National Laboratory developed the prototype of a miniature fuel cell [257]. This device incorporated a thin-film and a microfluidic fuel processor into a common package. Methanol from replaceable cartridges was used as fuel, the power generation device provided three times longer operating time than rechargeable batteries. A design configuration in a planar array [258,259] a "flip-flop" arrangement which allows a fully continuous electrolyte [259] is shown in Figure 33. The series combination performance of the two configurations is shown in Figure 34.

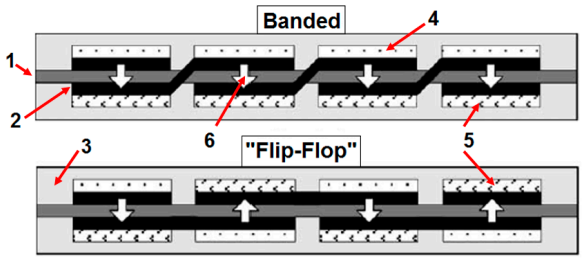

Figure 33. Banded and "Flip-flop" planar series interconnections. 1.—Membrane, 2.—Electrode, 3.—Flow Structure, 4.—Fuel, 5.—Oxidant, and 6.—Ion flux. The flip-flop configuration presents interconnects that avoid the membrane plane crossing, extracted from [258].

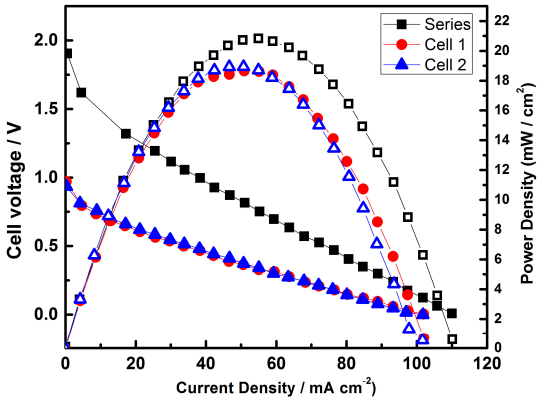

Figure 34. Cell voltage, and power density curves of two-cell assembly. Data extracted from [258].

The fabrication and evaluation of silicon wafers miniature fuel cells was reported by Yu et al. [260]. These devices consisted of a MEA between two silicon substrates. The design included feed holes and fuel distributors (channels in the silicon wafers). Pt/C electrocatalysts were used as electrodes (Pt loading = 4 mg/cm^2). To form the MEA, two electrodes with an area of 5 cm^2 were hot-pressed to a Nafion 112 piece. The results showed that the fuel cell performance was increased as a function of

the composite thickness (silicon wafer layers). The best performance was presented by the miniature fuel cell with smaller size channels, these results are presented in Figure 35 [260].

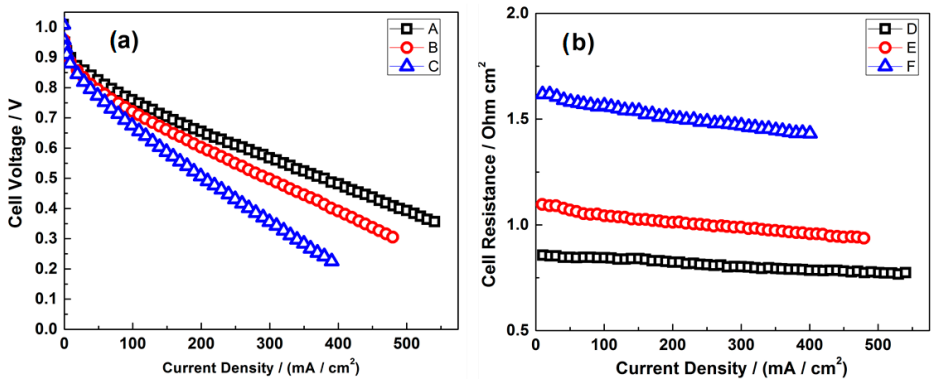

Figure 35. (**a**) Polarization of cells (A = cell 3, B = cell 2, C = cell 1); and (**b**) resistance of cells (D = cell 3, E = cell 2, F = cell 1). The cell temperature was 25 °C, dry H_2/O_2, the gas pressure was 0.10/0.10 MPa and the gas flow rate of H_2/O_2 at 50/50 mL/min. Data extracted from [260].

Until 2004, researchers were focused on tailoring, and miniaturizing, polymer exchange membrane fuel cells—PEM related issues [261]. It was not until 2005 that Choban et al. [262] worked on the first membraneless micro FC. This novel design eliminates the fuel crossover and cathode flooding issues presented in fuel cells. In this research, the membraneless micro FC performance was studied in acid, alkaline and also mixed-reactant media. In this last condition the cathode is in acid medium, while the anode is in alkaline medium or vice versa. In these flow conditions, the aqueous streams are merged into a microchannel and they continue flowing in a laminar flow through the channels configuration (Figure 36a).

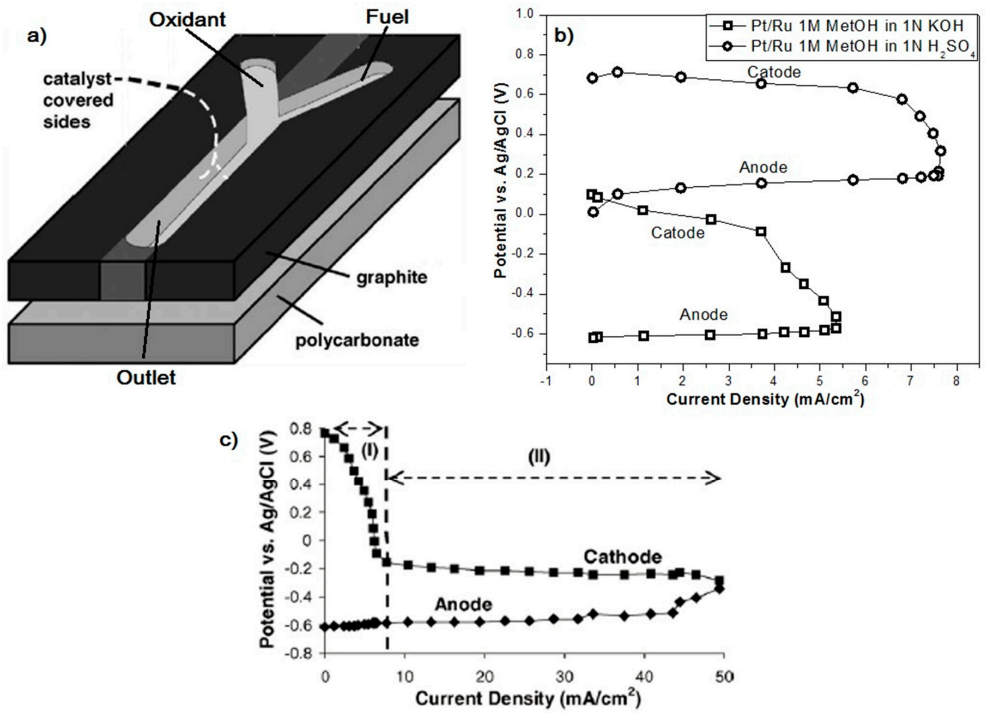

Figure 36. (**a**) Laminar flow fuel cell scheme. (**b**) Current-potential curves of individual electrode performances with an oxidant stream of oxygen-saturated. (**c**) Individual electrode performances (mixed-media configuration). Fuel: 1.0 M methanol in 1 N KOH; Oxidant: O_2-saturated 1 N H_2SO_4. Data extracted from [262].

In this experiment, unsupported Pt/Ru nanoparticles and Pt black were used as anode and cathode, respectively [262]. The individual electrodes polarization curves in different media are shown in Figure 36b, the results presented in this work are in agreement with the literature [263,264]. After several days, without operational interruption, any performance drop was appreciated. Also, any carbonate formation issue was found in this LFFC. In the mixed-reactant mode (anode-alkaline, cathode-acid), Figure 36c region II, we can observe how at constant cathodic potential the current potential value increased until the anodic value became the limiting factor.

The limiting behavior of mass-transfer is observed for the oxidation of methanol in these experimental conditions [265]. A higher overall cell potential, OCP and current density was obtained for the mixed-reactant configuration than those registered for all acidic and alkaline conditions.

The fuel cell operation in alkaline medium presents positive advantages in the kinetic of the anodic and cathodic reactions. However, the called "mixed-reactant" conditions allows the opportunity to increase the maximum OCP achievable in simple alkaline reactant conditions. Additionally, the design simplicity for this condition allows experiments to be carried out consecutively in a single fuel cell without modifying the system and changing only the pH of both electrolytic streams [262]. It is well known that the flow channel configuration [266] can induce the forced water removal inside the fuel cell [267]. According to this, Hsieh et al. [268] studied the flow fields configuration and effects under fixed operating conditions. Four flow fields were studied herein; the so-called interdigitated flow channel presented the most uniform transient current in comparison with the rest of channels designs: Parallel, mesh and serpentine. Finally, in this study it was developed a correlation of the water accumulated in the flow channels according to the time [268].

The development of a miniature PEM fuel cell stack with carbon bipolar plates was described in a previous contribution [269]. In Figure 37 is shown a representation of the PEM fuel cell stack. The stack is assembled in the following order: end plate, rubber gasket, bipolar end plate, rubber gasket, MEA, rubber gasket, bipolar plate, rubber gasket and end plate as depicted in the final fuel cell stack shown also in Figure 37. The way to keep together all those components is using screws which align the cell components and also allow the compression pressure control.

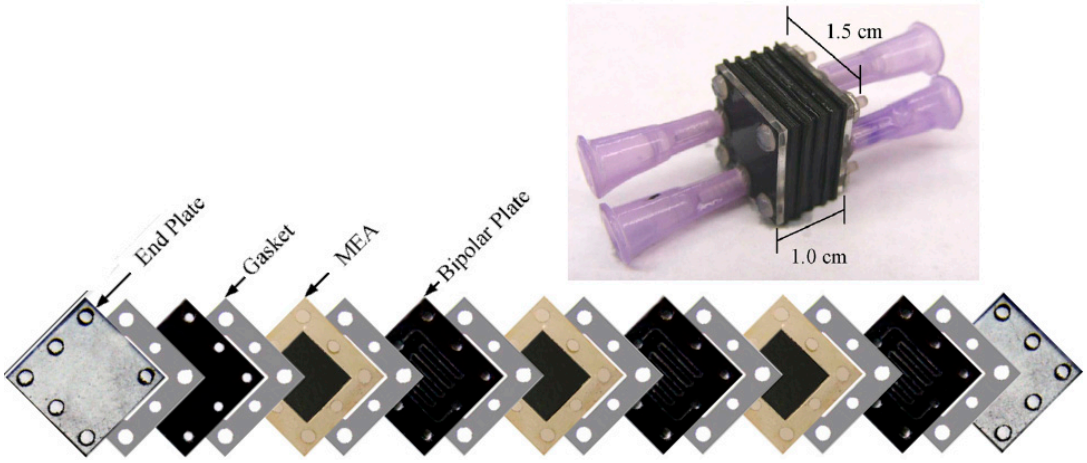

Figure 37. Three-cell fuel cell stack configuration. Scheme extracted from [270].

In this way, the stack was tested at different temperatures, Figure 38. The current-potential curves showed how the voltage increased as a function of the temperature increment. The optimal temperature conditions for this design was 60 to 80 °C and employing external hydration, because the dehydration of the membrane a cell drop performance occurred above 80 °C [270].

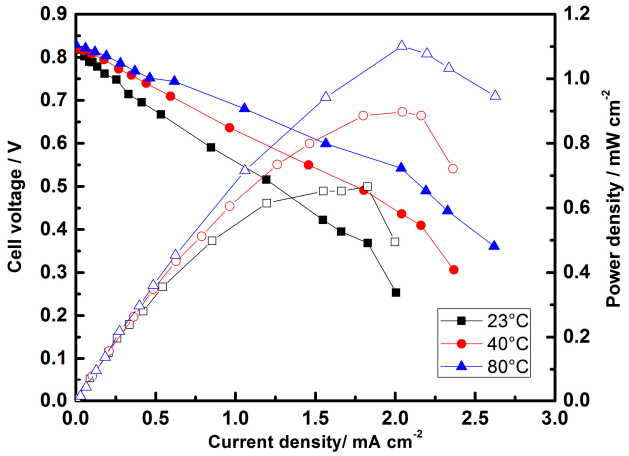

Figure 38. Temperature effect on the fuel cell polarization and the power density curves. Data extracted from [270].

Regarding the methanol crossover issue, and the methanol tolerant electrocatalysts development for the ORR, Whipple et al. [271], worked on the miniaturization of fuel cells tailoring the design and simplifying the fuel cell operation, Figure 39.

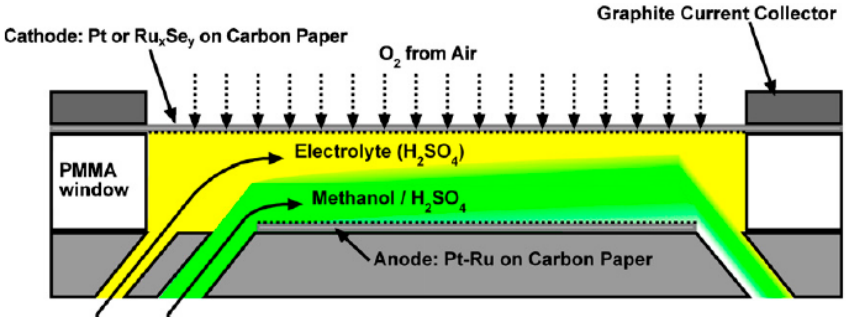

Figure 39. Scheme of the air-breathing laminar flow fuel cell (LFFC) [271]. Reprinted with permission from [271], Copyright Elsevier, 2009.

For this experiment two different cathodic streams without methanol and containing the same amount of methanol at anode were used in the operation of the laminar flow fuel cell. In the same way, an acid solution (0.5 M sulfuric acid) containing 0.1, 1, 2, 5, 7, 10, or 15 M CH_3OH was used as anolite. Figure 40 shows the individual cathodic and anodic polarization curve. These curves show the high depolarization of the Pt cathode in the presence of a stream containing methanol, Figure 40a2, this effect does not affect the same Pt electrode in the free-methanol stream, Figure 40a1. As we can observe, this depolarization effect does not occur when a Ru_xSe_y electrode is used as cathode; on the contrary, we can observe a slightly enhancement. This result proves that Ru_xSe_y electrocatalyst presents high tolerance to CH_3OH and does not present a depolarization effect caused by a mixed potential as occurs with Pt [82,272–274].

The Ru_xSe_y performance increase in presence of methanol can be explained as a result of a change in the oxygen diffusivity and solubility (Figure 40b2). Itoe et al. [275] showed that these two last parameters change in function of the CH_3OH–H_2SO_4 concentration ratio. This research group found that upon addition of CH_3OH to 0.5 M H_2SO_4, the initial oxygen diffusivity jumps by a factor of 2.5 to 3; after this, this value decreases until the initial value.

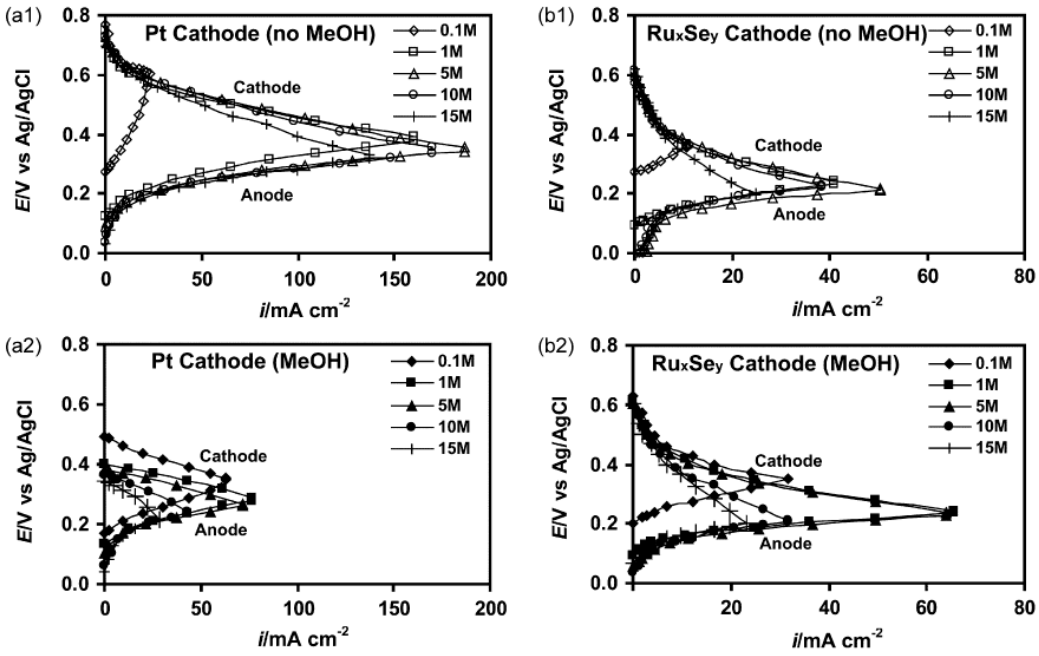

Figure 40. Current-potential curves of individual electrode performances for (**a**) Pt and (**b**) Ru_xSe_y cathodes working in a stream comprised of (1) 0.5 M H_2SO_4 and (2) 0.5 M H_2SO_4 + the methanol concentration present in the anode [271]. Reprinted with permission from [271], Copyright Elsevier, 2009.

This study demonstrated that the activity of the ruthenium chalcogenide (Ru_xSe_y) cathode increases in presence of CH_3OH concentration by 30 to 60% in the concentration range of 1 to 7 M [271].

The flow fields design of micro PEMFCs was reported by Lu et al. [253]. In this study, the authors evaluated the effect of different flow field topologies in the μ-PEMFCs performance, Figure 41. The electrochemical tests were performed at reactant flow rates of 15, 30 and 50 mL·min^{-1}. As a result of this experiment it was found that the μ-PEMFCs with different flow patterns present a similar tendency at flow rates of 50 mL·min^{-1}. On the contrary, the μ-PEMFC performance is rapidly deteriorated at low flow rates, this decrease of performance is caused by the micro channels flooding. The design with mixed and long multichannel yielded the best performance [253].

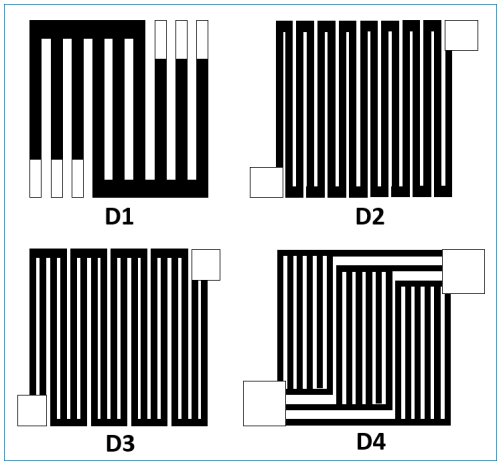

Figure 41. Flow design variations (D1–D4) for the μ-PEMFCs (micro proton exchange membrane fuel cell) reported in [253].

In Figure 42 we can observe the maximum power density value reached by each flow field (D1-D4) at a current density value of 175 mA·cm^{-2}. At a flow rate of 15 mL·min^{-1}, the power density value is in the range from 76 mW·cm^{-2} to 105 mW·cm^{-2} (38% discrepancy), 21% for the flow rate of 30 mL·min^{-1}, and finally 13% for the flow rates of 50 mL·min^{-1}.

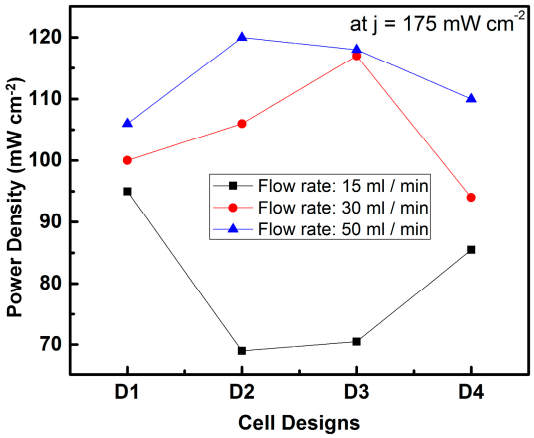

Figure 42. Power density curves of the different μ-PEMFCs designs with different flow rates at a density current value of 175 mW·cm^{-2}. Data extracted from [253].

Since we know that cluster-like compounds such as the ruthenium chalcogenide Ru_xSe_y presents a high methanol tolerance, and selectivity to perform the ORR in presence of methanol [82,271–274], Gago et al. reported on the electrochemical measurements of 20 wt % Ru_xSe_y/C as cathode for the oxygen reduction in the presence of formic acid in a microfluidic formic acid fuel cell (μFAFC) [276]. A commercial Pt/C electrode was used also for comparison purposes. It was found that at formic acid concentration of 0.5 M, Ru_xSe_y/C and Pt/C reached maximum current density values of 11.44 mA·cm^{-2} and 4.44 mA·cm^{-2}, respectively. Meanwhile the power density values were similar for both materials, ca. 1.9 mW·cm^{-2}. On the other hand, at a concentration of 5 M formic acid the power density value for Ru_xSe_y outperformed 9 times the power density value obtained by Pt/C, Figure 43, attesting that the Ru_xSe_y electrocatalyst is more suitable than Pt/C to be used as cathode in a μFAFC [276].

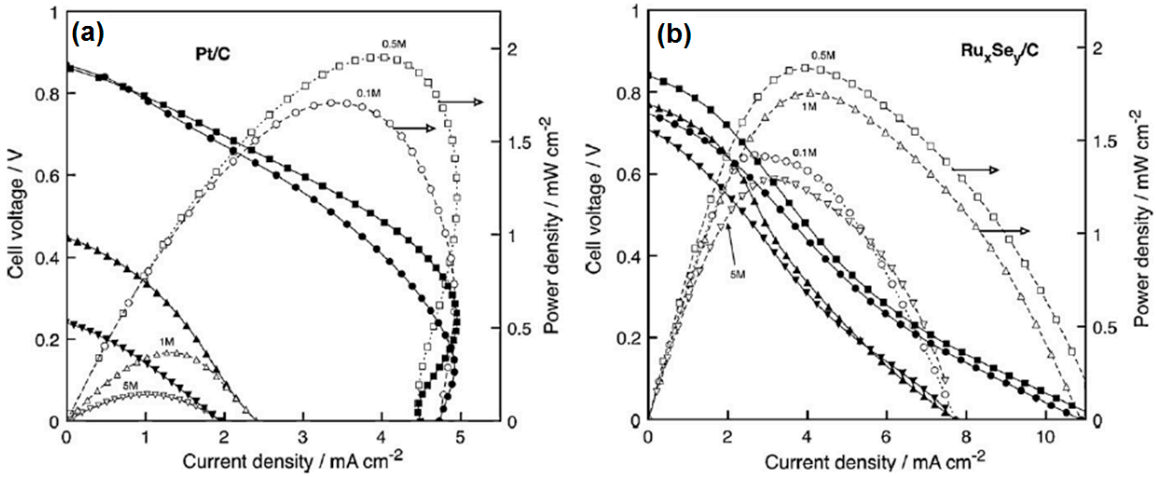

Figure 43. Polarization and power density curves for (**a**) 30 wt % Pt/C E-TEK and (**b**) Ru_xSe_y/C; in the μFAFC. 0.1 (circles), 0.5 (squares), 1 (triangles) and 5 M (inverted triangle), T = 25 °C, Flow rate = 1.2 mL·min^{-1}. 20 wt % Pd/C E-TEK was used as anode catalyst [276]. Reprinted with permission from [276]. Copyright Elsevier, 2011.

In 2012, Brushett et al. [160] performed a very interesting experiment on the alkaline microfluidic H_2/O_2 fuel cells field. They used a micro fuel cell to evaluate the electrochemical activity of Pt/C-based electrodes in alkaline medium. Their studies demonstrated that the behavior of such alkaline fuel cells (AFCs) is restricted by carbonated species presented in the electrolyte. These species affected only the performance of the anode, whereas the cathode performance remains practically unchanged. The carbonate formation (CO_3^{2-}/HCO_3^-) is one of the major technical issues in AFCs, this species formation reduces the concentration of OH^- in the electrolyte, hence it reduces the solution conductivity and the kinetic of the electrode reaction. One strategy to mitigate the water management and carbonate issues in alkaline FCs is with a recirculating electrolyte, the flow of the electrolyte helps the water management and removes carbonates resulting in a carbon dioxide tolerance up to ~100 ppm [160]. In this work, experiments to study the tolerance to CO_2 poisoning were performed as described as follows; in the first condition, CO_2 was injected in the anodic side of the μLFFC in stationary electrolyte conditions (3 M KOH). In order to determine a baseline, the first evaluation of the cell performance was carried out without the presence of CO_2. After this, a flow of 15 sccm of CO_2 was injected to the anode for 10 min meanwhile a nitrogen flow of 15 sccm was flowed in the cathode. After the gas exposure, the device was electrochemically evaluated to determine any change in performance. Afterwards, a second CO_2 exposure (10 min) followed by the electrochemical evaluation were performed. Subsequently, a rinse of the chamber was done by flowing KOH solution (10 min). Finally, the fuel cell was tested in a stationary mode in order to determine the KOH rinse effect. To perform a second study, the research group followed the same conditions of the first tests but introducing the CO_2 at the anode with a flowing of 3M KOH solution at a continuous flowing rate (0.3 mL/min) [277].

Figure 44a shows the electrochemical evaluation of the fuel cell operating with a stationary electrolyte. As a result of the CO_2 exposure the fuel cell suffers a power density decrease after the first exposure stage, and this power density reduction drops even further after the second CO_2 exposure. Nevertheless, the maximum power density value of 103 $mW \cdot cm^{-2}$ was regained after the KOH rinse, Figure 44a. The reduction of current density registered was attributed to precipitants which can be eliminated by the effective KOH rinse. On the other hand, in Figure 44b we can observe the polarization and power density curves for the flowing electrolyte conditions. From these curves we can observe how CO_2 does not affect the fuel cell performance because any carbonate species formed inside the fuel cell is immediately flushed. This study confirms that the fuel cell electrodes in flowing electrolyte conditions are not affected by the CO_2 exposure [277].

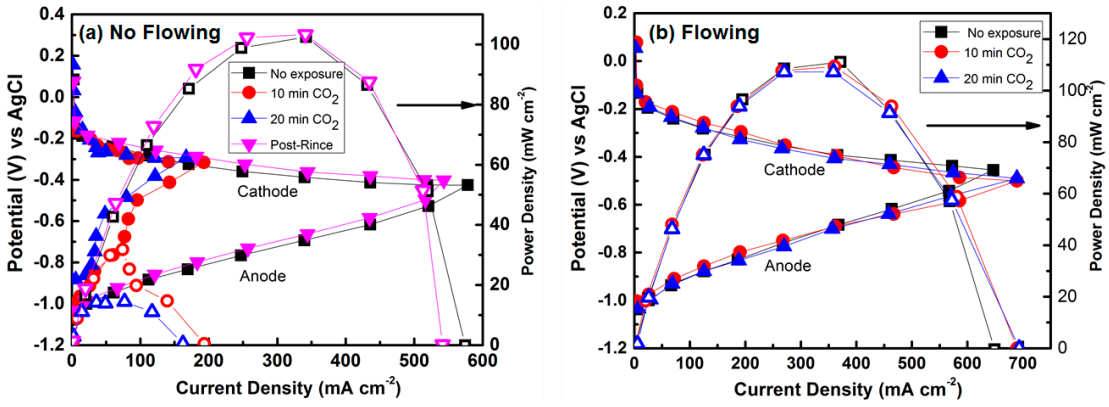

Figure 44. Anodic-cathodic polarization curves and power density curves for the alkaline microfluidic H_2/O_2 fuel cell exposed to CO_2 (**a**) stationary electrolyte, and (**b**) flowing a KOH solution. In both studies the H_2/O_2 flow rate was 50 sccm, the electrodes loading was 2 mg·Pt/C/cm^2, and experiments were performed at room temperature. Data extracted from [277].

Coming back to the transition metal chalcogenides and the membraneless fuel cells, two novel catalysts; carbon-supported Pt_xS_y and $CoSe_2$ were tested in a novel μLFFC [278]. A schematic image of the fabrication and assembly of the micro fuel cell components is shown in the Figure 45, detailed information about the components and operation can be consulted in reference [278].

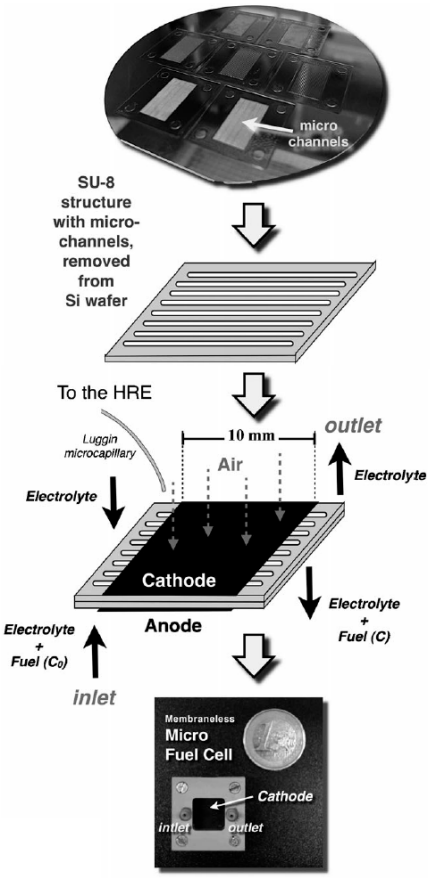

Figure 45. Fabrication and operating scheme of the μLFFC (micro-laminar flow fuel cell) [278]. Reprinted with permission from [278]. Copyright Elsevier, 2012.

In this study, the authors reported how such chalcogenide materials can be employed for developing cheaper, simpler, and smaller micro devices [278]. In Figure 46, we can observe how at a fuel concentration of 5 M CH_3OH the power density curves reached maximum values of 6.5 $mW{\cdot}cm^{-2}$ for Pt, 4 $mW{\cdot}cm^{-2}$ for Pt_xS_y and 0.23 $mW{\cdot}cm^{-2}$ for $CoSe_2$ when these material were used as cathodes in the micro fuel cell assembly. Moreover, when the micro fuel cell was operated in mixed-reactant mode, the maximum value for the Pt power density decreased by 80%; and 35% for Pt_xS_y; nevertheless, $CoSe_2$ did not present any change in performance [278].

These results suggested further that a μLFFC with selective electrodes can operate in mixed-reactant mode (one electrolyte + fuel stream). This configuration makes easier the fuel delivery and the pumping system reducing the manufacturing costs. Additionally, the crossover issue is no longer a major problem on this kind of micro-devices [278,279].

The use of methanol tolerant electrocatalysts such as Pt_xTi_y and Pt_xSe_y in an air-breathing methanol microfluidic fuel cell was further reported [280]. This study presented the improvement of a mixed-reactant micro fuel cell (MRFC) performance in comparison to a laminar flow fuel configuration (LFFC). We can observe that for the LFFC configuration, the anolyte and the catholyte contain 0.5 M H_2SO_4, Figure 47a. The 5M CH_3OH fuel is contained only in the anodic side. In the case of MRFC configuration, Figure 47b, the fuel (5M CH_3OH) and the supporting electrolyte (0.5 M H_2SO_4) are contained in only one reservoir [280].

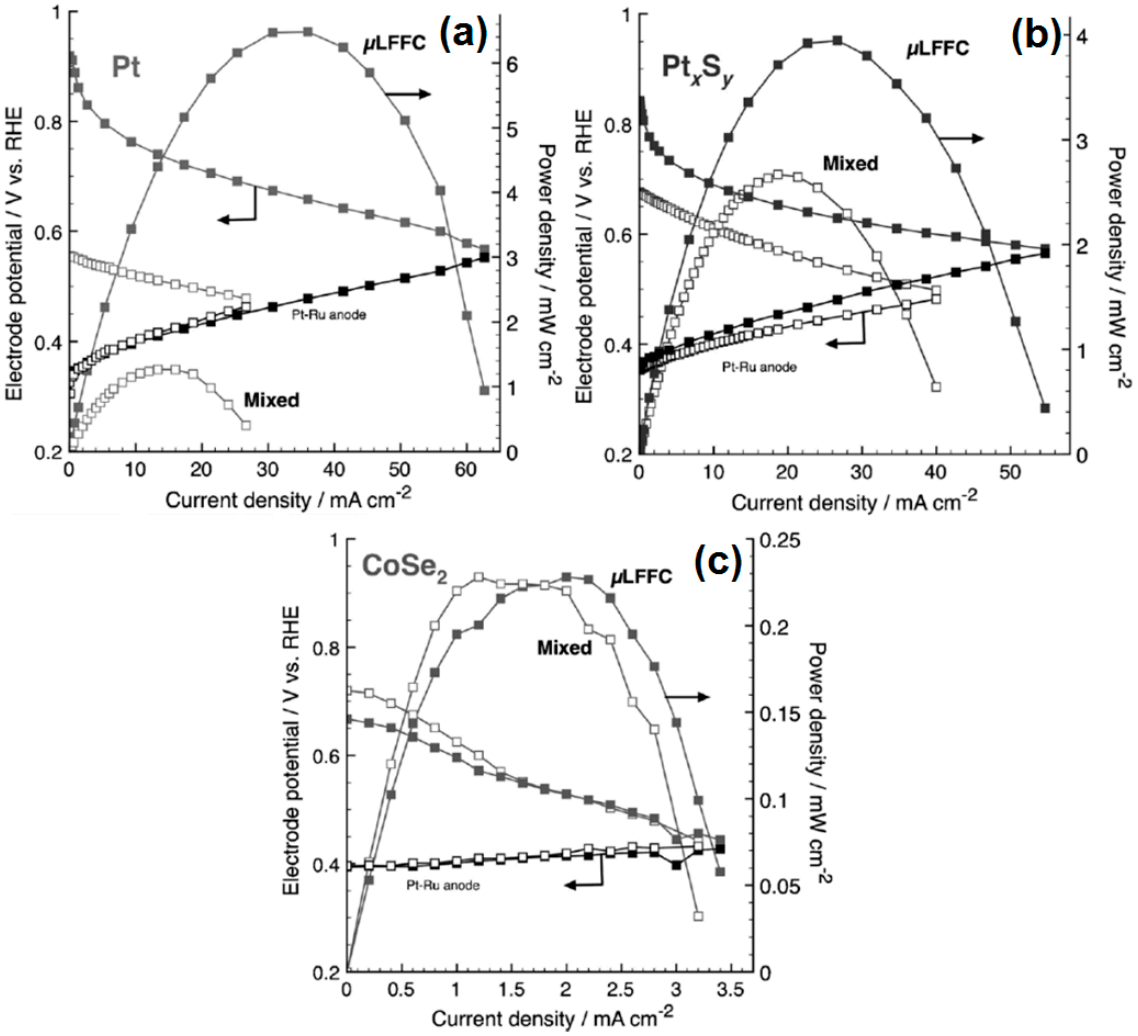

Figure 46. Anodic and cathodic polarization and power density curves of the μLFFCs with (**a**) Pt; (**b**) Pt_xS_y; and (**c**) $CoSe_2$ cathode catalysts. 5 M CH_3OH was used as fuel in the anodic stream (solid symbols) and in both streams (empty symbols) [278]. Reprinted with permission from [278]. Copyright Elsevier, 2012.

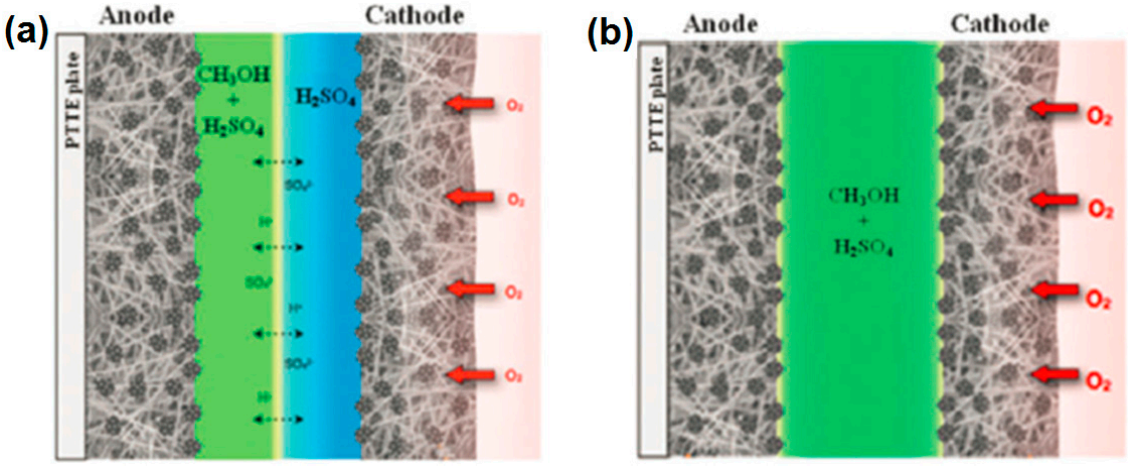

Figure 47. Laminar flow fuel cell configurations; (**a**) Insolated fuel cell and (**b**) mixed-reactant fuel cell [280]. Reprinted with permission from [280]. Copyright the Royal Society of Chemistry, 2014.

The individual anodic and cathodic polarizations for the Pt/C, Pt_xTi_y/C and Pt_xSe_y/C electrocatalysts are presented in Figure 48a–c. In the mixed-reactant condition a mixed potential between the oxygen reduction and the methanol oxidation is formed at the surface of the non-tolerant cathode. Because an inhibition effect caused by the Ti atoms on the Pt surface, the Pt_xTi_y/C overcame the potential value obtained for Pt/C [63]. Interestingly, the Pt_xSe_y/C presented a similar but enhanced effect, this electrocatalyst presented a selectivity to reduces de oxygen instead of oxidizing the methanol contained in the electrolytic solution. Thus, it allows the minimization of the methanol poisoning by the use of Se coordinated atoms onto the Pt surface [280].

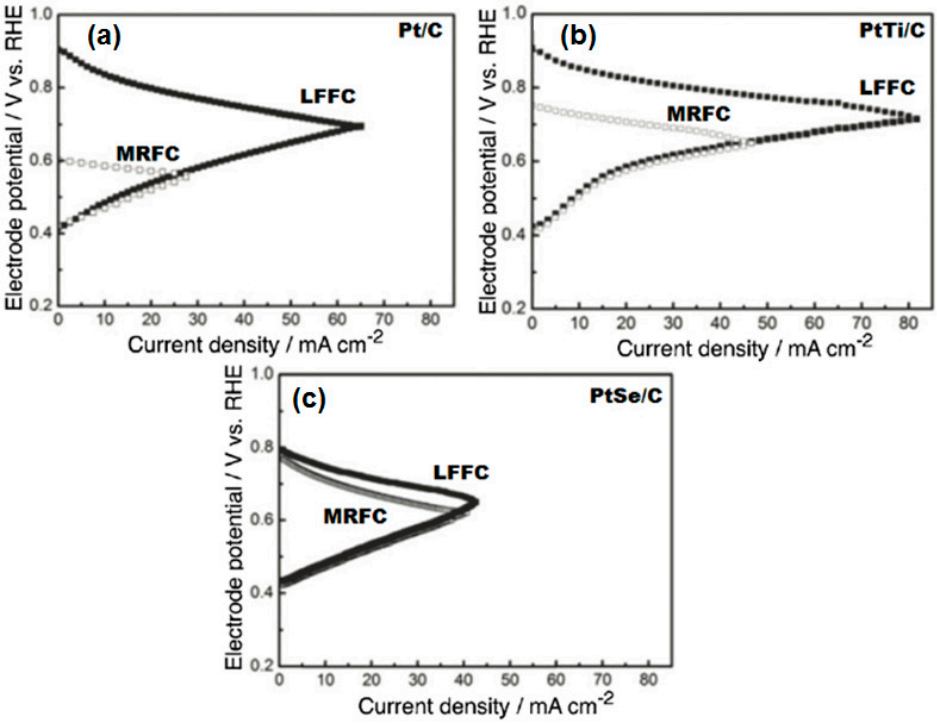

Figure 48. Current-potential polarizations for air-breathing methanol laminar flow fuel cell and mixed reactant flow cell (LFFC and MRFC, respectively) systems for (**a**) Pt/C; (**b**) Pt_xTi_y/C and (**c**) Pt_xSe_y/C cathode catalysts [280]. Reprinted with permission from [280]. Copyright the Royal Society of Chemistry, 2014.

Furthermore, recent studies showed that is possible to improve the electrocatalytic activity of non-precious $CoSe_2$ electrocatalysts evaluated in alkaline medium, with different carbon supports [229]. From this study, it was determined that a $CoSe_2$/NCNH electrocatalyst showed a lower onset overpotential than $CoSe_2$ supported on carbon, and carbon nanohorns ($CoSe_2$/C and $CoSe_2$/CNH, respectively). To validate the half-cell results, a self-breathing µLFFC was constructed and the $CoSe_2$/NCNH was used as a methanol tolerant cathodic electrocatalyst. The highest maximum power density value of 10.05 mW·cm^{-2} was achieved with $CoSe_2$/NCNH (5 M methanol as the fuel), Figure 49. This enhancement presented by $CoSe_2$/NCNH suggests a modification of the $CoSe_2$ active center by an interaction with the NCNH support [229].

Nanostructured palladium electrocatalysts supported on Vulcan carbon XC-72 were synthesized via the carbonyl chemical route and studied in micro-laminar flow fuel cells [56]. When these materials were evaluated to perform the oxidation of organic molecules, they presented a relationship between the electrocatalysts morphology and their electrochemical activity. A 20 wt % metal loading Pd/C electrocatalyst was selected to be used as anode in a direct formic acid µLFFC. As we can observe in Figure 50a, the power density in the direct formic acid µLFFC reached 14.7 mW·cm^{-2} with Pd/C-2, while its commercial counterpart Pd/C presented a power density value of 6.01 mW·cm^{-2}.

The individual polarization curves for the anode and cathode shown in Figure 50b, compares the performances of the anodes. While the cathodic polarization curves do not present variation. It turns out that the enhanced μLFFC performance is the result of a better oxidation reaction on the Pd/C-2 anode.

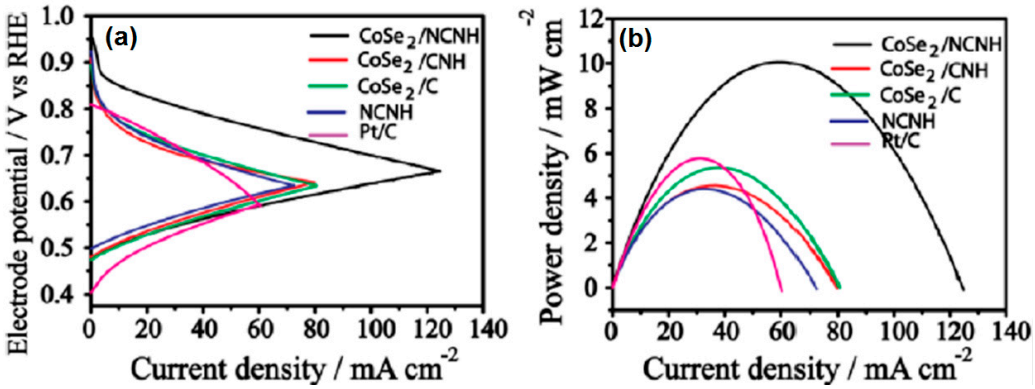

Figure 49. (**a**) Anodic and cathodic polarizations; and (**b**) power density curves of an air-breathing μLFFC with $CoSe_2$/NCNH, $CoSe_2$/CNH, $CoSe_2$/C, NCNHs and Pt/C as cathodes. A Pt-Ru/C electrode was used as the anode. A methanol solution 5 M was used as fuel in the alkaline solution [229]. Reprinted with permission from [229]. Copyright John Wiley and Sons, 2012.

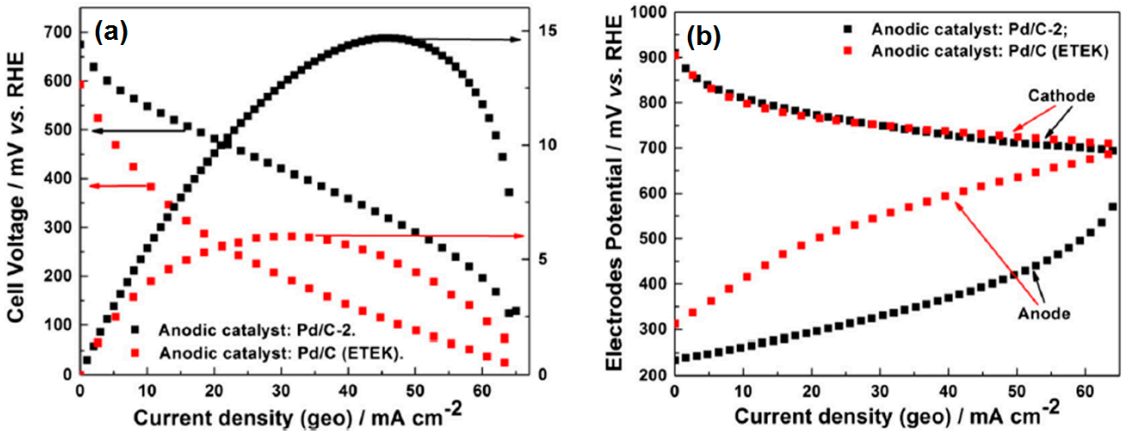

Figure 50. Formic Acid μLFFC. (**a**) cell polarization and power density curves; and (**b**) Anodic and cathodic polarization curves [56]. Reprinted with permission from [56]. Copyright Elsevier, 2016.

Pd/C-2 was also selected to perform the methanol oxidation reaction in a direct methanol μLFFC. Similarly, to the previous formic acid oxidation test, a commercial Pd/C electrode was used as reference material. From Figure 51a we can observe how the micro fuel cell configuration with Pd/C-2 as anode, presented a maximum power density value of 1.3 $mW \cdot cm^{-2}$ whereas the commercial counterpart reached only 0.45 $mW \cdot cm^{-2}$. In Figure 51b we can observe that the power density difference is the result of the anodic polarizations [56].

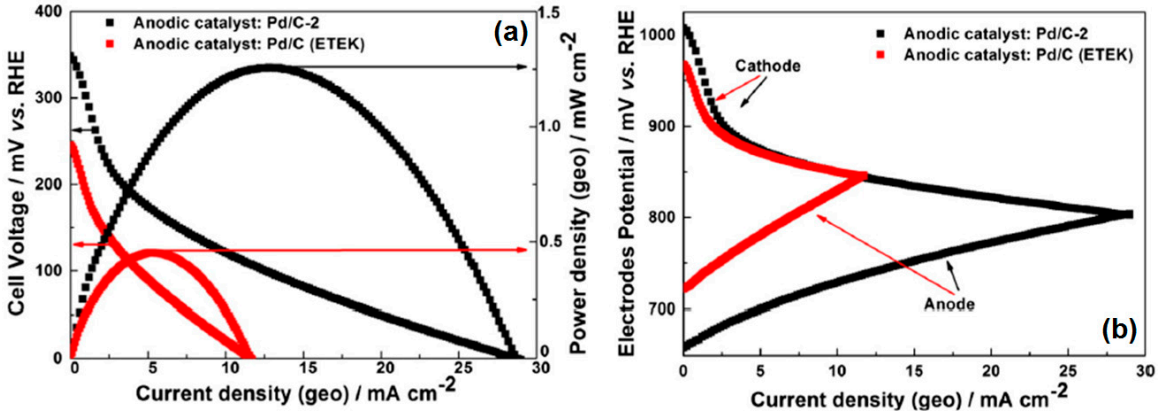

Figure 51. Direct Methanol μLFFC. (**a**) cell polarization and power density curves; and (**b**) electrode polarization curves [56]. Reprinted with permission from [56]. Copyright Elsevier, 2016.

5. Concluding Remarks

An attempt regarding the development of electrocatalytic materials has been outlined in this review. The activity and stability towards the ORR on Pt and Pd nanoparticles can be attained through ligand and support effects. The former focuses on synthesis of Pt or Pd nanoalloyed with a transition metals (ex. Co, Ni, etc.). The latter is tailoring the SMSI phenomenon, to attain the electronic, surface and structural modification of the catalytic center. The main trend in this direction is the application of highly graphitic carbon, carbon-oxide composites, and conducting/semiconducting oxide as supports. In this sense, significant progress in catalytic process on the catalytic center has been so far achieved. As pointed out herein, low temperature synthetic routes, e.g., carbonyl chemical or photo-deposition, was successfully employed.

The photo-deposition is particularly interesting for Pt-based NPs anchored onto high graphitic carbon, semiconducting oxide, and oxide-carbon composites. Strong metal support interaction (SMSI) between platinum and support could be reinforced, increasing the stability of catalytic center for ORR process. In addition, by means of Ti, Se or/and Cr as ligands, the tolerance of Pt was enhanced, favoring their application in a fuel cell using small organics, such as methanol as a fuel. Non-platinum metal chalcogenides, such as Ru_xSe_y and $CoSe_2$, are methanol tolerant electrocatalysts for ORR. Compared with Pt or Pd-based catalysts, the non-precious metal ones showed less catalytic activity, but an enhanced tolerance to methanol leading to the use of mixed-reactant systems, since cross-over effect in direct methanol fuel cell can be reduced, as described through the micro-fuel cells platform. Pt- or Pd-based electrocatalysts are still the most active materials for the hydrogen oxidation reaction (HOR). Nevertheless, non-precious metal nanoalloy, such as CoNiMo, was identified as active for HOR. Research on such kind of electrocatalyst has still a long way to go.

Concerning the oxidation process of organic fuels, e.g., methanol, and formic acid, Pd-based catalysts showed increased activity with respect to Pt ones. Chalcogenide materials containing Pt and Pd were measured for ORR and various fuel oxidation in a micro-fluid fuel cell. The non-precious metal catalysts become more and more attractive. The mechanism for the catalytic activity of such centers is still to be developed. It seems that the morphological impact plays an important role on the electrocatalytic activity. Thus, efforts should be further devoted to this issue.

Acknowledgments: The authors thank all the co-workers, cited in the literature list, and the University of Poitiers, France.

Author Contributions: N. A.-V. conceived the manuscript and warranted the scientific scope. The data collection and drafting was made by J.M. M.-H. in close collaboration with Y.L. All authors fully contributed to the revision of the manuscript.

Conflicts of Interest: The authors declare no conflict of interest.

References

1. Perry, M.L.; Fuller, T.F. A historical perspective of fuel cell technology in the 20th century. *J. Electrochem. Soc.* **2002**, *149*, S59–S67. [CrossRef]
2. Haiping, X.; Li, K.; Xuhui, W. Fuel cell power system and high power DC-DC converter. *IEEE Trans. Power Electr.* **2004**, *19*, 1250–1255.
3. Jayasayee, K.; Veen, J.A.R.V.; Manivasagam, T.G.; Celebi, S.; Hensen, E.J.M.; de Bruijn, F.A. Oxygen reduction reaction (ORR) activity and durability of carbon supported PtM (Co, Ni, Cu) alloys: Influence of particle size and non-noble metals. *Appl. Catal. B: Environ.* **2012**, *111–112*, 515–526. [CrossRef]
4. Gasteiger, H.A.; Kocha, S.S.; Sompalli, B.; Wagner, F.T. Activity benchmarks and requirements for Pt, Pt-alloy, and non-Pt oxygen reduction catalysts for PEMFCs. *Appl. Catal. B: Environ.* **2005**, *56*, 9–35. [CrossRef]
5. Ezeta, A.; Arce, E.M.; Solorza, O.; González, R.G.; Dorantes, H. Effect of the leaching of Ru-Se-Fe and Ru-Mo-Fe obtained by mechanical alloying on electrocatalytical behavior for the oxygen reduction reaction. *J. Alloys Compd.* **2009**, *483*, 429–431. [CrossRef]
6. Suryanarayana, C. Mechanical alloying and milling. *Prog. Mater. Sci.* **2001**, *46*, 1–184. [CrossRef]
7. Mukerjee, S.; Srinivasan, S.; Soriaga, M.P.; McBreen, J. Role of structural and electronic properties of Pt and Pt alloys on electrocatalysis of oxygen reduction: An in situ XANES and EXAFS investigation. *J. Electrochem. Soc.* **1995**, *142*, 1409–1422. [CrossRef]
8. Chen, S.; Ferreira, P.J.; Sheng, W.; Yabuuchi, N.; Allard, L.F.; Shao-Horn, Y. Enhanced activity for oxygen reduction reaction on "Pt_3Co" nanoparticles: Direct evidence of percolated and sandwich-segregation structures. *J. Am. Chem. Soc.* **2008**, *130*, 13818–13819. [CrossRef] [PubMed]
9. Min, M.-K.; Cho, J.; Cho, K.; Kim, H. Particle size and alloying effects of Pt-based alloy catalysts for fuel cell applications. *Electrochim. Acta* **2000**, *45*, 4211–4217. [CrossRef]
10. Guo, S.; Li, D.; Zhu, H.; Zhang, S.; Markovic, N.M.; Stamenkovic, V.R.; Sun, S. FePt and CoPt nanowires as efficient catalysts for the oxygen reduction reaction. *Angew. Chem. Int. Ed.* **2013**, *52*, 3465–3468. [CrossRef] [PubMed]
11. Shao, M.; Chang, Q.; Dodelet, J.-P.; Chenitz, R. Recent advances in electrocatalysts for oxygen reduction reaction. *Chem. Rev.* **2016**, *116*, 3594–3657. [CrossRef] [PubMed]
12. Greeley, J.; Stephens, I.E.L.; Bondarenko, A.S.; Johansson, T.P.; Hansen, H.A.; Jaramillo, T.F.; Rossmeisl, J.; Chorkendorff, I.; Nørskov, J.K. Alloys of platinum and early transition metals as oxygen reduction electrocatalysts. *Nat. Chem.* **2009**, *1*, 552–556. [CrossRef] [PubMed]
13. Pedersen, C.M.; Escudero-Escribano, M.; Velázquez-Palenzuela, A.; Christensen, L.H.; Chorkendorff, I.; Stephens, I.E.L. Benchmarking Pt-based electrocatalysts for low temperature fuel cell reactions with the rotating disk electrode: Oxygen reduction and hydrogen oxidation in the presence of CO. *Electrochim. Acta* **2015**, *179*, 647–657. [CrossRef]
14. Alonso-Vante, N.; Jaegermann, W.; Tributsch, H.; Hoenle, W.; Yvon, K. Electrocatalysis of oxygen reduction by chalcogenides containing mixed transition metal clusters. *J. Am. Chem. Soc.* **1987**, *109*, 3251–3257. [CrossRef]
15. Alonso-Vante, N. Chevrel phase and cluster-like chalcogenide materials. In *Handbook of Fuel Cells*; Vielstich, W., Lamm, A., Gasteiger, H., Eds.; John Wiley & Sons, Ltd.: Chichester, UK, 2003; Volume 2, pp. 534–543.
16. Friedrich, K.A.; Geyzers, K.P.; Linke, U.; Stimming, U.; Stumper, J. Co adsorption and oxidation on a Pt(111) electrode modified by ruthenium deposition: An ir spectroscopic study. *J. Electroanal. Chem.* **1996**, *402*, 123–128. [CrossRef]
17. Piazza, S.; Kühne, H.M.; Tributsch, H. Photoelectrochemical and electrocatalytic behaviour of p-type ruthenium disulphide electrodes. *J. Electroanal. Chem.* **1985**, *196*, 53–67. [CrossRef]
18. Bewick, A.; Gutiérrez, C.; Larramona, G. An international journal devoted to all aspects of electrode kinetics, interfacial structure, properties of electrolytes, colloid and biological electrochemistryin-situ IR spectroscopy study of the ruthenium electrode in acid and alkaline solutions. *J. Electroanal. Chem.* **1992**, *332*, 155–167. [CrossRef]
19. Alonso-Vante, N. Spectral sensitization of titanium dioxide electrodes via Ru-based chalcogenides thin layers. *Sol. Energy Mater. Sol. C* **1994**, *31*, 509–524. [CrossRef]

20. Chang, C.C.; Wen, T.C. Kinetics of oxygen reduction at RuO_2-coated titanium electrode in alkaline solution. *J. Appl. Electrochem.* **1997**, *27*, 355–363. [CrossRef]
21. González-Cruz, R.; Solorza-Feria, O. Oxygen reduction in acid media by a $Ru_xFe_ySe_z(CO)_n$ cluster catalyst dispersed on a glassy carbon-supported nafion film. *J. Sol. State Electrochem.* **2003**, *7*, 289–295. [CrossRef]
22. Cheng, H.; Yuan, W.; Scott, K. The influence of a new fabrication procedure on the catalytic activity of ruthenium–selenium catalysts. *Electrochim. Acta* **2006**, *52*, 466–473. [CrossRef]
23. Nagabhushana, K.S.; Dinjus, E.; Bönnemann, H.; Zaikovskii, V.; Hartnig, C.; Zehl, G.; Dorbandt, I.; Fiechter, S.; Bogdanoff, P. Reductive annealing for generating Se doped 20 wt % Ru/C cathode catalysts for the oxygen reduction reaction. *J. Appl. Electrochem.* **2007**, *37*, 1515–1522. [CrossRef]
24. Montiel, M.; García-Rodríguez, S.; Hernández-Fernández, P.; Díaz, R.; Rojas, S.; Fierro, J.L.G.; Fatás, E.; Ocón, P. Relevance of the synthesis route of Se-modified Ru/C as methanol tolerant electrocatalysts for the oxygen reduction reaction. *J. Power Sources* **2010**, *195*, 2478–2487. [CrossRef]
25. Suárez-Alcántara, K.; Solorza-Feria, O. Kinetics and PEMFC performance of $Ru_xMo_ySe_z$ nanoparticles as a cathode catalyst. *Electrochim. Acta* **2008**, *53*, 4981–4989. [CrossRef]
26. Koper, M.T.M. Electrocatalysis on bimetallic and alloy surfaces. *Surf. Sci.* **2004**, *548*, 1–3. [CrossRef]
27. He, T.; Kreidler, E.; Xiong, L.; Ding, E. Combinatorial screening and nano-synthesis of platinum binary alloys for oxygen electroreduction. *J. Power Sources* **2007**, *165*, 87–91. [CrossRef]
28. Anastasijević, N.A.; Vesović, V.; Adžić, R.R. Determination of the kinetic parameters of the oxygen reduction reaction using the rotating ring-disk electrode. *J. Electroanal. Chem. Interfacial Electrochem.* **1987**, *229*, 305–316. [CrossRef]
29. Kalevaru, V.N.; Benhmid, A.; Radnik, J.; Pohl, M.M.; Bentrup, U.; Martin, A. Marked influence of support on the catalytic performance of PdSb acetoxylation catalysts: Effects of Pd particle size, valence states, and acidity characteristics. *J. Catal.* **2007**, *246*, 399–412. [CrossRef]
30. Bagotzky, V.S.; Shumilova, N.A.; Samoilov, G.P.; Khrushcheva, E.I. Electrochemical oxygen reduction on nickel electrodes in alkaline solutions—II. *Electrochim. Acta* **1972**, *17*, 1625–1635. [CrossRef]
31. Ju, W.; Favaro, M.; Durante, C.; Perini, L.; Agnoli, S.; Schneider, O.; Stimming, U.; Granozzi, G. Pd nanoparticles deposited on nitrogen-doped HOPG: New insights into the Pd-catalyzed oxygen reduction reaction. *Electrochim. Acta* **2014**, *141*, 89–101. [CrossRef]
32. Chen, J.; Takanabe, K.; Ohnishi, R.; Lu, D.; Okada, S.; Hatasawa, H.; Morioka, H.; Antonietti, M.; Kubota, J.; Domen, K. Nano-sized tin on carbon black as an efficient electrocatalyst for the oxygen reduction reaction prepared using an MPG-C_3N_4 template. *Chem. Commun.* **2010**, *46*, 7492–7494. [CrossRef] [PubMed]
33. Wu, J.; Gross, A.; Yang, H. Shape and composition-controlled platinum alloy nanocrystals using carbon monoxide as reducing agent. *Nano Lett.* **2011**, *11*, 798–802. [CrossRef] [PubMed]
34. Vukmirovic, M.B.; Zhang, J.; Sasaki, K.; Nilekar, A.U.; Uribe, F.; Mavrikakis, M.; Adzic, R.R. Platinum monolayer electrocatalysts for oxygen reduction. *Electrochim. Acta* **2007**, *52*, 2257–2263. [CrossRef]
35. Salvador-Pascual, J.J.; Citalán-Cigarroa, S.; Solorza-Feria, O. Kinetics of oxygen reduction reaction on nanosized Pd electrocatalyst in acid media. *J. Power Sources* **2007**, *172*, 229–234. [CrossRef]
36. Sánchez-Sánchez, C.M.; Bard, A.J. Hydrogen peroxide production in the oxygen reduction reaction at different electrocatalysts as quantified by scanning electrochemical microscopy. *Anal. Chem.* **2009**, *81*, 8094–8100. [CrossRef] [PubMed]
37. Shao, M.-H.; Sasaki, K.; Adzic, R.R. Pd–Fe nanoparticles as electrocatalysts for oxygen reduction. *J. Am. Chem. Soc.* **2006**, *128*, 3526–3527. [CrossRef] [PubMed]
38. Shao, M.; Liu, P.; Zhang, J.; Adzic, R. Origin of enhanced activity in palladium alloy electrocatalysts for oxygen reduction reaction. *J. Phys. Chem. B* **2007**, *111*, 6772–6775. [CrossRef] [PubMed]
39. Liu, H.; Manthiram, A. Tuning the electrocatalytic activity and durability of low cost $Pd_{70}Co_{30}$ nanoalloy for oxygen reduction reaction in fuel cells. *Electrochem. Commun.* **2008**, *10*, 740–744. [CrossRef]
40. Kirubakaran, A.; Jain, S.; Nema, R.K. A review on fuel cell technologies and power electronic interface. *Renew. Sust. Energy Rev.* **2009**, *13*, 2430–2440. [CrossRef]
41. Mora-Hernández, J.M.; Ezeta-Mejía, A.; Reza-San Germán, C.; Citalán-Cigarroa, S.; Arce-Estrada, E.M. Electrochemical activity towards ORR of mechanically alloyed PdCo supported on vulcan carbon and carbon nanospheres. *J. Appl. Electrochem.* **2014**, *44*, 1307–1315. [CrossRef]

42. Lee, Y.-W.; Ko, A.R.; Kim, D.-Y.; Han, S.-B.; Park, K.-W. Octahedral Pt-Pd alloy catalysts with enhanced oxygen reduction activity and stability in proton exchange membrane fuel cells. *RSC Adv.* **2012**, *2*, 1119–1125. [CrossRef]
43. Antolini, E. Palladium in fuel cell catalysis. *Energy Environ. Sci.* **2009**, *2*, 915–931. [CrossRef]
44. Calvo, S.R.; Balbuena, P.B. Density functional theory analysis of reactivity of Pt_xPd_y alloy clusters. *Surf. Sci.* **2007**, *601*, 165–171. [CrossRef]
45. Shen, P.K.; Xu, C. Alcohol oxidation on nanocrystalline oxide Pd/C promoted electrocatalysts. *Electrochem. Commun.* **2006**, *8*, 184–188. [CrossRef]
46. Zhang, S.; Shao, Y.; Yin, G.; Lin, Y. Electrostatic self-assembly of a Pt-around-Au nanocomposite with high activity towards formic acid oxidation. *Angew. Chem. Int. Ed.* **2010**, *49*, 2211–2214. [CrossRef] [PubMed]
47. Ha, S.; Larsen, R.; Masel, R.I. Performance characterization of Pd/C nanocatalyst for direct formic acid fuel cells. *J. Power Sources* **2005**, *144*, 28–34. [CrossRef]
48. Zhu, Y.; Khan, Z.; Masel, R.I. The behavior of palladium catalysts in direct formic acid fuel cells. *J. Power Sources* **2005**, *139*, 15–20. [CrossRef]
49. Alonso-Vante, N. Tailoring of metal cluster-like materials for the molecular oxygen reduction reaction. *Pure Appl. Chem.* **2008**, *80*, 2103–2114. [CrossRef]
50. Gago Aldo, S.; Habrioux, A.; Alonso-Vante, N. Tailoring nanostructured catalysts for electrochemical energy conversion systems. *Nanotechnol. Rev.* **2012**, *1*, 427–453. [CrossRef]
51. Alonso-Vante, N. Carbonyl tailored electrocatalysts. *Fuel Cells* **2006**, *6*, 182–189. [CrossRef]
52. Le Rhun, V.; Garnier, E.; Pronier, S.; Alonso-Vante, N. Electrocatalysis on nanoscale ruthenium-based material manufactured by carbonyl decomposition. *Electrochem. Commun.* **2000**, *2*, 475–479. [CrossRef]
53. Yang, H.; Alonso-Vante, N.; Lamy, C.; Akins, D.L. High methanol tolerance of carbon-supported Pt-Cr alloy nanoparticle electrocatalysts for oxygen reduction. *J. Electrochem. Soc.* **2005**, *152*, A704–A709. [CrossRef]
54. Yang, H.; Alonso-Vante, N.; Léger, J.-M.; Lamy, C. Tailoring, structure, and activity of carbon-supported nanosized Pt–Cr alloy electrocatalysts for oxygen reduction in pure and methanol-containing electrolytes. *J. Phys. Chem. B* **2004**, *108*, 1938–1947. [CrossRef]
55. Yang, H.; Vogel, W.; Lamy, C.; Alonso-Vante, N. Structure and electrocatalytic activity of carbon-supported Pt–Ni alloy nanoparticles toward the oxygen reduction reaction. *J. Phys. Chem. B* **2004**, *108*, 11024–11034. [CrossRef]
56. Luo, Y.; Mora-Hernández, J.M.; Alonso-Vante, N. Morphological impact onto organic fuel oxidation of nanostructured palladium synthesized via carbonyl chemical route. *J. Electroanal. Chem.* **2016**, *765*, 79–86. [CrossRef]
57. Luo, Y.; Mora-Hernández, J.M.; Estudillo-Wong, L.A.; Arce-Estrada, E.M.; Alonso-Vante, N. Nanostructured palladium tailored via carbonyl chemical route towards oxygen reduction reaction. *Electrochim. Acta* **2015**, *173*, 771–778. [CrossRef]
58. Longoni, G.; Chini, P. Synthesis and chemical characterization of platinum carbonyl dianions $[Pt_3(CO)_6]_n^{2-}$ (n = .apprx.10,6,5,4,3,2,1). A new series of inorganic oligomers. *J. Am. Chem. Soc.* **1976**, *98*, 7225–7231. [CrossRef]
59. Manzo-Robledo, A.; Boucher, A.C.; Pastor, E.; Alonso-Vante, N. Electro-oxidation of carbon monoxide and methanol on carbon-supported Pt–Sn nanoparticles: A dems study. *Fuel Cells* **2002**, *2*, 109–116. [CrossRef]
60. Yang, H.; Coutanceau, C.; Léger, J.-M.; Alonso-Vante, N.; Lamy, C. Methanol tolerant oxygen reduction on carbon-supported Pt–Ni alloy nanoparticles. *J. Electroanal. Chem.* **2005**, *576*, 305–313. [CrossRef]
61. Ma, J.; Gago, A.S.; Alonso-Vante, N. Performance study of platinum nanoparticles supported onto MWCNT in a formic acid microfluidic fuel cell system. *J. Electrochem. Soc.* **2013**, *160*, F859–F866. [CrossRef]
62. Kondo, T.; Iwasaki, Y.; Honma, Y.; Takagi, Y.; Okada, S.; Nakamura, J. Formation of nonbonding π electronic states of graphite due to Pt-C hybridization. *Phys. Rev. B* **2009**, *80*, 233408. [CrossRef]
63. Ma, J.; Habrioux, A.; Miyao, T.; Kakinuma, K.; Inukai, J.; Watanabe, M.; Alonso-Vante, N. Correlation between surface chemical composition with catalytic activity and selectivity of organic-solvent synthesized Pt-Ti nanoparticles. *J. Mater. Chem. A* **2013**, *1*, 8798–8804. [CrossRef]
64. Alonso-Vante, N.; Schubert, B.; Tributsch, H. Transition metal cluster materials for multi-electron transfer catalysis. *Mater. Chem. Phys.* **1989**, *22*, 281–307. [CrossRef]
65. Chevrel, R.; Sergent, M.; Prigent, J. Sur de nouvelles phases sulfurées ternaires du molybdène. *J. Solid State Chem.* **1971**, *3*, 515–519. (In French) [CrossRef]

66. Perrin, A.; Chevrel, R.; Sergent, M.; Fischer, Ø. Synthesis and electrical properties of new chalcogenide compounds containing mixed (Mo, Me)$_6$ octahedral clusters (Me = Ru or Rh). *J. Sol. State Chem.* **1980**, *33*, 43–47. [CrossRef]
67. Perrin, A.; Sergent, M.; Fischer, O. New compounds of the type $Mo_2Re_4X_8$ (M = S, Se) containing octahedral Mo_2Re_4 clusters. *Mater. Res. Bull.* **1978**, *13*, 259–264. [CrossRef]
68. Alonso-Vante, N.; Tributsch, H. Energy conversion catalysis using semiconducting transition metal cluster compounds. *Nature* **1986**, *323*, 431–432. [CrossRef]
69. Alonso-Vante, N.; Tributsch, H. what. *J. Electroanal. Chem. Interfacial Electrochem.* **1987**, *229*, 223–237.
70. Kühne, H.M.; Tributsch, H. Oxygen and chlorine evolution on ruthenium-iron-disulphide mediated by low energy photons. *Ber. Bunsenges. Physikalische Chem.* **1984**, *88*, 10–16. [CrossRef]
71. Kühne, H.M.; Tributsch, H. Energetics and dynamics of the interface of RuS_2 and implications for photoelectrolysis of water. *J. Electroanal. Chem. Interfacial Electrochem.* **1986**, *201*, 263–282. [CrossRef]
72. Vante, N.A.; Schubert, B.; Tributsch, H.; Perrin, A. Influence of d-state density and chemistry of transition metal cluster selenides on electrocatalysis. *J. Catal.* **1988**, *112*, 384–391. [CrossRef]
73. Hughbanks, T.; Hoffmann, R. Molybdenum chalcogenides: Clusters, chains, and extended solids. The approach to bonding in three dimensions. *J. Am. Chem. Soc.* **1983**, *105*, 1150–1162. [CrossRef]
74. Jaegermann, W.; Pettenkofer, C.; Alonso Vante, N.; Schwarzlose, T.; Tributsch, H. Chevrel phase type compounds: Electronic, chemical and structural factors in oxygen reduction electrocatalysis. *Ber. Bunsenges. Phys. Chem.* **1990**, *94*, 513–520. [CrossRef]
75. Solorza-Feria, O.; Ellmer, K.; Giersig, M.; Alonso-Vante, N. Novel low-temperature synthesis of semiconducting transition metal chalcogenide electrocatalyst for multielectron charge transfer: Molecular oxygen reduction. *Electrochim. Acta* **1994**, *39*, 1647–1653. [CrossRef]
76. Kochubey, D.I.; Nikitenko, S.G.; Parmon, V.N.; Gruzdkov, Yu.A.; Tributsch, H.; Alonso-Vante, N. In situ EXAFS-electrochemical study of reduction of molecular oxygen on Mo□Ru□Se thin layers electrodes in acidic media. *Phys. B Condens. Matter* **1995**, *208–209*, 694–696. [CrossRef]
77. Schmidt, T.J.; Paulus, U.A.; Gasteiger, H.A.; Alonso-Vante, N.; Behm, R.J. Oxygen reduction on $Ru_{1.92}Mo_{0.08}SeO_4$, Ru/carbon, and Pt/carbon in pure and methanol-containing electrolytes. *J. Electrochem. Soc.* **2000**, *147*, 2620–2624. [CrossRef]
78. Dassenoy, F.; Vogel, W.; Alonso-Vante, N. Structural studies and stability of cluster-like Ru_xSe_y electrocatalysts. *J. Phys. Chem. B* **2002**, *106*, 12152–12157. [CrossRef]
79. Alonso-Vante, N.; Borthen, P.; Fieber-Erdmann, M.; Strehblow, H.H.; Holub-Krappe, E. An in situ grazing incidence X-ray absorption study of ultra thin ruxsey cluster-like electrocatalyst layers. *Electrochim. Acta* **2000**, *45*, 4227–4236. [CrossRef]
80. Malakhov, I.V.; Nikitenko, S.G.; Savinova, E.R.; Kochubey, D.I.; Alonso-Vante, N. In situ EXAFS study to probe active centers of Ru chalcogenide electrocatalysts during oxygen reduction reaction. *J. Phys. Chem. B* **2002**, *106*, 1670–1676. [CrossRef]
81. Babu, P.K.; Lewera, A.; Jong, H.C.; Hunger, R.; Jaegermann, W.; Alonso-Vante, N.; Wieckowski, A.; Oldfield, E. Selenium becomes metallic in Ru-Se fuel cell catalysts: An EC-NMR and XPS investigation. *J. Am. Chem. Soc.* **2007**, *129*, 15140–15141. [CrossRef] [PubMed]
82. Cao, D.; Wieckowski, A.; Inukai, J.; Alonso-Vante, N. Oxygen reduction reaction on ruthenium and rhodium nanoparticles modified with selenium and sulfur. *J. Electrochem. Soc.* **2006**, *153*, A869–A874. [CrossRef]
83. Ma, J.; Gago, A.S.; Vogel, W.; Alonso-Vante, N. Tailoring and tuning the tolerance of a Pt chalcogenide cathode electrocatalyst to methanol. *ChemCatChem* **2013**, *5*, 701–705. [CrossRef]
84. Nie, Y.; Li, L.; Wei, Z. Recent advancements in Pt and Pt-free catalysts for oxygen reduction reaction. *Chem. Soc. Rev.* **2015**, *44*, 2168–2201. [CrossRef] [PubMed]
85. Borup, R.; Meyers, J.; Pivovar, B.; Kim, Y.S.; Mukundan, R.; Garland, N.; Myers, D.; Wilson, M.; Garzon, F.; Wood, D.; et al. Scientific aspects of polymer electrolyte fuel cell durability and degradation. *Chem. Rev.* **2007**, *107*, 3904–3951. [CrossRef] [PubMed]
86. Su, D.S.; Sun, G. Nonprecious-metal catalysts for low-cost fuel cells. *Angew. Chem. Int. Ed.* **2011**, *50*, 11570–11572. [CrossRef] [PubMed]
87. Behret, H.; Binder, H.; Sandstede, G. Electrocatalytic oxygen reduction with thiospinels and other sulphides of transition metals. *Electrochim. Acta* **1975**, *20*, 111–117. [CrossRef]

88. Feng, Y.; Alonso-Vante, N. Nonprecious metal catalysts for the molecular oxygen-reduction reaction. *Phys. Status Solidi* **2008**, *245*, 1792–1806. [CrossRef]
89. Puntes, V.F.; Krishnan, K.M.; Alivisatos, A.P. Colloidal nanocrystal shape and size control: The case of cobalt. *Science* **2001**, *291*, 2115–2117. [CrossRef] [PubMed]
90. Yang, H.T.; Shen, C.M.; Wang, Y.G.; Su, Y.K.; Yang, T.Z.; Gao, H.J. Stable cobalt nanoparticles passivated with oleic acid and triphenylphosphine. *Nanotechnology* **2004**, *15*, 70. [CrossRef]
91. Yin, Y.; Rioux, R.M.; Erdonmez, C.K.; Hughes, S.; Somorjai, G.A.; Alivisatos, A.P. Formation of hollow nanocrystals through the nanoscale kirkendall effect. *Science* **2004**, *304*, 711–714. [CrossRef] [PubMed]
92. Sidik, R.A.; Anderson, A.B. Co_9S_8 as a catalyst for electroreduction of O_2: Quantum chemistry predictions. *J. Phys. Chem. B* **2006**, *110*, 936–941. [CrossRef] [PubMed]
93. Vayner, E.; Sidik, R.A.; Anderson, A.B.; Popov, B.N. Experimental and theoretical study of cobalt selenide as a catalyst for O_2 electroreduction. *J. Phys. Chem. C* **2007**, *111*, 10508–10513. [CrossRef]
94. Feng, Y.; He, T.; Alonso-Vante, N. In situ free-surfactant synthesis and ORR- electrochemistry of carbon-supported Co_3S_4 and $CoSe_2$ nanoparticles. *Chem. Mater.* **2008**, *20*, 26–28. [CrossRef]
95. Feng, Y.; He, T.; Alonso-Vante, N. Oxygen reduction reaction on carbon-supported $CoSe_2$ nanoparticles in an acidic medium. *Electrochim. Acta* **2009**, *54*, 5252–5256. [CrossRef]
96. Susac, D.; Sode, A.; Zhu, L.; Wong, P.C.; Teo, M.; Bizzotto, D.; Mitchell, K.A.R.; Parsons, R.R.; Campbell, S.A. A methodology for investigating new nonprecious metal catalysts for PEM fuel cells. *J. Phys. Chem. B* **2006**, *110*, 10762–10770. [CrossRef] [PubMed]
97. Susac, D.; Zhu, L.; Teo, M.; Sode, A.; Wong, K.C.; Wong, P.C.; Parsons, R.R.; Bizzotto, D.; Mitchell, K.A.R.; Campbell, S.A. Characterization of FeS_2-based thin films as model catalysts for the oxygen reduction reaction. *J. Phys. Chem. C* **2007**, *111*, 18715–18723. [CrossRef]
98. Zhu, L.; Susac, D.; Teo, M.; Wong, K.C.; Wong, P.C.; Parsons, R.R.; Bizzotto, D.; Mitchell, K.A.R.; Campbell, S.A. Investigation of CoS_2-based thin films as model catalysts for the oxygen reduction reaction. *J. Catal.* **2008**, *258*, 235–242. [CrossRef]
99. Ahlberg, E.; Elfström Broo, A. Oxygen reduction at sulphide minerals. 1. A rotating ring disc electrode (RRDE) study at galena and pyrite. *Int. J. Miner. Process.* **1996**, *46*, 73–89. [CrossRef]
100. Bonakdarpour, A.; Delacote, C.; Yang, R.; Wieckowski, A.; Dahn, J.R. Loading of Se/Ru/C electrocatalyst on a rotating ring-disk electrode and the loading impact on a H_2O_2 release during oxygen reduction reaction. *Electrochem. Commun.* **2008**, *10*, 611–615. [CrossRef]
101. Alonso-Vante, N. Platinum and non-platinum nanomaterials for the molecular oxygen reduction reaction. *ChemPhysChem* **2010**, *11*, 2732–2744. [CrossRef] [PubMed]
102. Feng, Y.; Alonso-Vante, N. Carbon-supported cubic $CoSe_2$ catalysts for oxygen reduction reaction in alkaline medium. *Electrochim. Acta* **2012**, *72*, 129–133. [CrossRef]
103. Feng, Y.J.; He, T.; Alonso-Vante, N. Carbon-supported $CoSe_2$ nanoparticles for oxygen reduction reaction in acid medium. *Fuel Cells* **2010**, *10*, 77–83.
104. Liang, Y.; Li, Y.; Wang, H.; Zhou, J.; Wang, J.; Regier, T.; Dai, H. Co_3O_4 nanocrystals on graphene as a synergistic catalyst for oxygen reduction reaction. *Nat. Mater.* **2011**, *10*, 780–786. [CrossRef] [PubMed]
105. Sabatier, P. Hydrogénations et déshydrogénations par catalyse. *Ber. Dtsch. Chem. Ges.* **1911**, *44*, 1984–2001. [CrossRef]
106. Yang, B.; Burch, R.; Hardacre, C.; Headdock, G.; Hu, P. Understanding the optimal adsorption energies for catalyst screening in heterogeneous catalysis. *ACS Catal.* **2014**, *4*, 182–186. (In French) [CrossRef]
107. Maruyama, J.; Abe, I. Formation of platinum-free fuel cell cathode catalyst with highly developed nanospace by carbonizing catalase. *Chem. Mater.* **2005**, *17*, 4660–4667. [CrossRef]
108. Zhang, L.; Zhang, J.; Wilkinson, D.P.; Wang, H. Progress in preparation of non-noble electrocatalysts for PEM fuel cell reactions. *J. Power Sources* **2006**, *156*, 171–182. [CrossRef]
109. Wood, T.E.; Tan, Z.; Schmoeckel, A.K.; O'Neill, D.; Atanasoski, R. Non-precious metal oxygen reduction catalyst for PEM fuel cells based on nitroaniline precursor. *J. Power Sources* **2008**, *178*, 510–516. [CrossRef]
110. Rand, D.A.J.; Woods, R. Cyclic voltammetric studies on iridium electrodes in sulphuric acid solutions. *J. Electroanal. Chem. Interfacial Electrochem.* **1974**, *55*, 375–381. [CrossRef]
111. Croissant, M.J.; Napporn, T.; Léger, J.M.; Lamy, C. Electrocatalytic oxidation of hydrogen at platinum-modified polyaniline electrodes. *Electrochim. Acta* **1998**, *43*, 2447–2457. [CrossRef]

112. Cao, L.; Sun, G.; Li, H.; Xin, Q. Carbon-supported IrSn catalysts for direct ethanol fuel cell. *Fuel Cells Bull.* **2007**, *2007*, 12–16. [CrossRef]
113. Lee, K.; Zhang, L.; Zhang, J. Ir_xCO_{1-x} (x = 0.3–1.0) alloy electrocatalysts, catalytic activities, and methanol tolerance in oxygen reduction reaction. *J. Power Sources* **2007**, *170*, 291–296. [CrossRef]
114. Santos, E.; Schmickler, W. Electrocatalysis of hydrogen oxidation—Theoretical foundations. *Angew. Chem. Int. Ed.* **2007**, *46*, 8262–8265. [CrossRef] [PubMed]
115. Mokrane, S.; Makhloufi, L.; Alonso-Vante, N. Electrochemical behaviour of platinum nanoparticles supported on polypyrrole (PPY)/C composite. *ECS Trans.* **2008**, *6*, 93–103.
116. Shao, M. Palladium-based electrocatalysts for hydrogen oxidation and oxygen reduction reactions. *J. Power Sources* **2011**, *196*, 2433–2444. [CrossRef]
117. Kwon, K.; Jin, S.-A.; Lee, K.H.; You, D.J.; Pak, C. Performance enhancement of Pd-based hydrogen oxidation catalysts using tungsten oxide. *Catal. Today* **2014**, *232*, 175–178. [CrossRef]
118. Zhang, H.; Shen, P.K. Recent development of polymer electrolyte membranes for fuel cells. *Chem. Rev.* **2012**, *112*, 2780–2832. [CrossRef] [PubMed]
119. Sheng, W.; Bivens, A.P.; Myint, M.; Zhuang, Z.; Forest, R.V.; Fang, Q.; Chen, J.G.; Yan, Y. Non-precious metal electrocatalysts with high activity for hydrogen oxidation reaction in alkaline electrolytes. *Energy Environ. Sci.* **2014**, *7*, 1719–1724. [CrossRef]
120. Spendelow, J.S.; Wieckowski, A. Electrocatalysis of oxygen reduction and small alcohol oxidation in alkaline media. *PhysChemChemPhys* **2007**, *9*, 2654–2675. [CrossRef] [PubMed]
121. Neyerlin, K.C.; Gu, W.; Jorne, J.; Gasteiger, H.A. Study of the exchange current density for the hydrogen oxidation and evolution reactions. *J. Electrochem. Soc.* **2007**, *154*, B631–B635. [CrossRef]
122. Durst, J.; Siebel, A.; Simon, C.; Hasche, F.; Herranz, J.; Gasteiger, H.A. New insights into the electrochemical hydrogen oxidation and evolution reaction mechanism. *Energy Environ. Sci.* **2014**, *7*, 2255–2260. [CrossRef]
123. Greeley, J.; Jaramillo, T.F.; Bonde, J.; Chorkendorff, I.; Norskov, J.K. Computational high-throughput screening of electrocatalytic materials for hydrogen evolution. *Nat. Mater.* **2006**, *5*, 909–913. [CrossRef] [PubMed]
124. Gu, J.; Guo, Y.; Jiang, Y.-Y.; Zhu, W.; Xu, Y.-S.; Zhao, Z.-Q.; Liu, J.-X.; Li, W.-X.; Jin, C.-H.; Yan, C.-H.; et al. Robust phase control through hetero-seeded epitaxial growth for face-centered cubic Pt@Ru nanotetrahedrons with superior hydrogen electro-oxidation activity. *J. Phys. Chem. C* **2015**, *119*, 17697–17706. [CrossRef]
125. Kucernak, A.R.J.; Fahy, K.F.; Sundaram, V.N.N. Facile synthesis of palladium phosphide electrocatalysts and their activity for the hydrogen oxidation, hydrogen evolutions, oxygen reduction and formic acid oxidation reactions. *Catal. Today* **2016**, *262*, 48–56. [CrossRef]
126. Carenco, S.; Portehault, D.; Boissière, C.; Mézailles, N.; Sanchez, C. Nanoscaled metal borides and phosphides: Recent developments and perspectives. *Chem. Rev.* **2013**, *113*, 7981–8065. [CrossRef] [PubMed]
127. Henkes, A.E.; Vasquez, Y.; Schaak, R.E. Converting metals into phosphides: A general strategy for the synthesis of metal phosphide nanocrystals. *J. Am. Chem. Soc.* **2007**, *129*, 1896–1897. [CrossRef] [PubMed]
128. Barry, B.M.; Gillan, E.G. Low-temperature solvothermal synthesis of phosphorus-rich transition-metal phosphides. *Chem. Mater.* **2008**, *20*, 2618–2620. [CrossRef]
129. Alexander, A.-M.; Hargreaves, J.S.J. Alternative catalytic materials: Carbides, nitrides, phosphides and amorphous boron alloys. *Chem. Soc. Rev.* **2010**, *39*, 4388–4401. [CrossRef] [PubMed]
130. Shervedani, R.K.; Lasia, A. Studies of the hydrogen evolution reaction on Ni-P electrodes. *J. Electrochem. Soc.* **1997**, *144*, 511–519. [CrossRef]
131. Hu, C.C.; Bai, A. Optimization of hydrogen evolving activity on nickel–phosphorus deposits using experimental strategies. *J. Appl. Electrochem.* **2001**, *31*, 565–572. [CrossRef]
132. Popczun, E.J.; McKone, J.R.; Read, C.G.; Biacchi, A.J.; Wiltrout, A.M.; Lewis, N.S.; Schaak, R.E. Nanostructured nickel phosphide as an electrocatalyst for the hydrogen evolution reaction. *J. Am. Chem. Soc.* **2013**, *135*, 9267–9270. [CrossRef] [PubMed]
133. Kucernak, A.R.J.; Naranammalpuram Sundaram, V.N. Nickel phosphide: The effect of phosphorus content on hydrogen evolution activity and corrosion resistance in acidic medium. *J. Mater. Chem. A* **2014**, *2*, 17435–17445. [CrossRef]
134. Popczun, E.J.; Read, C.G.; Roske, C.W.; Lewis, N.S.; Schaak, R.E. Highly active electrocatalysis of the hydrogen evolution reaction by cobalt phosphide nanoparticles. *Angew. Chem. Int. Ed.* **2014**, *53*, 5427–5430. [CrossRef] [PubMed]

135. Xiao, P.; Sk, M.A.; Thia, L.; Ge, X.; Lim, R.J.; Wang, J.-Y.; Lim, K.H.; Wang, X. Molybdenum phosphide as an efficient electrocatalyst for the hydrogen evolution reaction. *Energy Environ. Sci.* **2014**, *7*, 2624–2629. [CrossRef]
136. McEnaney, J.M.; Chance Crompton, J.; Callejas, J.F.; Popczun, E.J.; Read, C.G.; Lewis, N.S.; Schaak, R.E. Electrocatalytic hydrogen evolution using amorphous tungsten phosphide nanoparticles. *Chem. Commun.* **2014**, *50*, 11026–11028. [CrossRef] [PubMed]
137. Lu, S.; Pan, J.; Huang, A.; Zhuang, L.; Lu, J. Alkaline polymer electrolyte fuel cells completely free from noble metal catalysts. *Proc. Natl. Acad. Sci. USA* **2008**, *105*, 20611–20614. [CrossRef]
138. Sakamoto, T.; Asazawa, K.; Sanabria-Chinchilla, J.; Martinez, U.; Halevi, B.; Atanassov, P.; Strasser, P.; Tanaka, H. Combinatorial discovery of Ni-based binary and ternary catalysts for hydrazine electrooxidation for use in anion exchange membrane fuel cells. *J. Power Sources* **2014**, *247*, 605–611. [CrossRef]
139. Brown, D.E.; Mahmood, M.N.; Man, M.C.M.; Turner, A.K. Preparation and characterization of low overvoltage transition metal alloy electrocatalysts for hydrogen evolution in alkaline solutions. *Electrochim. Acta* **1984**, *29*, 1551–1556. [CrossRef]
140. Bakos, I.; Paszternák, A.; Zitoun, D. Pd/Ni synergestic activity for hydrogen oxidation reaction in alkaline conditions. *Electrochim. Acta* **2015**, *176*, 1074–1082. [CrossRef]
141. Subbaraman, R.; Danilovic, N.; Lopes, P.P.; Tripkovic, D.; Strmcnik, D.; Stamenkovic, V.R.; Markovic, N.M. Origin of anomalous activities for electrocatalysts in alkaline electrolytes. *J. Phys. Chem. C* **2012**, *116*, 22231–22237. [CrossRef]
142. Henning, S.; Herranz, J.; Gasteiger, H.A. Bulk-palladium and palladium-on-gold electrocatalysts for the oxidation of hydrogen in alkaline electrolyte. *J. Electrochem. Soc.* **2015**, *162*, F178–F189. [CrossRef]
143. Subbaraman, R.; Tripkovic, D.; Strmcnik, D.; Chang, K.-C.; Uchimura, M.; Paulikas, A.P.; Stamenkovic, V.; Markovic, N.M. Enhancing hydrogen evolution activity in water splitting by tailoring Li^+-$Ni(OH)_2$-Pt interfaces. *Science* **2011**, *334*, 1256–1260. [CrossRef] [PubMed]
144. Scofield, M.E.; Zhou, Y.; Yue, S.; Wang, L.; Su, D.; Tong, X.; Vukmirovic, M.B.; Adzic, R.R.; Wong, S.S. Role of chemical composition in the enhanced catalytic activity of Pt-based alloyed ultrathin nanowires for the hydrogen oxidation reaction under alkaline conditions. *ACS Catal.* **2016**, *6*, 3895–3908. [CrossRef]
145. Scofield, M.E.; Koenigsmann, C.; Wang, L.; Liu, H.; Wong, S.S. Tailoring the composition of ultrathin, ternary alloy ptrufe nanowires for the methanol oxidation reaction and formic acid oxidation reaction. *Energy Environ. Sci.* **2015**, *8*, 350–363. [CrossRef]
146. Alia, S.M.; Larsen, B.A.; Pylypenko, S.; Cullen, D.A.; Diercks, D.R.; Neyerlin, K.C.; Kocha, S.S.; Pivovar, B.S. Platinum-coated nickel nanowires as oxygen-reducing electrocatalysts. *ACS Catal.* **2014**, *4*, 1114–1119. [CrossRef]
147. Kandoi, S.; Ferrin, P.A.; Mavrikakis, M. Hydrogen on and in selected overlayer near-surface alloys and the effect of subsurface hydrogen on the reactivity of alloy surfaces. *Top. Catal.* **2010**, *53*, 384–392. [CrossRef]
148. Rheinländer, P.J.; Herranz, J.; Durst, J.; Gasteiger, H.A. Kinetics of the hydrogen oxidation/evolution reaction on polycrystalline platinum in alkaline electrolyte reaction order with respect to hydrogen pressure. *J. Electrochem. Soc.* **2014**, *161*, F1448–F1457. [CrossRef]
149. Montero, M.A.; Gennero de Chialvo, M.R.; Chialvo, A.C. Kinetics of the hydrogen oxidation reaction on nanostructured rhodium electrodes in alkaline solution. *J. Power Sources* **2015**, *283*, 181–186. [CrossRef]
150. Montero, M.A.; Fernández, J.L.; Gennero de Chialvo, M.R.; Chialvo, A.C. Characterization and kinetic study of a nanostructured rhodium electrode for the hydrogen oxidation reaction. *J. Power Sources* **2014**, *254*, 218–223. [CrossRef]
151. Montero, M.A.; Fernández, J.L.; Gennero de Chialvo, M.R.; Chialvo, A.C. Kinetic study of the hydrogen oxidation reaction on nanostructured iridium electrodes in acid solutions. *J. Phys. Chem. C* **2013**, *117*, 25269–25275. [CrossRef]
152. Pasti, I.A.; Gavrilov, N.M.; Mentus, S.V. Potentiodynamic investigation of oxygen reduction reaction on polycrystalline platinum surface in acidic solutions: The effect of the polarization rate on the kinetic parameters. *Int. J. Electrochem. Sci.* **2012**, *7*, 11076–11090.
153. Lopes, P.P.; Strmcnik, D.; Jirkovsky, J.S.; Connell, J.G.; Stamenkovic, V.; Markovic, N. Double layer effects in electrocatalysis: The oxygen reduction reaction and ethanol oxidation reaction on Au(111), Pt(111) and Ir(111) in alkaline media containing Na and Li cations. *Catal. Today* **2016**, *262*, 41–47. [CrossRef]

154. Wang, J.X.; Markovic, N.M.; Adzic, R.R. Kinetic analysis of oxygen reduction on Pt(111) in acid solutions: Intrinsic kinetic parameters and anion adsorption effects. *J. Phys. Chem. B* **2004**, *108*, 4127–4133. [CrossRef]
155. Markovic, N.; Gasteiger, H.; Ross, P.N. Kinetics of oxygen reduction on Pt(hkl) electrodes: Implications for the crystallite size effect with supported Pt electrocatalysts. *J. Electrochem. Soc.* **1997**, *144*, 1591–1597. [CrossRef]
156. Paulus, U.A.; Schmidt, T.J.; Gasteiger, H.A.; Behm, R.J. Oxygen reduction on a high-surface area Pt/vulcan carbon catalyst: A thin-film rotating ring-disk electrode study. *J. Electroanal. Chem.* **2001**, *495*, 134–145. [CrossRef]
157. Strmcnik, D.; Escudero-Escribano, M.; Kodama, K.; StamenkovicVojislav, R.; Cuesta, A.; Marković, N.M. Enhanced electrocatalysis of the oxygen reduction reaction based on patterning of platinum surfaces with cyanide. *Nat. Chem.* **2010**, *2*, 880–885. [CrossRef] [PubMed]
158. Antolini, E.; Gonzalez, E.R. Alkaline direct alcohol fuel cells. *J. Power Sources* **2010**, *195*, 3431–3450. [CrossRef]
159. Blizanac, B.B.; Ross, P.N.; Markovic, N.M. Oxygen electroreduction on Ag(111): The Ph effect. *Electrochim. Acta* **2007**, *52*, 2264–2271. [CrossRef]
160. Cifrain, M.; Kordesch, K.V. Advances, aging mechanism and lifetime in AFCs with circulating electrolytes. *J. Power Sources* **2004**, *127*, 234–242. [CrossRef]
161. Koscher, G.A.; Kordesch, K. Alkaline methanol–air system. *J. Sol. State Electrochem.* **2003**, *7*, 632–636. [CrossRef]
162. Lin, B.Y.S.; Kirk, D.W.; Thorpe, S.J. Performance of alkaline fuel cells: A possible future energy system? *J. Power Sources* **2006**, *161*, 474–483. [CrossRef]
163. Lewera, A.; Timperman, L.; Roguska, A.; Alonso-Vante, N. Metal–support interactions between nanosized Pt and metal oxides (WO_3 and TiO_2) studied using X-ray photoelectron spectroscopy. *J. Phys. Chem. C* **2011**, *115*, 20153–20159. [CrossRef]
164. Luo, Y.; Alonso-Vante, N. The effect of support on advanced Pt-based cathodes towards the oxygen reduction reaction. State of the art. *Electrochim. Acta* **2015**, *179*, 108–118. [CrossRef]
165. Yang, W.; Wang, X.; Yang, F.; Yang, C.; Yang, X. Carbon nanotubes decorated with Pt nanocubes by a noncovalent functionalization method and their role in oxygen reduction. *Adv. Mater.* **2008**, *20*, 2579–2587. [CrossRef]
166. Orfanidi, A.; Daletou, M.K.; Neophytides, S.G. Preparation and characterization of Pt on modified multi-wall carbon nanotubes to be used as electrocatalysts for high temperature fuel cell applications. *Appl. Catal. B: Environ.* **2011**, *106*, 379–389. [CrossRef]
167. Li, W.; Liang, C.; Zhou, W.; Qiu, J.; Zhou, Z.; Sun, G.; Xin, Q. Preparation and characterization of multiwalled carbon nanotube-supported platinum for cathode catalysts of direct methanol fuel cells. *J. Phys. Chem. B* **2003**, *107*, 6292–6299. [CrossRef]
168. Chen, Y.; Wang, J.; Liu, H.; Banis, M.N.; Li, R.; Sun, X.; Sham, T.-K.; Ye, S.; Knights, S. Nitrogen doping effects on carbon nanotubes and the origin of the enhanced electrocatalytic activity of supported Pt for proton-exchange membrane fuel cells. *J. Phys. Chem. C* **2011**, *115*, 3769–3776. [CrossRef]
169. Wang, S.; Jiang, S.P.; White, T.J.; Guo, J.; Wang, X. Electrocatalytic activity and interconnectivity of Pt nanoparticles on multiwalled carbon nanotubes for fuel cells. *J. Phys. Chem. C* **2009**, *113*, 18935–18945. [CrossRef]
170. Hijazi, I.; Bourgeteau, T.; Cornut, R.; Morozan, A.; Filoramo, A.; Leroy, J.; Derycke, V.; Jousselme, B.; Campidelli, S. Carbon nanotube-templated synthesis of covalent porphyrin network for oxygen reduction reaction. *J. Am. Chem. Soc.* **2014**, *136*, 6348–6354. [CrossRef] [PubMed]
171. Hasche, F.; Oezaslan, M.; Strasser, P. Activity, stability and degradation of multi walled carbon nanotube (MXCNT) supported Pt fuel cell electrocatalysts. *PCCP* **2010**, *12*, 15251–15258. [CrossRef] [PubMed]
172. Kongkanand, A.; Vinodgopal, K.; Kuwabata, S.; Kamat, P.V. Highly dispersed Pt catalysts on single-walled carbon nanotubes and their role in methanol oxidation. *J. Phys. Chem. B* **2006**, *110*, 16185–16188. [CrossRef] [PubMed]
173. Wang, J.J.; Yin, G.P.; Zhang, J.; Wang, Z.B.; Gao, Y.Z. High utilization platinum deposition on single-walled carbon nanotubes as catalysts for direct methanol fuel cell. *Electrochim. Acta* **2007**, *52*, 7042–7050. [CrossRef]
174. Su, L.; Jia, W.; Zhang, L.; Beacham, C.; Zhang, H.; Lei, Y. Facile synthesis of a platinum nanoflower monolayer on a single-walled carbon nanotube membrane and its application in glucose detection. *J. Phys. Chem. C* **2010**, *114*, 18121–18125. [CrossRef]

175. Seo, M.H.; Choi, S.M.; Seo, J.K.; Noh, S.H.; Kim, W.B.; Han, B. The graphene-supported palladium and palladium–yttrium nanoparticles for the oxygen reduction and ethanol oxidation reactions: Experimental measurement and computational validation. *Appl. Catal. B: Environ.* **2013**, *129*, 163–171. [CrossRef]
176. Rao, C.V.; Reddy, A.L.M.; Ishikawa, Y.; Ajayan, P.M. Synthesis and electrocatalytic oxygen reduction activity of graphene-supported Pt_3Co and Pt_3Cr alloy nanoparticles. *Carbon* **2011**, *49*, 931–936. [CrossRef]
177. Kou, R.; Shao, Y.; Wang, D.; Engelhard, M.H.; Kwak, J.H.; Wang, J.; Viswanathan, V.V.; Wang, C.; Lin, Y.; Wang, Y.; et al. Enhanced activity and stability of Pt catalysts on functionalized graphene sheets for electrocatalytic oxygen reduction. *Electrochem. Commun.* **2009**, *11*, 954–957. [CrossRef]
178. Li, Y.; Tang, L.; Li, J. Preparation and electrochemical performance for methanol oxidation of Pt/graphene nanocomposites. *Electrochem. Commun.* **2009**, *11*, 846–849. [CrossRef]
179. Moldovan, M.S.; Bulou, H.; Dappe, Y.J.; Janowska, I.; Bégin, D.; Pham-Huu, C.; Ersen, O. On the evolution of Pt nanoparticles on few-layer graphene supports in the high-temperature range. *J. Phys. Chem. C* **2012**, *116*, 9274–9282. [CrossRef]
180. Shao, Y.; Zhang, S.; Wang, C.; Nie, Z.; Liu, J.; Wang, Y.; Lin, Y. Highly durable graphene nanoplatelets supported Pt nanocatalysts for oxygen reduction. *J. Power Sources* **2010**, *195*, 4600–4605. [CrossRef]
181. Jahan, M.; Bao, Q.; Loh, K.P. Electrocatalytically active graphene–porphyrin MOF composite for oxygen reduction reaction. *J. Am. Chem. Soc.* **2012**, *134*, 6707–6713. [CrossRef] [PubMed]
182. Jin, T.; Guo, S.; Zuo, J.-L.; Sun, S. Synthesis and assembly of Pd nanoparticles on graphene for enhanced electrooxidation of formic acid. *Nanoscale* **2013**, *5*, 160–163. [CrossRef] [PubMed]
183. Di Noto, V.; Negro, E.; Lavina, S.; Gross, S.; Pace, G. Pd-Co carbon-nitride electrocatalysts for polymer electrolyte fuel cells. *Electrochim. Acta* **2007**, *53*, 1604–1617. [CrossRef]
184. Di Noto, V.; Negro, E.; Polizzi, S.; Riello, P.; Atanassov, P. Preparation, characterization and single-cell performance of a new class of Pd-carbon nitride electrocatalysts for oxygen reduction reaction in PEMFCs. *Appl. Catal. B: Environ.* **2012**, *111–112*, 185–199. [CrossRef]
185. Di Noto, V.; Negro, E.; Polizzi, S.; Vezzù, K.; Toniolo, L.; Cavinato, G. Synthesis, studies and fuel cell performance of "core–shell" electrocatalysts for oxygen reduction reaction based on a $PtNi_x$ carbon nitride "shell" and a pyrolyzed polyketone nanoball "core". *Int. J. Hydrogen Energy* **2014**, *39*, 2812–2827. [CrossRef]
186. Di Noto, V.; Negro, E.; Polizzi, S.; Agresti, F.; Giffin, G.A. Synthesis–structure–morphology interplay of bimetallic "core–shell" carbon nitride nano-electrocatalysts. *ChemSusChem* **2012**, *5*, 2451–2459. [CrossRef] [PubMed]
187. Datye, A.K.; Kalakkad, D.S.; Yao, M.H.; Smith, D.J. Comparison of metal-support interactions in Pt/TiO_2 and Pt/CeO_2. *J. Catal.* **1995**, *155*, 148–153. [CrossRef]
188. Koudelka, M.; Monnier, A.; Sanchez, J.; Augustynski, J. Correlation between the surface composition of Pt/TiO_2 catalysts and their adsorption behaviour in aqueous solutions. *J. Mol. Catal.* **1984**, *25*, 295–305. [CrossRef]
189. Jiang, D.-e.; Overbury, S.H.; Dai, S. Structures and energetics of Pt clusters on TiO_2: Interplay between metal–metal bonds and metal–oxygen bonds. *J. Phys. Chem. C* **2012**, *116*, 21880–21885. [CrossRef]
190. Bauer, A.; Lee, K.; Song, C.; Xie, Y.; Zhang, J.; Hui, R. Pt nanoparticles deposited on TiO_2 based nanofibers: Electrochemical stability and oxygen reduction activity. *J. Power Sources* **2010**, *195*, 3105–3110. [CrossRef]
191. Huang, S.-Y.; Ganesan, P.; Popov, B.N. Electrocatalytic activity and stability of niobium-doped titanium oxide supported platinum catalyst for polymer electrolyte membrane fuel cells. *Appl. Catal. B: Environ.* **2010**, *96*, 224–231. [CrossRef]
192. Huang, S.-Y.; Ganesan, P.; Popov, B.N. Titania supported platinum catalyst with high electrocatalytic activity and stability for polymer electrolyte membrane fuel cell. *Appl. Catal. B: Environ.* **2011**, *102*, 71–77. [CrossRef]
193. Ho, V.T.T.; Pan, C.-J.; Rick, J.; Su, W.-N.; Hwang, B.-J. Nanostructured $Ti_{0.7}Mo_{0.3}O_2$ support enhances electron transfer to Pt: High-performance catalyst for oxygen reduction reaction. *J. Am. Chem. Soc.* **2011**, *133*, 11716–11724. [CrossRef] [PubMed]
194. Estudillo-Wong, L.A.; Luo, Y.; Diaz-Real, J.A.; Alonso-Vante, N. Enhanced oxygen reduction reaction stability on platinum nanoparticles photo-deposited onto oxide-carbon composites. *Appl. Catal. B: Environ.* **2015**, *187*, 291–300. [CrossRef]
195. Luo, Y.; Calvillo, L.; Daiguebonne, C.; Daletou, M.K.; Granozzi, G.; Alonso-Vante, N. A highly efficient and stable oxygen reduction reaction on $Pt/CeO_x/C$ electrocatalyst obtained via a sacrificial precursor based on a metal-organic framework. *Appl. Catal. B: Environ.* **2016**, *189*, 39–50. [CrossRef]

196. Ruiz Camacho, B.; Morais, C.; Valenzuela, M.A.; Alonso-Vante, N. Enhancing oxygen reduction reaction activity and stability of platinum via oxide-carbon composites. *Catal. Today* **2013**, *202*, 36–43. [CrossRef]
197. Luo, Y.; Habrioux, A.; Calvillo, L.; Granozzi, G.; Alonso-Vante, N. Thermally induced strains on the catalytic activity and stability of Pt–M_2O_3/C (M = Y or Gd) catalysts towards oxygen reduction reaction. *ChemCatChem* **2015**, *7*, 1573–1582. [CrossRef]
198. Luo, Y.; Habrioux, A.; Calvillo, L.; Granozzi, G.; Alonso-Vante, N. Yttrium oxide/gadolinium oxide-modified platinum nanoparticles as cathodes for the oxygen reduction reaction. *ChemPhysChem* **2014**, *15*, 2136–2144. [CrossRef] [PubMed]
199. Tauster, S.J. Strong metal-support interactions. *Acc. Chem. Res.* **1987**, *20*, 389–394. [CrossRef]
200. Tauster, S.J.; Fung, S.C.; Garten, R.L. Strong metal-support interactions. Group 8 noble metals supported on titanium dioxide. *J. Am. Chem. Soc.* **1978**, *100*, 170–175. [CrossRef]
201. Ma, J.; Habrioux, A.; Morais, C.; Lewera, A.; Vogel, W.; Verde-Gómez, Y.; Ramos-Sanchez, G.; Balbuena, P.B.; Alonso-Vante, N. Spectroelectrochemical probing of the strong interaction between platinum nanoparticles and graphitic domains of carbon. *ACS Catal.* **2013**, *3*, 1940–1950. [CrossRef]
202. Ma, J.; Habrioux, A.; Pisarek, M.; Lewera, A.; Alonso-Vante, N. Induced electronic modification of Pt nanoparticles deposited onto graphitic domains of carbon materials by uv irradiation. *Electrochem. Commun.* **2013**, *29*, 12–16. [CrossRef]
203. Fleisch, T.H.; Hicks, R.F.; Bell, A.T. An XPS study of metal-support interactions on $PdSiO_2$ and $PdLa_2O_3$. *J. Catal.* **1984**, *87*, 398–413. [CrossRef]
204. Dall'Agnol, C.; Gervasini, A.; Morazzoni, F.; Pinna, F.; Strukul, G.; Zanderighi, L. Hydrogenation of carbon monoxide: Evidence of a strong metal-support interaction in $RhZrO_2$ catalysts. *J. Catal.* **1985**, *96*, 106–114. [CrossRef]
205. Wu, G.; Zelenay, P. Nanostructured nonprecious metal catalysts for oxygen reduction reaction. *Acc. Chem. Res.* **2013**, *46*, 1878–1889. [CrossRef] [PubMed]
206. Wu, G.; Mack, N.H.; Gao, W.; Ma, S.; Zhong, R.; Han, J.; Baldwin, J.K.; Zelenay, P. Nitrogen-doped graphene-rich catalysts derived from heteroatom polymers for oxygen reduction in nonaqueous lithium–O_2 battery cathodes. *ACS Nano* **2012**, *6*, 9764–9776. [CrossRef] [PubMed]
207. Wu, G.; More, K.L.; Johnston, C.M.; Zelenay, P. High-performance electrocatalysts for oxygen reduction derived from polyaniline, iron, and cobalt. *Science* **2011**, *332*, 443–447. [CrossRef] [PubMed]
208. Fu, T.; Wang, M.; Cai, W.; Cui, Y.; Gao, F.; Peng, L.; Chen, W.; Ding, W. Acid-resistant catalysis without use of noble metals: Carbon nitride with underlying nickel. *ACS Catal.* **2014**, *4*, 2536–2543. [CrossRef]
209. Jiang, T.; Zhang, Q.; Wang, T.-J.; Zhang, Q.; Ma, L.-L. High yield of pentane production by aqueous-phase reforming of xylitol over Ni/HZSM-5 and Ni/MCM22 catalysts. *Energy Convers. Manag.* **2012**, *59*, 58–65. [CrossRef]
210. Luo, Y.; Estudillo-Wong, L.A.; Alonso-Vante, N. Carbon supported Pt-Y_2O_3 and Pt-Gd_2O_3 nanoparticles prepared via carbonyl chemical route towards oxygen reduction reaction: Kinetics and stability. *Int. J. Hydrogen Energy* **2016**, in press. [CrossRef]
211. Vogel, W.; Timperman, L.; Alonso-Vante, N. Probing metal substrate interaction of Pt nanoparticles: Structural XRD analysis and oxygen reduction reaction. *Appl. Catal. A* **2010**, *377*, 167–173. [CrossRef]
212. Ma, J.; Habrioux, A.; Gago, A.; Alonso-Vante, N. Towards understanding the essential role played by the platinum-support interaction on electrocatalytic activity. *ECS Trans.* **2013**, *45*, 25–33. [CrossRef]
213. Ma, J.; Habrioux, A.; Guignard, N.; Alonso-Vante, N. Functionalizing effect of increasingly graphitic carbon supports on carbon-supported and TiO_2–carbon composite-supported Pt nanoparticles. *J. Phys. Chem. C* **2012**, *116*, 21788–21794. [CrossRef]
214. Matter, P.H.; Zhang, L.; Ozkan, U.S. The role of nanostructure in nitrogen-containing carbon catalysts for the oxygen reduction reaction. *J. Catal.* **2006**, *239*, 83–96. [CrossRef]
215. Wang, D.; Xin, H.L.; Hovden, R.; Wang, H.; Yu, Y.; Muller, D.A.; DiSalvo, F.J.; Abruña, H.D. Structurally ordered intermetallic platinum–cobalt core–shell nanoparticles with enhanced activity and stability as oxygen reduction electrocatalysts. *Nat. Mater.* **2013**, *12*, 81–87. [CrossRef] [PubMed]
216. Wang, D.; Xin, H.L.; Wang, H.; Yu, Y.; Rus, E.; Muller, D.A.; DiSalvo, F.J.; Abruña, H.D. Facile synthesis of carbon-supported Pd–Co core–shell nanoparticles as oxygen reduction electrocatalysts and their enhanced activity and stability with monolayer pt decoration. *Chem. Mater.* **2012**, *24*, 2274–2281. [CrossRef]

217. Wang, D.; Xin, H.L.; Yu, Y.; Wang, H.; Rus, E.; Muller, D.A.; Abruña, H.D. Pt-decorated PdCo@Pd/C core–shell nanoparticles with enhanced stability and electrocatalytic activity for the oxygen reduction reaction. *J. Am. Chem. Soc.* **2010**, *132*, 17664–17666. [CrossRef] [PubMed]
218. Lee, J.-S.; Park, G.S.; Lee, H.I.; Kim, S.T.; Cao, R.; Liu, M.; Cho, J. Ketjenblack carbon supported amorphous manganese oxides nanowires as highly efficient electrocatalyst for oxygen reduction reaction in alkaline solutions. *Nano Lett.* **2011**, *11*, 5362–5366. [CrossRef] [PubMed]
219. Cui, C.; Gan, L.; Heggen, M.; Rudi, S.; Strasser, P. Compositional segregation in shaped Pt alloy nanoparticles and their structural behaviour during electrocatalysis. *Nat. Mater.* **2013**, *12*, 765–771. [CrossRef] [PubMed]
220. Chhina, H.; Campbell, S.; Kesler, O. An oxidation-resistant indium tin oxide catalyst support for proton exchange membrane fuel cells. *J. Power Sources* **2006**, *161*, 893–900. [CrossRef]
221. Millington, B.; Whipple, V.; Pollet, B.G. A novel method for preparing proton exchange membrane fuel cell electrodes by the ultrasonic-spray technique. *J. Power Sources* **2011**, *196*, 8500–8508. [CrossRef]
222. Malacrida, P.; Escudero-Escribano, M.; Verdaguer-Casadevall, A.; Stephens, I.E.L.; Chorkendorff, I. Enhanced activity and stability of Pt-La and Pt-Ce alloys for oxygen electroreduction: The elucidation of the active surface phase. *J. Mater. Chem. A* **2014**, *2*, 4234–4243. [CrossRef]
223. Escudero-Escribano, M.; Verdaguer-Casadevall, A.; Malacrida, P.; Grønbjerg, U.; Knudsen, B.P.; Jepsen, A.K.; Rossmeisl, J.; Stephens, I.E.L.; Chorkendorff, I. Pt_5Gd as a highly active and stable catalyst for oxygen electroreduction. *J. Am. Chem. Soc.* **2012**, *134*, 16476–16479. [CrossRef] [PubMed]
224. Hernandez-Fernandez, P.; Masini, F.; McCarthy, D.N.; Strebel, C.E.; Friebel, D.; Deiana, D.; Malacrida, P.; Nierhoff, A.; Bodin, A.; Wise, A.M.; et al. Mass-selected nanoparticles of Pt_xY as model catalysts for oxygen electroreduction. *Nat. Chem.* **2014**, *6*, 732–738. [CrossRef] [PubMed]
225. Jeon, M.K.; McGinn, P.J. Carbon supported Pt–Y electrocatalysts for the oxygen reduction reaction. *J. Power Sources* **2011**, *196*, 1127–1131. [CrossRef]
226. Nishanth, K.G.; Sridhar, P.; Pitchumani, S. Enhanced oxygen reduction reaction activity through spillover effect by Pt–$Y(OH)_3$/C catalyst in direct methanol fuel cells. *Electrochem. Commun.* **2011**, *13*, 1465–1468. [CrossRef]
227. Xu, J.; Gao, P.; Zhao, T.S. Non-precious Co_3O_4 nano-rod electrocatalyst for oxygen reduction reaction in anion-exchange membrane fuel cells. *Energy Environ. Sci.* **2012**, *5*, 5333–5339. [CrossRef]
228. Unni, S.M.; Mora-Hernandez, J.M.; Kurungot, S.; Alonso-Vante, N. $CoSe_2$ supported on nitrogen-doped carbon nanohorns as a methanol-tolerant cathode for air-breathing microlaminar flow fuel cells. *ChemElectroChem* **2015**, *2*, 1339–1345. [CrossRef]
229. Zhu, S.; Xu, G. Single-walled carbon nanohorns and their applications. *Nanoscale* **2010**, *2*, 2538–2549. [CrossRef] [PubMed]
230. Kasuya, D.; Yudasaka, M.; Takahashi, K.; Kokai, F.; Iijima, S. Selective production of single-wall carbon nanohorn aggregates and their formation mechanism. *J. Phys. Chem. B* **2002**, *106*, 4947–4951. [CrossRef]
231. Guo, D.-J.; Jing, Z.-H. A novel co-precipitation method for preparation of Pt-CeO_2 composites on multi-walled carbon nanotubes for direct methanol fuel cells. *J. Power Sources* **2010**, *195*, 3802–3805. [CrossRef]
232. Wang, X.; Li, W.; Chen, Z.; Waje, M.; Yan, Y. Durability investigation of carbon nanotube as catalyst support for proton exchange membrane fuel cell. *J. Power Sources* **2006**, *158*, 154–159. [CrossRef]
233. Wu, G.; More, K.L.; Xu, P.; Wang, H.-L.; Ferrandon, M.; Kropf, A.J.; Myers, D.J.; Ma, S.; Johnston, C.M.; Zelenay, P. A carbon-nanotube-supported graphene-rich non-precious metal oxygen reduction catalyst with enhanced performance durability. *Chem. Commun.* **2013**, *49*, 3291–3293. [CrossRef] [PubMed]
234. Jaouen, F.; Proietti, E.; Lefevre, M.; Chenitz, R.; Dodelet, J.-P.; Wu, G.; Chung, H.T.; Johnston, C.M.; Zelenay, P. Recent advances in non-precious metal catalysis for oxygen-reduction reaction in polymer electrolyte fuel cells. *Energy Environ. Sci.* **2011**, *4*, 114–130. [CrossRef]
235. Li, Q.; Xu, P.; Gao, W.; Ma, S.; Zhang, G.; Cao, R.; Cho, J.; Wang, H.-L.; Wu, G. Graphene/graphene-tube nanocomposites templated from cage-containing metal-organic frameworks for oxygen reduction in Li–O_2 batteries. *Adv. Mater.* **2014**, *26*, 1378–1386. [CrossRef] [PubMed]
236. Estudillo-Wong, L.A.; Vargas-Gómez, A.M.; Arce-Estrada, E.M.; Manzo-Robledo, A. TiO_2/C composite as a support for Pd-nanoparticles toward the electrocatalytic oxidation of methanol in alkaline media. *Electrochim. Acta* **2013**, *112*, 164–170. [CrossRef]
237. Xiong, L.; Manthiram, A. Synthesis and characterization of methanol tolerant Pt/TiO_x/C nanocomposites for oxygen reduction in direct methanol fuel cells. *Electrochim. Acta* **2004**, *49*, 4163–4170. [CrossRef]

238. Andrew Lin, K.-Y.; Hsu, F.-K.; Lee, W.-D. Magnetic cobalt-graphene nanocomposite derived from self-assembly of MOFs with graphene oxide as an activator for peroxymonosulfate. *J. Mater. Chem. A* **2015**, *3*, 9480–9490. [CrossRef]
239. Guo, D.-J.; Cui, S.-K.; Sun, H. Preparation of Pt–CeO_2/MWNT nano-composites by reverse micellar method for methanol oxidation. *J. Nanoparticle Res.* **2009**, *11*, 707–712. [CrossRef]
240. Von Kraemer, S.; Wikander, K.; Lindbergh, G.; Lundblad, A.; Palmqvist, A.E.C. Evaluation of TiO_2 as catalyst support in Pt-TiO_2/C composite cathodes for the proton exchange membrane fuel cell. *J. Power Sources* **2008**, *180*, 185–190. [CrossRef]
241. Sun, Z.; Wang, X.; Liu, Z.; Zhang, H.; Yu, P.; Mao, L. Pt–Ru/CeO_2/carbon nanotube nanocomposites: An efficient electrocatalyst for direct methanol fuel cells. *Langmuir* **2010**, *26*, 12383–12389. [CrossRef] [PubMed]
242. Ma, J.; Habrioux, A.; Luo, Y.; Ramos-Sanchez, G.; Calvillo, L.; Granozzi, G.; Balbuena, P.B.; Alonso-Vante, N. Electronic interaction between platinum nanoparticles and nitrogen-doped reduced graphene oxide: Effect on the oxygen reduction reaction. *J. Mater. Chem. A* **2015**, *3*, 11891–11904. [CrossRef]
243. Sreekuttan, M.U.; Campos-Roldan, C.A.; Mora-Hernandez, J.M.; Luo, Y.; Estudillo-Wong, L.A.; Alonso-Vante, N. The effect of carbon-based substrates onto non-precious and precious electrocatalytic centers. *ECS Trans.* **2015**, *69*, 35–42. [CrossRef]
244. Lee, C.-L.; Huang, C.-H.; Huang, K.-L.; Tsai, Y.-L.; Yang, C.-C. A comparison of three carbon nanoforms as catalyst supports for the oxygen reduction reaction. *Carbon* **2013**, *60*, 392–400. [CrossRef]
245. Liu, Z.-T.; Huang, K.-L.; Wu, Y.-S.; Lyu, Y.-P.; Lee, C.-L. A comparison of physically and chemically defective graphene nanosheets as catalyst supports for cubic Pd nanoparticles in an alkaline oxygen reduction reaction. *Electrochim. Acta* **2015**, *186*, 552–561. [CrossRef]
246. Thanh Ho, V.T.; Pillai, K.C.; Chou, H.-L.; Pan, C.-J.; Rick, J.; Su, W.-N.; Hwang, B.-J.; Lee, J.-F.; Sheu, H.-S.; Chuang, W.-T. Robust non-carbon $Ti_{0.7}Ru_{0.3}O_2$ support with co-catalytic functionality for Pt: Enhances catalytic activity and durability for fuel cells. *Energy Environ. Sci.* **2011**, *4*, 4194–4200. [CrossRef]
247. Timperman, L.; Alonso-Vante, N. Oxide substrate effect toward electrocatalytic enhancement of platinum and ruthenium–selenium catalysts. *Electrocatalysis* **2011**, *2*, 181–191. [CrossRef]
248. Scotti, G.; Kanninen, P.; Matilainen, V.-P.; Salminen, A.; Kallio, T. Stainless steel micro fuel cells with enclosed channels by laser additive manufacturing. *Energy* **2016**, *106*, 475–481. [CrossRef]
249. Wang, R.; Xu, Z. Recycling of non-metallic fractions from waste electrical and electronic equipment (WEEE): A review. *Waste Manag.* **2014**, *34*, 1455–1469. [CrossRef] [PubMed]
250. Cadena, L.E.S.; Arroyo, Z.G.; Lara, M.A.G.; Quiroz, Q.D. Cell-phone recycling by solvolysis for recovery of metals. *J. Mater. Sci. Chem. Eng.* **2015**, *3*, 52–57. [CrossRef]
251. Xiao, Z.; Feng, C.; Chan, P.C.H.; Hsing, I.M. Monolithically integrated planar microfuel cell arrays. *Sensors Actuators B: Chem.* **2008**, *132*, 576–586. [CrossRef]
252. Cha, S.-W.; O'Hayre, R.; Lee, S.J.; Saito, Y.; Prinz, F.B. Geometric scale effect of flow channels on performance of fuel cells. *J. Electrochem. Soc.* **2004**, *151*, A1856–A1864. [CrossRef]
253. Lu, Y.; Reddy, R.G. Performance of micro-PEM fuel cells with different flow fields. *J. Power Sources* **2010**, *195*, 503–508. [CrossRef]
254. Hockaday, R.; Navas, C. Micro-fuel cells ^{TM} for portable electronics. *Fuel Cells Bull.* **1999**, *2*, 9–12. [CrossRef]
255. Mex, L.; Ponath, N.; Müller, J. Miniaturized fuel cells based on microsystem technologies. *Fuel Cells Bull.* **2001**, *4*, 9–12. [CrossRef]
256. Breakthrough in micro fuel cell design, architecture. *Fuel Cells Bull.* **2002**, 1. Available online: http://thirdworld.nl/breakthrough-in-micro-fuel-cell-design-architecture (accessed on 15 September 2016).
257. Micro fuel cell developed at llnl. *Fuel Cells Bull.* **2002**, 4. Available online: http://thirdworld.nl/breakthrough-in-micro-fuel-cell-design-architecture (accessed on 15 September 2016).
258. Lee, S.J.; Chang-Chien, A.; Cha, S.W.; O'Hayre, R.; Park, Y.I.; Saito, Y.; Prinz, F.B. Design and fabrication of a micro fuel cell array with "flip-flop" interconnection. *J. Power Sources* **2002**, *112*, 410–418. [CrossRef]
259. Blum, A.; Duvdevani, T.; Philosoph, M.; Rudoy, N.; Peled, E. Water-neutral micro direct-methanol fuel cell (DMFC) for portable applications. *J. Power Sources* **2003**, *117*, 22–25. [CrossRef]
260. Yu, J.; Cheng, P.; Ma, Z.; Yi, B. Fabrication of miniature silicon wafer fuel cells with improved performance. *J. Power Sources* **2003**, *124*, 40–46. [CrossRef]

261. Choban, E.R.; Markoski, L.J.; Wieckowski, A.; Kenis, P.J.A. Microfluidic fuel cell based on laminar flow. *J. Power Sources* **2004**, *128*, 54–60. [CrossRef]
262. Choban, E.R.; Spendelow, J.S.; Gancs, L.; Wieckowski, A.; Kenis, P.J.A. Membraneless laminar flow-based micro fuel cells operating in alkaline, acidic, and acidic/alkaline media. *Electrochim. Acta* **2005**, *50*, 5390–5398. [CrossRef]
263. McLean, G.F.; Niet, T.; Prince-Richard, S.; Djilali, N. An assessment of alkaline fuel cell technology. *Int. J. Hydrogen Energy* **2002**, *27*, 507–526. [CrossRef]
264. Tripković, A.V.; Popović, K.D.; Lović, J.D.; Jovanović, V.M.; Kowal, A. Methanol oxidation at platinum electrodes in alkaline solution: Comparison between supported catalysts and model systems. *J. Electroanal. Chem.* **2004**, *572*, 119–128. [CrossRef]
265. Yu, E.H.; Scott, K. Development of direct methanol alkaline fuel cells using anion exchange membranes. *J. Power Sources* **2004**, *137*, 248–256. [CrossRef]
266. Hsieh, S.-S.; Yang, S.-H.; Kuo, J.-K.; Huang, C.-F.; Tsai, H.-H. Study of operational parameters on the performance of micro PEMFCs with different flow fields. *Energy Convers. Manag.* **2006**, *47*, 1868–1878. [CrossRef]
267. Nakajima, H.; Konomi, T.; Kitahara, T. Direct water balance analysis on a polymer electrolyte fuel cell (PEFC): Effects of hydrophobic treatment and micro-porous layer addition to the gas diffusion layer of a PEFC on its performance during a simulated start-up operation. *J. Power Sources* **2007**, *171*, 457–463. [CrossRef]
268. Hsieh, S.-S.; Huang, Y.-J. Measurements of current and water distribution for a micro-pem fuel cell with different flow fields. *J. Power Sources* **2008**, *183*, 193–204. [CrossRef]
269. Park, B.Y.; Madou, M.J. Design, fabrication, and initial testing of a miniature pem fuel cell with micro-scale pyrolyzed carbon fluidic plates. *J. Power Sources* **2006**, *162*, 369–379. [CrossRef]
270. Lin, P.-C.; Park, B.Y.; Madou, M.J. Development and characterization of a miniature PEM fuel cell stack with carbon bipolar plates. *J. Power Sources* **2008**, *176*, 207–214. [CrossRef]
271. Whipple, D.T.; Jayashree, R.S.; Egas, D.; Alonso-Vante, N.; Kenis, P.J.A. Ruthenium cluster-like chalcogenide as a methanol tolerant cathode catalyst in air-breathing laminar flow fuel cells. *Electrochim. Acta* **2009**, *54*, 4384–4388. [CrossRef]
272. Cheng, H.; Yuan, W.; Scott, K. Influence of thermal treatment on RuSe cathode materials for direct methanol fuel cells. *Fuel Cells* **2007**, *7*, 16–20. [CrossRef]
273. Colmenares, L.; Jusys, Z.; Behm, R.J. Activity, selectivity, and methanol tolerance of Se-modified Ru/C cathode catalysts. *J. Phys. Chem. C* **2007**, *111*, 1273–1283. [CrossRef]
274. Cremers, C.; Scholz, M.; Seliger, W.; Racz, A.; Knechtel, W.; Rittmayr, J.; Grafwallner, F.; Peller, H.; Stimming, U. Developments for improved direct methanol fuel cell stacks for portable power. *Fuel Cells* **2007**, *7*, 21–31. [CrossRef]
275. Itoe, R.N.; Wesson, G.D.; Kalu, E.E. Evaluation of oxygen transport parameters in H_2SO_4-CH_3OH mixtures using electrochemical methods. *J. Electrochem. Soc.* **2000**, *147*, 2445–2450. [CrossRef]
276. Gago, A.S.; Morales-Acosta, D.; Arriaga, L.G.; Alonso-Vante, N. Carbon supported ruthenium chalcogenide as cathode catalyst in a microfluidic formic acid fuel cell. *J. Power Sources* **2011**, *196*, 1324–1328. [CrossRef]
277. Brushett, F.R.; Naughton, M.S.; Ng, J.W.D.; Yin, L.; Kenis, P.J.A. Analysis of Pt/C electrode performance in a flowing-electrolyte alkaline fuel cell. *Int. J. Hydrogen Energy* **2012**, *37*, 2559–2570. [CrossRef]
278. Gago, A.S.; Gochi-Ponce, Y.; Feng, Y.-J.; Esquivel, J.P.; Sabaté, N.; Santander, J.; Alonso-Vante, N. Tolerant chalcogenide cathodes of membraneless micro fuel cells. *ChemSusChem* **2012**, *5*, 1488–1494. [CrossRef] [PubMed]
279. Gago, A.S.; Esquivel, J.-P.; Sabaté, N.; Santander, J.; Alonso-Vante, N. Comprehensive characterization and understanding of micro-fuel cells operating at high methanol concentrations. *Beilstein J. Nanotechnol.* **2015**, *6*, 2000–2006. [CrossRef] [PubMed]
280. Ma, J.; Habrioux, A.; Morais, C.; Alonso-Vante, N. Electronic modification of Pt via Ti and Se as tolerant cathodes in air-breathing methanol microfluidic fuel cells. *PhysChemChemPhys* **2014**, *16*, 13820–13826. [CrossRef] [PubMed]